UNIVERSITY OF CALIFORNIA
SANTA CRUZ

BAYESIAN STATISTICAL INFERENCE OF GIANT PLANET PHYSICS

A dissertation submitted in partial satisfaction of the
requirements for the degree of

DOCTOR OF PHILOSOPHY

in

PHYSICS

by

Daniel P. Thorngren

June 2019

The Dissertation of Daniel P. Thorngren
is approved:

Jonathan Fortney, Chair

Stefano Profumo

Ruth Murray-Clay

Francis Nimmo

Lori Kletzer
Dean of Graduate Studies

Table of Contents

List of Figures

List of Tables

Abstract

Bayesian Statistical Inference of Giant Planet Physics

by

Daniel P. Thorngren

The many exoplanet discoveries of recent years have opened new avenues for studying giant planets and their formation. The giant planets of our solar system have been studied up close and in great detail, and exoplanets can complement this with a rich population to examine statistically. More than just studying their occurrence rates, it is possible to combine physical and statistical models to uncover aspects of their physical processes. I apply this strategy here on a series of related topics. First, I study a set of cool giant exoplanets, infer their bulk compositions, and demonstrate that there is a relationship between a planet's mass and its composition. I further discuss the implications to their formation, and how a planet's bulk composition can usefully complement its observed atmospheric abundances. I also consider hot Jupiters, inferring the amount of internal heating required to explain their anomalously large radii, the cause of which is one of the longest standing open questions in exoplanet science. I show through a careful examination of their radii and parent star evolution that these objects appear to reinflate quickly when their equilibrium temperature is increased. This strongly constrains the physical mechanisms that are causing their inflation. Finally, I outline several immediately relevant areas for future work to better understand these objects.

Acknowledgments

First, I wish to thank my parents, Jane and Peter, and my sister Christina for their love and support as I pursued this path. I am also greatly indebted to my advisor, Jonathan Fortney, for his guidance and support when I had difficulties. Finally, I sincerely thank my fellow researchers – Eric Lopez, Michael Line, Chris Mankovich, Naor Movshovitz, Peter Gao, Laura Mayorga, Thaddeus Komacek, and too many others to list – for many helpful discussions and especially for their warm welcome into this field.

1. Introduction

In studying the physics of planets and their formation processes, giant planets are an especially valuable piece of the puzzle. Not only do they represent one class of planet formation outcomes, but their envelopes are records of the disk that created them. Until recently, we have had only the solar system giants to study. From these we have obtained a wealth of detailed information (see Sec. 1.1). However, our solar system is only one of many possible outcomes of planet formation, and is an inherently biased sample – we could only have observed a solar system that contains a habitable planet!

As such, the relatively recent discovery of extrasolar planets has been a tremendous boon to our understanding of planets and their formation. We have discovered new classes of planets, such as super Earths and hot Jupiters, which are not found in our solar system. We have also found planets in solar systems very unlike our own, such as around pulsars (Wolszczan & Frail, 1992), binary star systems (Doyle et al., 2011), A stars (Gaudi et al., 2017), and M dwarfs (Charbonneau et al., 2009). These planets are also a biased sample from observational constraints, but nevertheless allow for a much broader picture of planetary physics. Thus there is a synergy between the detailed observations available with solar system planets and the broad, diverse samples provided by exoplanets.

Naturally, research based on explanets initially focused on detailed simulations of individual planets (e.g. Baraffe et al., 2003; Fortney et al., 2006; Guillot & Havel,

2009; Nettelmann et al., 2010; Rogers & Seager, 2010, and many others), as had been done with the solar system giants. This approach is also a natural format for spectroscopic analysis of exoplanets, such as Deming et al. (2007); Swain et al. (2010); Benneke & Seager (2012); Kreidberg et al. (2014b); Piskorz et al. (2018). With the dramatic rise in detected exoplanets from the Kepler mission and others, it became possible to study the occurrence rate of planets as a function of semi-major axis, radius, mass, etc. (e.g. Johnson et al., 2010; Howard et al., 2010; Weiss et al., 2013; Fressin et al., 2013; Dressing & Charbonneau, 2013; Fulton et al., 2017).

Now that we have a relatively large sample of well-characterized exoplanets, it is possible to take a new approach. By constructing physical models of planets tied together by Bayesian statistical models of the whole population, we can test which physical models (and their parameters) are able to reproduce the properties of the observed population. In this work, I will discuss four research projects that apply this strategy, and show how their results provide a unique new contribution to the study of giant planets.

1.1 Solar System Giants

The solar system contains four giant planets, commonly classified into gas giants (Jupiter and Saturn) and ice giants (Uranus and Neptune). The gas giants, being easily visible to the naked eye, have been known of since prehistoric times. The ice giants are much harder to observe, and so they were not discovered until much later – Uranus in 1781 (Herschel, 1781), and Neptune in 1846 (Galle, 1846). These planets owe their label to the significant quantities of ice they contain, a term referring to volatile species such as water, ammonia, and methane.

Our understanding of the interiors of giant planets initially developed slowly,

owing to the difficulty of making relevant observations. A significant development was the proposal that hydrogen takes a liquid metallic state at extreme pressures (Wigner & Huntington, 1935). Early models of their interior composition were made (e.g. Demarcus, 1958), but our modern understanding arguably began when Hubbard (1968) argued that the excess emission of heat from Jupiter (from Low, 1966) can be explained by a convective envelope delivering energy from the interior to the surface.

A series of spacecraft visits to the giant planets has greatly increased our knowledge of their properties. Pioneers 10 and 11 visited Jupiter and Saturn during the 1970s and measured their gravitational fields, magnetic fields, atmospheric properties and more. Voyager 1 followed shortly thereafter, and Voyager 2 completed a tour of all of the giant planets between 1979 and 1989. Over the following decades the spacecraft Galileo, Ulysses, Cassini-Huygens, and New Horizons have all paid visits to the giants of the outer solar system. The Juno mission to Jupiter is ongoing.

Especially interesting to this work are measurements of atmospheric composition, because the atmosphere should have a similar composition to the interior due to convection. This data originally came from a myriad of spectroscopic observations from ground and space-based telescopes, but now include observations from spacecraft such as the Galileo's Solid State Imager (Belton et al., 1996), Cassini's Imaging Science Subsystem (Porco et al., 2005), Juno's Microwave Radiometer (Li et al., 2017), and too many others to list here. For Jupiter, we have a uniquely good source of information from the Galileo entry probe, which carried a mass spectrometer and other equipment into Jupiter in late 1995. It was able to gather invaluable measurements of the atmospheric composition (Niemann et al., 1998; Wong et al., 2004). Unfortunately, the water abundance it measured reflected

only the dry region that it landed in (see Baker & Schubert, 1998; Showman & Ingersoll, 1998). Arguably the most important result from these many observations was that relative to solar metal abundances (Lodders, 2009; Asplund et al., 2009), Jupiter is enhanced by a factor of $\sim 3.5\times$ (Atreya et al., 2018), Saturn by $\sim 5\times$ (Atreya et al., 2018), and Uranus and Neptune by $50 - 100\times$ (Guillot & Gautier, 2014).

1.1.1 Gravitational Fields

A particularly valuable dataset for interior modelling has been the measurements of the gravitational field by orbiting spacecraft. These come in the form of the spherical expansion coefficients (colloquially known as the J's) of the gravity field (see e.g. Guillot et al., 2004).

$$U(r,\theta) = \frac{GM}{r}\left(1 - \sum_{i=1}^{\infty}\left(\frac{R_{\rm eq}}{r}\right)^2 J_i P_i(\cos(\theta))\right) \tag{1.1}$$

Here $R_{\rm eq}$ is the equatorial radius of the planet, J_i is the $i^{\rm th}$ spherical expansion coefficient, and P_i is the $i^{\rm th}$ Legendre polynomial. These coefficients are nonzero due to the rotation of the planets, which pulls them into oblate spheroids. Due to north-south symmetry across the equator, J_i is extremely close to zero for odd values of i. These coefficients may be predicted from the density structure $\rho(\vec{r})$ of planetary interior models:

$$J_i = -\frac{1}{MR_{\rm eq}^i}\int_V \rho(\vec{r}) r^i P_i(\cos(\theta)) d\vec{r} \tag{1.2}$$

Note however, that this requires a model of the full 3-dimensional density structure of the planet. Computing this self-consistently is non-trivial, but can be accomplished through the theory of figures (Zharkov & Trubitsyn, 1974) or the

concentric Maclaurin spheroids (Hubbard, 2012) algorithms.

Comparison of interior models with observed coefficients has been a valuable approach for understanding solar system planets. These were refined, through Pioneer (Null, 1976), Voyager (Campbell & Synnott, 1985), Cassini (Anderson et al., 2010), and now Juno (Bolton et al., 2017; Iess et al., 2018) (these citations are not exhaustive). In each case, these have resulted in refinements of our understanding of their interiors through comparisons with structure modelling, e.g. Hubbard & Marley (1989); Chabrier et al. (1992); Guillot (1999). It is clear from these that Saturn has a heavy-element enriched core (Guillot, 1999; Helled, 2018). Jupiter appears to have a core as well, but there is ongoing debate about whether the core boundary is relatively well-defined (e.g. Guillot, 1999; Helled, 2018; Hubbard & Militzer, 2016), or ends in an extended composition gradient (e.g. Debras & Chabrier, 2019; Wahl et al., 2017) (see Sec. 1.4.4).

1.2 Exoplanet Discovery

The first confirmed discovery of an exoplanet occurred in 1992 through the careful analysis of the pulsation timings of the neutron star PSR1257 + 12 (Wolszczan & Frail, 1992). Though impressive, this feat was overshadowed several years later with the discovery of planets around "sunlike" stars – main sequence stars not differing wildly from the sun in mass and evolutionary state. This began with the discovery of 51 Peg b by Mayor & Queloz (1995) using the radial velocity method.

Briefly, this approach works by tracking the Doppler shifts of the spectroscopic lines in a star's spectrum. Neglecting small general relativistic corrections, lines shift a wavelength factor of $1 + V_r/c$ for a given radial velocity V_r of the star. This is important because an orbiting planet causes periodic oscillations in the star's radial velocity. The period is the planet's orbital period P, and the semi-amplitude

of oscillation K (in m/s) is:

$$K = \frac{m \sin(i)}{P^{1/3}(M+m)^{2/3}\sqrt{1-e^2}} \tag{1.3}$$

Here, m is the planet mass, M is the stellar mass, i is the inclination relative to the observer, and e is the orbital ecccentricity. Thus, from observables, the radial velocity method can measure the mass of a planet up to a factor of $\sin(i)$. A more thorough discussion can be found in Lovis & Fischer (2010).

A number of planet discoveries through the radial velocity method were subsequently made, and in 2000 it was discovered that one of these planets, HD 209458, transits its star (Charbonneau et al., 2000; Henry et al., 2000). In 2003, OGLE-TR-56 b became the first planet discovered through the transit method (Konacki et al., 2003), using data collected in a microlensing search. Transiting planets are of particular interest because their radius can be determined from their transit depths (the fractional darkening during transit) as $R_p = R_*\sqrt{d}$, where d is the transit depth and R_* is the parent star's radius (see Deeg & Alonso, 2018, for a more detailed discussion). The time between transits is the orbital period of the planet. Additionally, the inclination must be very close to $i = \pi/2$ in order for the planet to transit, and so radial velocity follow-up can measure the actual mass of the planet. A number of survey telescopes began searching for transits in the late 2000s including CoRoT (Auvergne et al., 2009), WASP (Pollacco et al., 2006), and Kepler (Borucki et al., 2010), which brought the number of known exoplanets into the thousands.

In this work, we are primarily interested in transiting planet with radial velocity follow-up, as these provide us with masses and radii. However, these are by no means the only ways to discover exoplanets, so I'll briefly mention a few other major techniques. First, a careful analysis of the exact timing of transits can re-

veal the presence of gravitational influences from other, potentially non-transiting planets; this is known as the transit timing variations (TTV) technique. It has been used to infer/confirm the presence of planets (e.g. Becker et al., 2015) and to help characterize existing systems (e.g. Jontof-Hutter et al., 2016; Hadden & Lithwick, 2017). Additionally, the direct imaging of exoplanets has been able to identify a number of young giant planets and brown dwarfs, such as Beta Pictoris b (Lagrange et al., 2009). Finally, microlensing surveys (see Batista, 2018) can sometimes identify planets in hard-to-observe parts of parameter space (e.g. Beaulieu et al., 2006). These planets are nearly always impossible to follow-up, but can be useful in determining the overall abundance of planets.

1.3 The Giant Exoplanet Population

Thanks to the efforts of various exoplanet surveys, more than a thousand giant planets have been discovered and confirmed. These are primarily from radial velocity and transit surveys, with smaller contributions from microlensing and direct imaging. Figure 1.1 depicts these planets' masses (often from approximations) against their semi-major axis, colored by their discovery techniques; the data was collected from exoplanet.eu (Schneider et al., 2011) and the NASA Exoplanet Archive (Akeson et al., 2013).

It is clear that different techniques sample parts of this space unevenly (see Cumming, 2010). Transit searches are better at finding planets close in because these are more likely to transit. Lacking this constraint, radial velocity approaches have been able to discover many more planets at larger separations. The RV and transit approaches are better able to identify massive and large planets respectively, but have nevertheless both managed to make discoveries of objects with Earth-like masses and radii. Direct imaging is constrained by the luminosity of

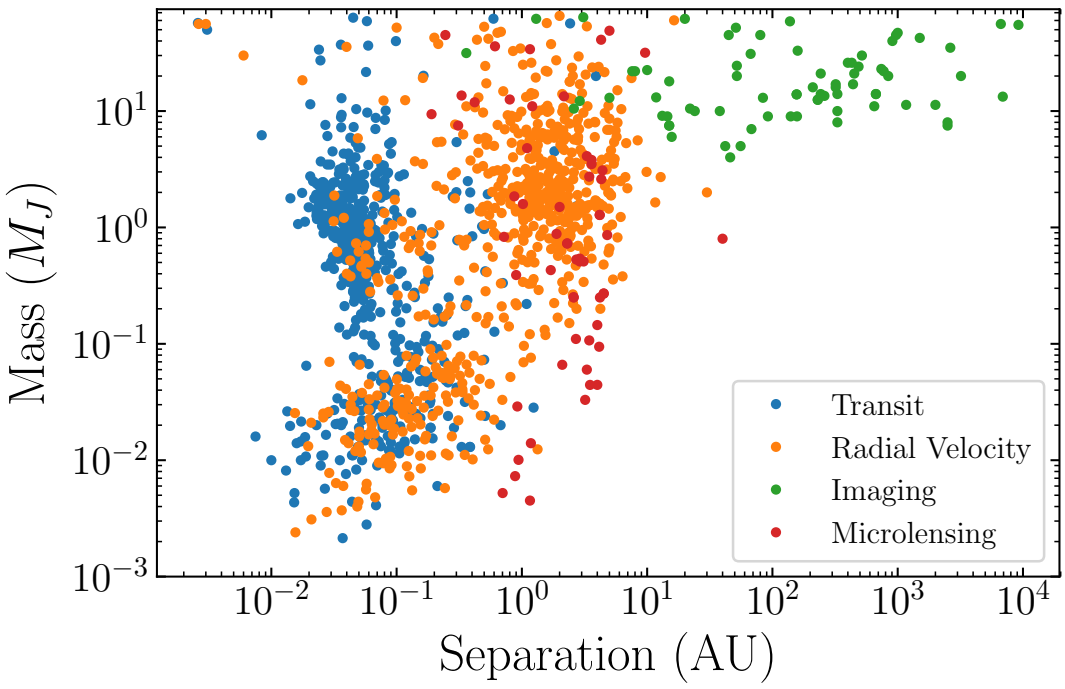

Figure 1.1: Mass vs. separation of discovered planets, colored by discovery method. For RV planets, the mass shown is only up to a factor of $\sin(i)$, where i is the inclination. For the remaining planets, some masses are estimated from theoretical models. Due to observational biases, the location and number of planets shown are not representative of the actual occurrence rates.

the planet and its angular separation from its parent star. For this reason, these discoveries have been primarily of young, very massive planets and brown dwarfs at large separations (hundreds to thousands of AU). HR 8799 is a classic example of this type of system (see Marois et al., 2008).

To characterize the interior of a giant planet, it is very important to have measurements of both its mass and radius. For transiting planets, RV follow-up or TTV analysis can be generally be used to determine the mass. However, planets discovered by RV are usually not transiting, and so the radius information is unavailable. Thus we nearly always consider only transiting planets for studying planetary interiors. Figure 1.2 shows the radius vs period for known transiting planets, colored by the survey that discovered them. A cluster of warm and hot giant planets is clearly present around the 1 R_J region primarily between 1 and 10 days. Below this, thanks primarily to the Kepler and K2 programs, there are a large number of sub-Neptunes and super Earths. It is important to remember that the distributions in these plots are the result not only of the underlying astrophysical distributions, but also of observational biases and publishing biases (favoring planets considered "interesting" by researchers).

For the purposes of this work, we will focus primarily on transiting planets with masses measured to be greater than 20 $M_\oplus$. Fig. 1.3 shows the radii of these planets plotted against their masses and colored by the incident flux. Jupiter, Saturn, Uranus, and Neptune are also shown for reference. A number of patterns related to their interior structure are immediately evident. First, planets below about Saturn's mass are clearly smaller than those above it. This is because the radius rises with mass until about Saturn's mass, whereupon electron degeneracy pressure dominates the equation of state. Where degeneracy pressure dominates, the mass-radius relation flattens. Also visible is the fact that Jupiter mass planets

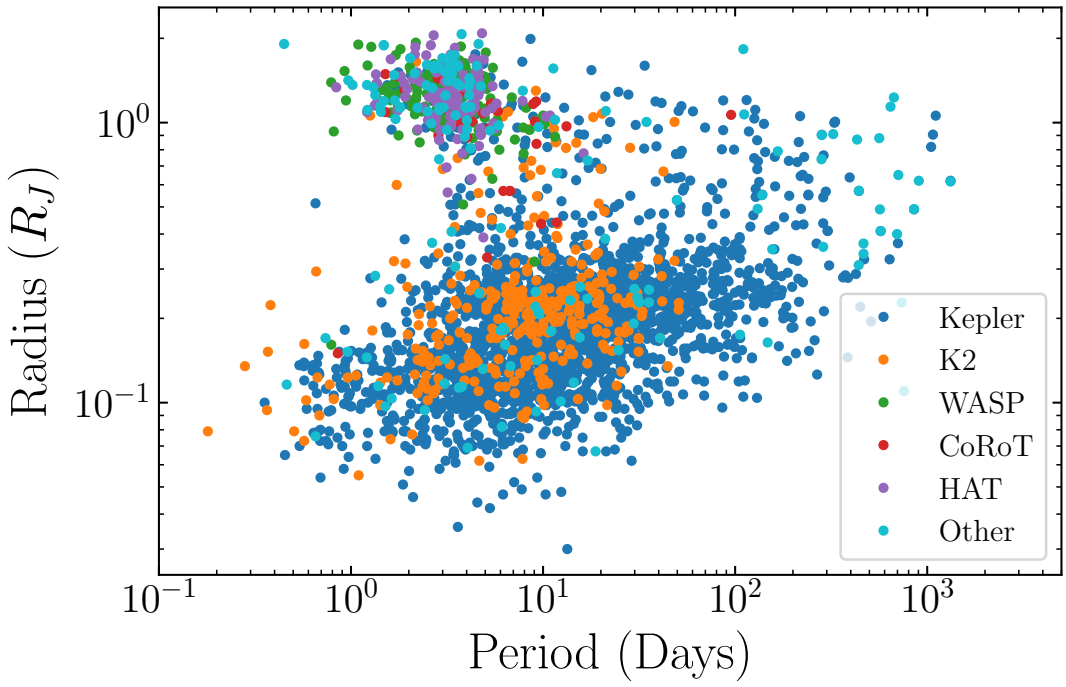

Figure 1.2: Radius vs. period for transiting exoplanets, colored by discovery mission. Hot Jupiters are the small cluster at the top left, with cooler giant planets tailing off to the right of them. Below these are the sub-Neptunes, super-Earths, and even a few roughly Earth-radius planets.

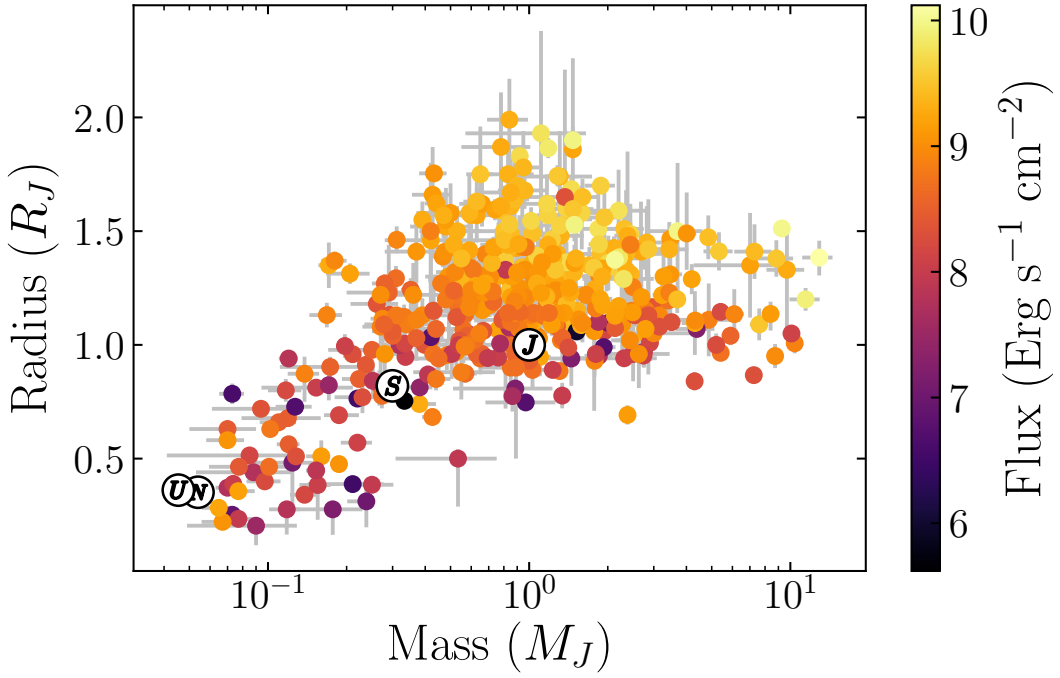

Figure 1.3: Radius vs. mass of observed giant planets, colored by incident flux. The solar system giant planets are shown as well, labeled accordingly. Note that Saturn represents a transition point between planets with smaller radii and true Jupiter-sized planets. The mass-radius relation levels off here as the planets become primarily supported by electron degeneracy pressure.

vary more in radius than more massive planets; this is because the higher gravity suppresses the effect that higher internal temperatures have on the radius.

Finally and perhaps most important is the relationship between the planet radius and flux, a term which refers to the power per unit area from light incident on the planet from its parent star(s). I highlight this in Fig. 1.4, which depicts planet radius against flux, colored by mass. It is clear that above about 2×10^8 erg s^{-1} cm^{-2} (vertical dotted line), radii are strongly correlated with incident flux, but not below this cutoff (Miller & Fortney, 2011; Demory & Seager, 2011). I'll refer to these groups as hot and cool giants respectively. Using our existing interior structure models, we would expect this flux-radius correlation to be very small

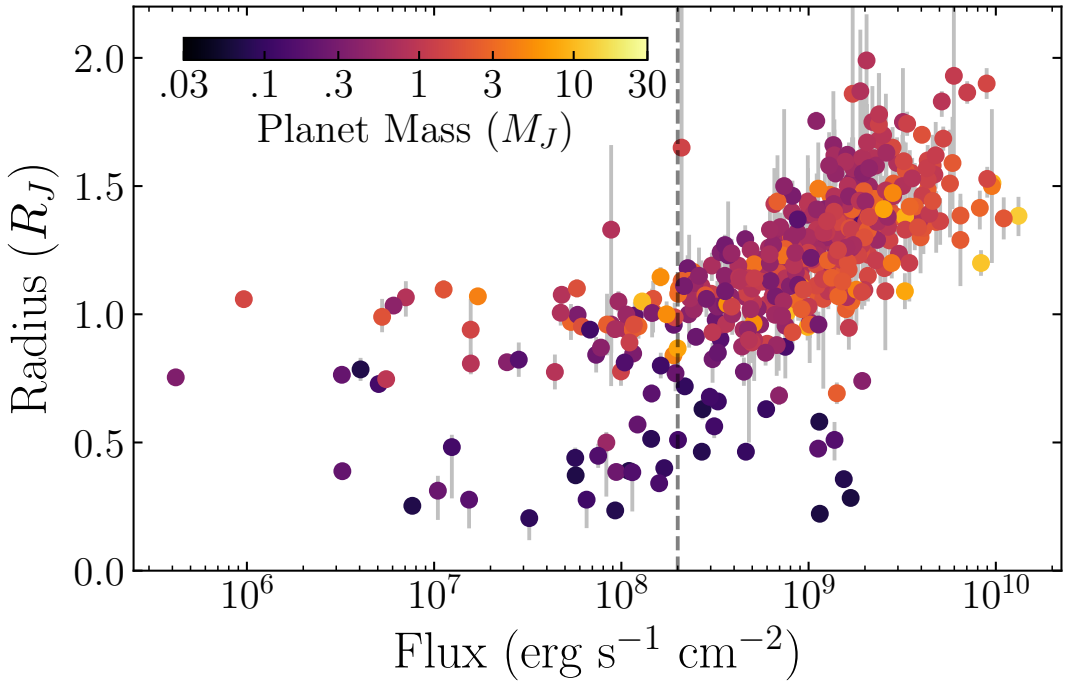

Figure 1.4: Radius vs. incident flux of the known transiting giant planets, colored by mass. The most important feature is the strong correlation between radius and flux which turns on at about 2×10^8 erg s^{-1} cm^{-2}. Note also that less massive planets have not been discovered at fluxes as high as the Jupiters, cutting off at about 2×10^9 erg s^{-1} cm^{-2}.

even for hot Jupiters. Instead, they are inflated well beyond model predictions. This problem is referred to as the hot Jupiter radius inflation effect, and has been the subject of considerable research interest. I will discuss these objects more in Chapter 3.

1.4 Interior Structure Models

Giant planets are nearly spherically symmetric, deviating only in the case of rapid rotation and tidal distortion. These deviations are small enough that giant planet interiors are well approximated by a one-dimensional (radial) model which assumes

spherical symmetry. Under these assumptions

$$\frac{dP}{dr} = -\frac{Gm(r)\rho(P,T)}{r^2} \tag{1.4}$$

$$\frac{dm}{dr} = 4\pi r^2 \rho(P,T) \tag{1.5}$$

If we assume the equation of state may be written as a power law $P = K\rho^\gamma$, these equations may be combined into the well-known Lane-Emden equation, whose solutions are known as polytropes (Kippenhahn et al., 2012; Chandrasekhar, 1939). These solutions yield complete descriptions of pressure, density, etc. as a function of radius. One particularly interesting result is that given the polytrope order $n = 1/(\gamma - 1)$, the mass-radius relation is given by

$$R \propto M^{\frac{n-1}{n-3}} \tag{1.6}$$

A pure, degenerate electron gas, such as might occur near the core of a pure hydrogen giant planet, has $n = 3/2$ (see Griffiths, 2017). However, real mixtures of hydrogen and helium are better characterized as $n \approx 1$. As such, we should expect a relatively flat relationship with mass and radius in the observed population. For cool massive planets, this is indeed the case – see again Fig. 1.3. To fully capture their behavior, however, we must use more advanced equations of state and solve them numerically.

1.4.1 Equations of State for Giant Planet Interiors

Giant planets are composed predominantly of Hydrogen and Helium, with some smaller fraction of heavier elements (which I will refer to as metals) mixed in. As such, giant planet interiors are strongly dependent on the properties of Hydrogen

and Helium at high pressures. Unfortunately, the conditions found in giant planets are difficult to probe experimentally. The extreme pressures on Hydrogen can be probed through laser-driven shock experiments (e.g. Hicks et al., 2009; Loubeyre et al., 2012). However, the path explored through temperature-pressure space due to the shock (the Hugoniot) passes through temperatures that are much higher than those of planetary interiors. Diamond anvil compression techniques (e.g. Boehler, 1993; Fei et al., 1991, for rock and iron respectively), used extensively for geophysical cases, can explore lower temperatures but struggle to achieve pressures much beyond a megabar.

For this reason, computational derivations of the equations of state are essential. The Saumon et al. (1995) equations of state for Hydrogen, Helium, and mixtures thereof have enjoyed considerable attention for their application to stars, brown dwarfs, and giant planets. These relied on semi-analytic studies of the material properties, but modern techniques have begun to replace this approach. These make use of supercomputers to run quantum molecular dynamics (QMD) simulations, which involve treating the nuclei largely as classical particles (molecular dynamics – MD) and simulating the electrons in an explicitly quantum manner, such as with density field theory (DFT). These simulations are run forward until a rough thermal equilibrium is reached and a pressure (and other parameters) are measured. This is then repeated at various temperatures and densities. Examples of this approach for H/He mixtures include Militzer & Hubbard (2013); Nettelmann et al. (2008); Chabrier et al. (2019).

These calculations and (some of the) experiments show that Hydrogen exists in an atomic or molecular state until pressures of about 1 megabar (Chabrier et al., 1992) for temperatures in the relevant range (1000-100000 K). At this point, a transition occurs to a highly-conductive, very opaque, liquid metallic state. This

phase has been long been thought to exist (Wigner & Huntington, 1935) and has subsequently been produced in the lab (Weir et al., 1996; Eremets & Troyan, 2011). In general, heavier elements readily dissolve in liquid metallic hydrogen (Wahl et al., 2013; Wilson & Militzer, 2012a,b; González-Cataldo et al., 2014). Interestingly, Helium dissolves in hydrogen for most of the relevant phase space, but will likely fall out of solution for very cool giants (Stevenson, 1975). The resulting "Helium rain" (see section 1.4.4) is thought to play a significant role in the internal structure and thermal evolution of Saturn and, to a lesser extent, Jupiter (Nettelmann et al., 2015; Mankovich et al., 2016; Hubbard & Militzer, 2016; Helled, 2018).

Similar approaches are possible for producing equations of state for heavy elements. Due to their lessened importance for giant planet interiors compared to H/He, less attention has been given to them. Nevertheless, they can still have significant effects on model results (see e.g. Miguel et al., 2016). Older analytic equations of state, such as those of Thompson (1990) and Lyon & Johnson (1992), are still commonly used. Water is probably the best studied, due to its importance for the interiors of Uranus and Neptune (Fortney et al., 2007; Nettelmann et al., 2016). In French et al. (2009) (see also Nettelmann et al., 2008), the authors use QMD to compute an equation of state for water. Figure 1.5 shows several of the aforementioned equations of state in pressure-density space.

Computing the equations of state for mixtures of materials from their separate equations of state is easy to do approximately and very hard to do exactly. The well-known additive volumes approximation (see a good discussion of it in Saumon et al., 1995) is an easy way to do this that relies on the assumption that the

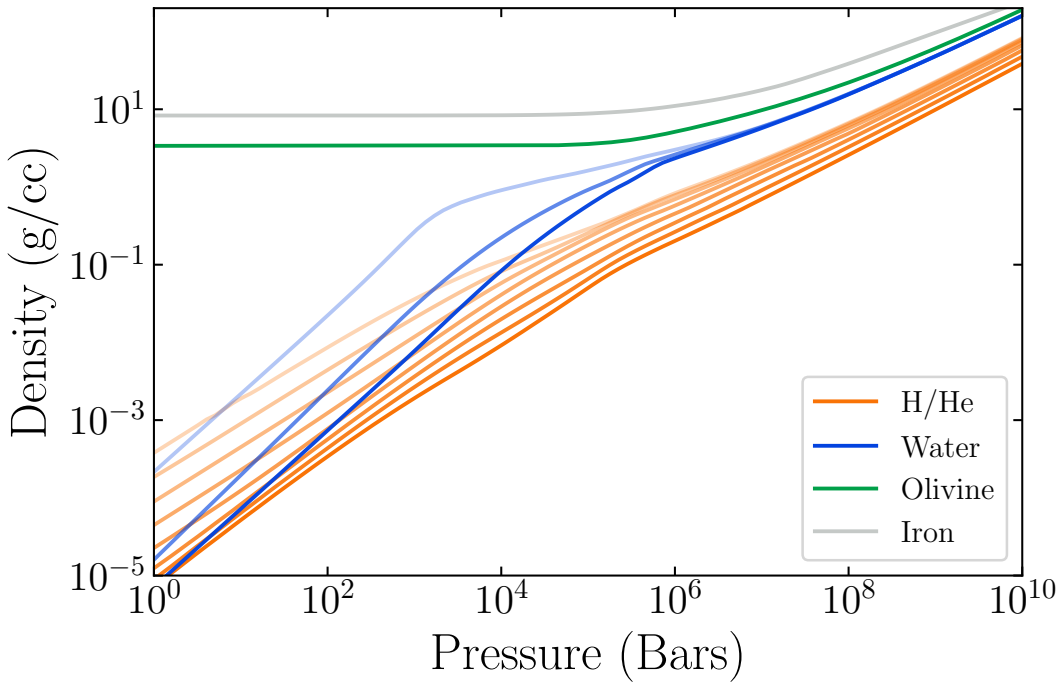

Figure 1.5: Equations of state densities vs pressure for various materials under different thermal conditions. H/He is a solar ratio mixture of Hydrogen and Helium from Chabrier et al. (2019) with specific entropies (going downwards) of 5, 6, 7, 8, 9, 10, 11, and 12 k_b/baryon. Water is the French et al. (2009) equation of state (further processed in Nettelmann et al., 2008) for 1000, 5000, and 10000 K; notice how the lines converge at around a megabar. Olivine data comes from ANEOS (Thompson, 1990) calculations, and is approximated as being independent of temperature. Iron is similarly from the SESAME database (Lyon & Johnson, 1992).

materials are non-interacting:

$$\frac{1}{\rho(P,T)} \simeq \sum_i \frac{m_i}{\rho_i(P,T)} \tag{1.7}$$

$$u(P,T) \simeq \sum_i m_i u_i(P,T) \tag{1.8}$$

$$s(P,T) \simeq s_{\text{mix}}(P,T,...) + \sum_i m_i s_i(P,T) \tag{1.9}$$

where m_i is the mass fractions of the i^{th} species, ρ is the density, u is the specific energy, and s is the specific entropy. Computing the mixture density and energy is relatively straight-forward, but the entropy is harder. In addition to the weighted sum of the component specific entropies, an entropy of mixture term must also be considered, which is a complicated function of the number of particles (including free electrons) in each species. This is not even constant across pressure and temperature, as the ionization and molecular state can change.

For most cases, the exact entropy is not important; only the relative entropy of two states. For this, we can compute the entropy differences numerically through the careful integration of basic thermodynamic relationships. For example, suppose we have computed a mixture's density $\rho(P,T)$ and specific internal energy $u(P,T)$ as a function of pressure and temperature, and we wish to compute the entropy change between two (P,T) points. First, we note that the following four partial derivatives are directly available from the numerical derivatives of our functions:

$$\left.\frac{\partial \rho}{\partial P}\right|_T \qquad \left.\frac{\partial \rho}{\partial T}\right|_P \qquad \left.\frac{\partial U}{\partial P}\right|_T \qquad \left.\frac{\partial U}{\partial T}\right|_P \tag{1.10}$$

Each of these depends on pressure and temperature, but for readability we omit the (P,T). Next, we can use the fundamental thermodynamic relation, assuming

the number of particles is constant. First, however, we must replace the extensive variables (energy U, entropy S and volume V) with intensive variables – specific energy ($u = U/M$), specific entropy ($s = S/M$), and density ($\rho = M/V$).

$$dU = TdS - PdV \tag{1.11}$$

$$\frac{dU}{M} = \frac{TdS}{M} - \frac{P}{M}\left(-\frac{Md\rho}{\rho^2}\right) \tag{1.12}$$

$$du = Tds + \frac{P}{\rho^2}d\rho \tag{1.13}$$

From this follows the intensive form of Maxwell's fourth relation:

$$\left.\frac{\partial s}{\partial P}\right|_T = \frac{1}{\rho^2}\left.\frac{\partial \rho}{\partial T}\right|_P \tag{1.14}$$

Additionally, from Eq. 1.13 one can immediately see that:

$$\left.\frac{\partial u}{\partial T}\right|_P = T\left.\frac{\partial s}{\partial T}\right|_P + \frac{P}{\rho^2}\left.\frac{\partial \rho}{\partial T}\right|_P \tag{1.15}$$

$$\left.\frac{\partial s}{\partial T}\right|_P = \frac{1}{T}\left(\left.\frac{\partial u}{\partial T}\right|_P - \frac{P}{\rho^2}\left.\frac{\partial \rho}{\partial T}\right|_P\right) \tag{1.16}$$

Equations 1.14 and 1.16 give the change in entropy with temperature and pressure but only draw on values which may be numerically computed directly from our initial functions. Thus, line integrating these equations yields the change in entropy between two (T, P) points. Alternatively, you may solve them using Euler's chain rule (the cyclic relation) for the change in temperature with pressure (or vice versa) at constant specific entropy:

$$\left.\frac{\partial T}{\partial P}\right|_s = -\frac{\left.\frac{\partial s}{\partial P}\right|_T}{\left.\frac{\partial s}{\partial T}\right|_P} = -\frac{\frac{1}{\rho^2}\left.\frac{\partial \rho}{\partial T}\right|_P}{\frac{1}{T}\left(\left.\frac{\partial u}{\partial T}\right|_P - \frac{P}{\rho^2}\left.\frac{\partial \rho}{\partial T}\right|_P\right)} \tag{1.17}$$

$$= \frac{T\left.\frac{\partial \rho}{\partial T}\right|_P}{P\left.\frac{\partial \rho}{\partial T}\right|_P - \rho^2\left.\frac{\partial u}{\partial T}\right|_P} \tag{1.18}$$

Integrating this with respect to pressure yields a pressure-temperature curve for a given adiabat. Convective regions of giant planets follow the adiabatic temperature gradient, so this can be very useful. The principal difficulty of using this approach to derive adiabats or relative entropy is that error in the equation of state accumulates the further one integrates through parameter space.

1.4.2 Numerical Solutions

Often in these cases, the mass is a given parameter but the radius is not; as such, using the mass contained within a given shell m is generally the most convenient dependent variable. This mass variable m extends from $m = 0$ at the core to $m = M$ (the total mass) at the surface. Each mass shell is associated with a particular pressure $P(m)$, density $\rho(m)$, temperature $T(m)$, and radius $r(M)$. Under this parameterization, the equations of hydrostatic equilibrium, mass conservation, and energy conservation respectively take the following forms:

$$\frac{dP}{dm} = -\frac{Gm}{4\pi r^4} \tag{1.19}$$

$$\frac{dr}{dm} = \frac{1}{4\pi r^2 \rho(P,T)} \tag{1.20}$$

$$\frac{dL}{dm} = -T\frac{ds}{dt} \tag{1.21}$$

If we assume a convective envelope, the temperature structure can be charac-

terized entirely by a uniform specific entropy s, eliminating the need for Eq. 1.21. Instead, we can parameterize the density as $\rho(P, s)$, using the results of section 1.4.1. A core can be modeled by applying a different equation of state to compute ρ below a specified mass shell m_c. For the dependent variables, the boundary conditions are $r(M), \rho(M) \geq 0$, $P(M) \approx 0$, and $r(0) = 0$. This defines a set of coupled differential equations in m that can solved numerically.

At this point, one may use standard differential equation solvers; however there is a particularly effective relaxation technique that may be applied. To use it, one first guesses an initial set of radii as a function of mass $r(m)$. Then, one must repeatedly apply the equations of hydrostatic equilibrium (Eq. 1.19), the equation of state, and mass conservation (Eq. 1.20) in sequence as follows.

$$P_n(m) = \int_0^M \frac{Gm}{4\pi r_n(m)^4} dm \tag{1.22}$$

$$\rho_n(m) = \rho(P_n(m), s, m) \tag{1.23}$$

$$r_{n+1}(m) = \left(\int_0^M \frac{3}{4\pi \rho_n(m)} dm \right)^{\frac{1}{3}} \tag{1.24}$$

Here, n is the iteration number; the procedure has converged when $r_{n+1}(m) - r_n(m)$ drops below a pre-specified error tolerance. These equations can be discretized using a standard difference equation approach. It is self-evident that the only stable solution is one in which these equations are consistent with one another. Less obvious is why this method approaches the solution rather than diverges from it. To understand this qualitatively, notice that the order in which we apply these equations mimics how a planet might adjust to disequilibrium. If the pressure in a region is too low compared to hydrostatic equilibrium, the density will decrease and the radius of the planet grows. Conversely if the pressure is too high, the density will increase and the radius will shrink. Thus the only danger

is that the correction is too large. This is not generally a problem, but if it ever were, one might adjust the update (Eq. 1.24) with a weighting $\gamma < 1$, such as:

$$r'_{n+1}(m) = (1-\gamma)r_{n+1}(m) + \gamma r_n(m) \tag{1.25}$$

where r_{n+1} is the usual updated radius and r'_{n+1} is our adjusted replacement for it.

1.4.3 Thermal Evolution

The primary avenue by which giant planets evolve (once they have finished forming), is through the radiation of their initial formation heat into space. This process is driven by heat convecting up from the interior and limited by the atmospheric opacity and (related) the surface heating from the parent star. Thus, in order to calculate the cooling rates for a planet, it is useful to precompute separate atmosphere models. For this work, we turn to Fortney et al. (2007) for a grid of atmosphere models. With some rearranging and interpolation, these give us the intrinsic temperature $T_{\rm int}$ as a function of the surface gravity g, the planet's equilibrium temperature $T_{\rm eq}$, and the specific entropy of the underlying H/He envelope s. The intrinsic temperature leads directly to the rate of heat loss from the interior $dE/dt = -4\pi R^2 \sigma_b T_{\rm int}^4$, where σ_b is the Boltzmann constant. To this one may add additional power sources, such as a hot Jupiter anomalous heating power (see chapter 3), radioactive decay heating (Vazan et al., 2018; Lopez et al., 2012), tidal dissipation, etc.

The thermal change of a convective envelope can be easily characterized by the change in its specific entropy. With the heat loss dE/dt in hand, we compute

this as follows:

$$\frac{ds}{dt} = \frac{ds}{dE}\frac{dE}{dt} = \frac{dE}{dt}\int_0^M \frac{dm}{T(m)} \tag{1.26}$$

For non-adiabatic regions, such as an isothermal core, we need only dT/dt, which is just the ratio of the heat loss to the heat capacity. There are a couple of reasonable ways to proceed from here. First, one may treat the system like a 1-d ordinary differential equation of s in t, and apply ODE solvers as usual. Alternatively, one may compute a grid of models at various specific entropies and use ds/dt afterwards to figure out how much time has elapsed between the models. This second approach is not particularly useful for simple adiabatic planets, but can simplify calculations for planets with non-adiabatic zones.

Due to the steep cooling curves of very high entropy planets, the initial specific entropy of a planet's envelope is generally unimportant beyond about 10^7 years (Fortney et al., 2007), as shown in Fig. 1.6. This is a mixed blessing. On the one hand, structure modeling of most planets can safely proceed using a large and arbitrary initial s, simplifying those computations greatly (e.g. Fortney et al., 2007; Miller et al., 2009, and chapters 2, 3 and 4). On the other hand, when we identify very young giant planets, such as Beta Pictoris b (Lagrange et al., 2009) and the HR 8799 system (Marois et al., 2008), we have very little constraint on s, making useful evolution modelling difficult. Calculating it from first principles is also difficult, and depends strongly on the opacity of the accreting gas during formation (Marley et al., 2007; Stahler et al., 1980) and thus whether significant amounts of heat are released during collapse (the "hot start" model) or not ("cold start"). Marley et al. (2007) provides one such calculation, and more recently Cumming et al. (2018) computes initial entropy as a function of depth into the planet, but significant uncertainties remain. More observational data on these

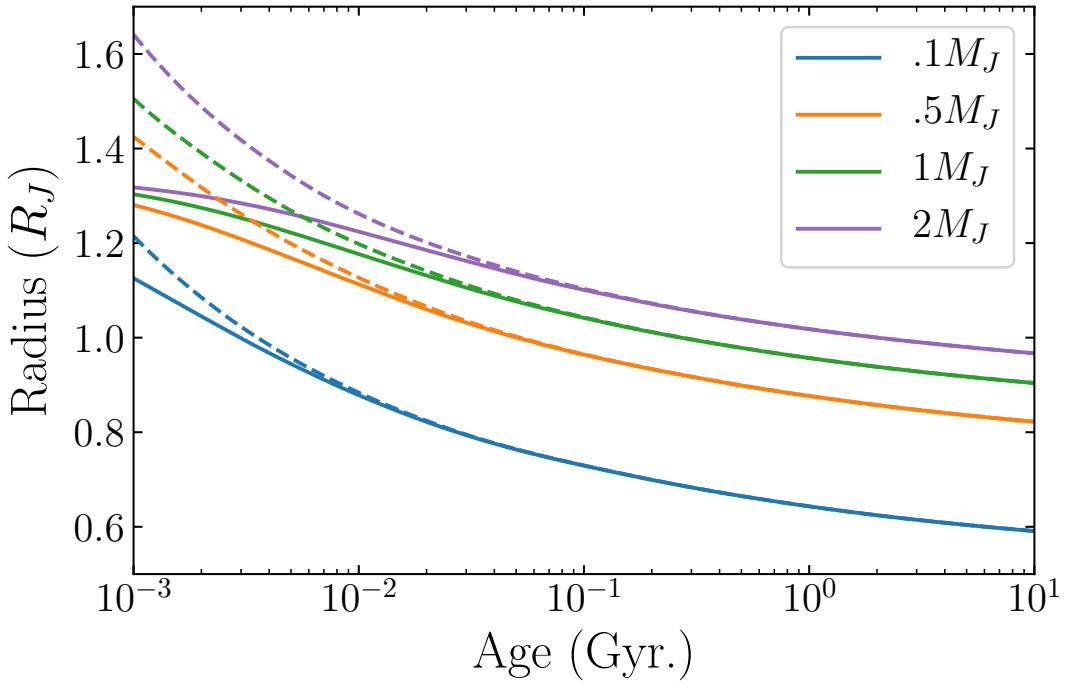

Figure 1.6: The radius evolution of giant planets, varying the mass, composition, and initial entropy. The solid and dotted lines indicate initial specific entropies of 9 and 12 k_b/baryon respectively. Note how this has little effect on the radius after 100 Myr. The composition was set by the median value from the mass-metallicity relationship to be discussed in Chapter 2; the compositions (and therefore radii) of real planets vary. This figure was based on figures in Fortney et al. (2007); Marley et al. (2007).

objects would be extremely helpful at this point, perhaps through more direct imaging discoveries, spectroscopic follow-up, and astrometry of their parent stars.

1.4.4 Alternative Thermal Structures

Traditional models of giant planet interiors posit that these objects are structured into a heavy-element core and a convective, primarily H/He envelope. This model has been applied successfully to both solar system and exoplanet cases. However, as observations give us more information, we have begun to consider refinements to this model.

Helium rain is one such case. While studying mixtures of hydrogen and helium (Stevenson & Salpeter, 1977b), Stevenson & Salpeter (1977a) noticed that at high pressure and sufficiently low temperatures, helium may precipitate out of solution from liquid metallic hydrogen. Importantly, these conditions (see Mazzola et al., 2018) definitely occur in Saturn and very likely (but to a lesser extent) in Jupiter as well (Guillot et al., 2004). This implies that in each planet some amount of helium will have precipitated down onto a layer on top of the core. Voyager measurements of Saturn's helium abundance (Conrath & Gautier, 2000) support this, finding a significant depletion of atmosphere helium relative to the protosolar abundance. Likewise the Galileo Entry Probe found that the helium abundance in Jupiter (von Zahn et al., 1998) was slightly below the protosolar value. Neon, which is thought to dissolve in helium better than in hydrogen, was observed to be similarly depleted (Niemann et al., 1998), suggesting that it is sequestered in a helium rich layer in the planetary interior (e.g. Hubbard et al., 2002). This helium rain effect is believed to have significant effects on the layering structure and luminosity of these planets (Nettelmann et al., 2013; Mankovich et al., 2016, e.g.). Extrasolar giant planets discovered so far, however, are usually too hot to

exhibit this effect.

Another potential change to the usual interior structure models is the inclusion of radiative zones and double-diffusive convection. If composition gradients exist in a planet, these may inhibit convection and significantly reduce the rate at which heat can escape the planet (Chabrier & Baraffe, 2007; Leconte & Chabrier, 2012; Nettelmann et al., 2013). However, where convection does occur it will quickly mix the material, flattening the composition gradient and enforcing an adiabatic temperature gradient.

Determining which of these cases occurs relies on comparing the temperature gradient of the planet ∇ with the adiabatic temperature gradient ∇_a, and a composition-based correction term ∇_z, which is defined as:

$$\nabla_z \equiv \frac{\partial \ln(T)}{\partial Z} \frac{dZ}{d \ln(P)} \tag{1.27}$$

Convection occurs when the Ledoux criterion (Ledoux, 1947), $\nabla < \nabla_a + \nabla_z$, is *not* satisfied. Similarly, when the Schwarzchild criterion, $\nabla < \nabla_a$ is met, the region is radiative. In between these cases, when $\nabla_a < \nabla < \nabla_a + \nabla_z$, the fluid will exhibit semi-convection. For the fluid properties found in giant planets, this generally means layered convection, in which well-mixed convective layers are separated by thin radiative zones with steep composition and temperature gradients (Chabrier & Baraffe, 2007).

Due primarily to the difficulty of correctly handling semi-convection, modelling the evolution of planets with these possibilities in mind is the subject of ongoing research. Due to the billion-year timescales of planetary evolution, it is often necessary to use 1-dimensional models (e.g. Vazan et al., 2015, 2016). Still, because it is difficult to treat layered convection in purely 1-d, it is helpful to refer to 3-d models (Moll et al., 2017; Wood et al., 2013, e.g.) and first-principles

fluid property simulations (such as French et al., 2012). Finally, it appears that the present-day thermal structure of a planet may depend significantly on the initial composition (Lozovsky et al., 2017) and thermal structure (Cumming et al., 2018).

1.5 Bayesian Statistics

For much of this work, I'll be making use of Bayesian statistics to study various aspects of giant planet physics. These techniques can be seen as a flexible alternative to traditional frequentist statistics. The strategy is to begin with prior beliefs about a parameter and update these in light of collected data. This process may be rigorously defined by applying the rules of conditional probability via Bayes' law. If we write the parameter(s) of interest as θ and the relevant data as y (both can be vectors), this may be written as:

$$p(\theta|y) = \frac{p(y|\theta)p(\theta)}{p(y)} \tag{1.28}$$

Here, our prior distribution $p(\theta)$ is updated using the likelihood $p(y|\theta)$ and normalized by $p(y) = \int p(y|\theta)p(\theta)d\theta$ to yield the posterior probability distribution $p(\theta|y)$. The likelihood is the probability of obtaining the data y for a given value of θ; choosing a functional form is generally the first step of the modelling procedure. For example, we can measure the rate λ of a Poisson process (e.g. radioactive decays) using the likelihood Poisson$(n|\lambda, t)$; for a uniform prior $\lambda \propto 1$, observing n counts in t time gives a posterior distribution $p(\lambda|n, t) \sim \Gamma(1 + n, t)$. The symbol $\sim$ indicates that the variable to the left is distributed as the distribution to the right, and Γ is the Gamma distribution parameterized by rate.

The most common concern raised about this approach is the difficulty in se-

lecting a prior, which is often less well-motivated than the form of the likelihood. For these cases, one may apply a weakly-informative prior (see Yang & Berger, 1996), such as the uniform (as above) and Jeffrey's priors (Jeffreys, 1946). Sometimes these take the form of improper priors, where $\int p(\theta)d\theta$ is not finite; this is in general not a problem so long as $p(y)$ remains finite. From a philosophical perspective, one may take issue with the lack of objectivity from an arbitrary choice of prior. However, this prior may be seen as stating assumptions explicitly which had been left implicit in the frequentist approach, e.g. through the parameterization of θ. In fact, when a frequentist approach can be applied to a problem, its results are often equivalent to the Bayesian approach for some particular choice of prior. Ultimately, the practical approach is to only believe results of an inference if they do not differ much between reasonable choices of the prior.

Another important issue in Bayesian statistics is that of model selection, in which we wish to weigh different forms of the likelihood (or different spaces of θ) against one another. A uniquely well-motivated approach (Jeffreys, 1935) is to compare each model's $p(y)$, often called the Bayes evidence. This arises from considering one's belief in each model to be a parameter that itself must be updated; the ratio of posterior model probabilities is the ratio of the model evidences, known as the Bayes factor (see Kass & Raftery, 1995). Unfortunately, taking this approach can be quite sensitive to the choice of prior (see discussion in Gelman et al., 2014a), especially for continuous distributions with weakly-informative priors. As such, I do not use Bayes factors in this work.

Perhaps the best known alternative to the Bayes factor is the Bayesian information criterion (BIC). This is an approximation to the Bayes factor (Schwarz, 1978), which is less sensitive to the choice of prior. One may instead consider the predictive power of a model, for which the Akaike information criterion (AIC;

Akaike, 1974) was developed. Several other selection criteria have since been devloped (Gelman et al., 2014b), such as the deviance information criterion (DIC; Spiegelhalter et al., 2002). In all of these cases, the model with the lower (often more negative) score is favored. There is not a consensus on which criterion is preferred, perhaps because in most practical cases they yield the same results.

2. The Mass-Metallicity Relation

2.1 Introduction

Giant planets do not directly take on the composition of their parent stars. If some flavor of core-accretion formation is correct (Pollack et al., 1996), then a seed core of $\sim 5 - 10 M_{\oplus}$ of ice/rock must build up first, which begins accreting nebular gas. The gas need not share the exact composition of the parent star, due to condensation and migration of solids within the disk (Lodders, 2009; Öberg et al., 2011). The growing giant planet accretes gas but is also bombarded by planetesimals, which may add to the core mass or dissolve into the growing H/He envelope. The amounts and variety of heavy elements (metals) accreted by the growing planet will depend on its formation location, formation time, disk environments sampled, and whether it forms near neighboring planets, among many other factors. A planet's present-day composition is our indirect window into its formation process.

The observed atmospheric composition of fully convective giant planets reflect the mixing ratios of heavy elements within their whole H/He envelope (with some caveats – see §2.3.1). Spectroscopy of the Solar System's giants points to enhancements in the mixing ratio of carbon (as seen in CH_4) of ∼4, 10, 80, and 80, in Jupiter, Saturn, Uranus, and Neptune, respectively (Wong et al., 2004;

Fletcher et al., 2009). The *Galileo Entry Probe* found that Jupiter's atmosphere is enhanced in volatiles like C, N, S, and noble gases by factors of 2-5 compared to the Sun (Wong et al., 2004).

Remarkably, one can make inferences about the *bulk* metallicity, or heavy element enhancement, $Z_{\rm planet}$ $/Z_{\rm Sun}$, of a Solar System giant planet by measuring only its mass and radius. These results are consistent with and refined by measurements of their gravitational moments. By comparing to structure models, it is straightforward to infer from mass and radius alone that Jupiter and Saturn are both smaller and denser than they would be if they were composed of solar composition material (Zapolsky & Salpeter, 1969; Fortney et al., 2007). Therefore, we can infer they are enhanced in heavy elements. As we describe below, this leads to an immediate connection with transiting giant planets, where mass and radius can be accurately measured.

Knowledge of the heavy element enrichment of our Solar System's giant planets has led to dramatic advances in our understanding of planet formation. Models of the core-accretion model of planet formation have advanced to the point where they can match the heavy element enrichment of each of the Solar System's giant planets (Alibert et al., 2005; Lissauer et al., 2009; Helled & Bodenheimer, 2014). However, we are only beginning to attain similar data for exoplanets, which will provide a critical check for planet formation models over a tremendously larger phase space. Such constraints are particularly important for comparison with planetary population synthesis models that aim to understand the processes of core formation, H/He envelope accretion, and planetary migration, in diverse protoplanetary environments (Ida & Lin, 2004; Mordasini et al., 2014). Constraints on planet formation from exoplanetary systems have been almost entirely driven by data on the frequency of planets in the mass/semi-major axis plane. A

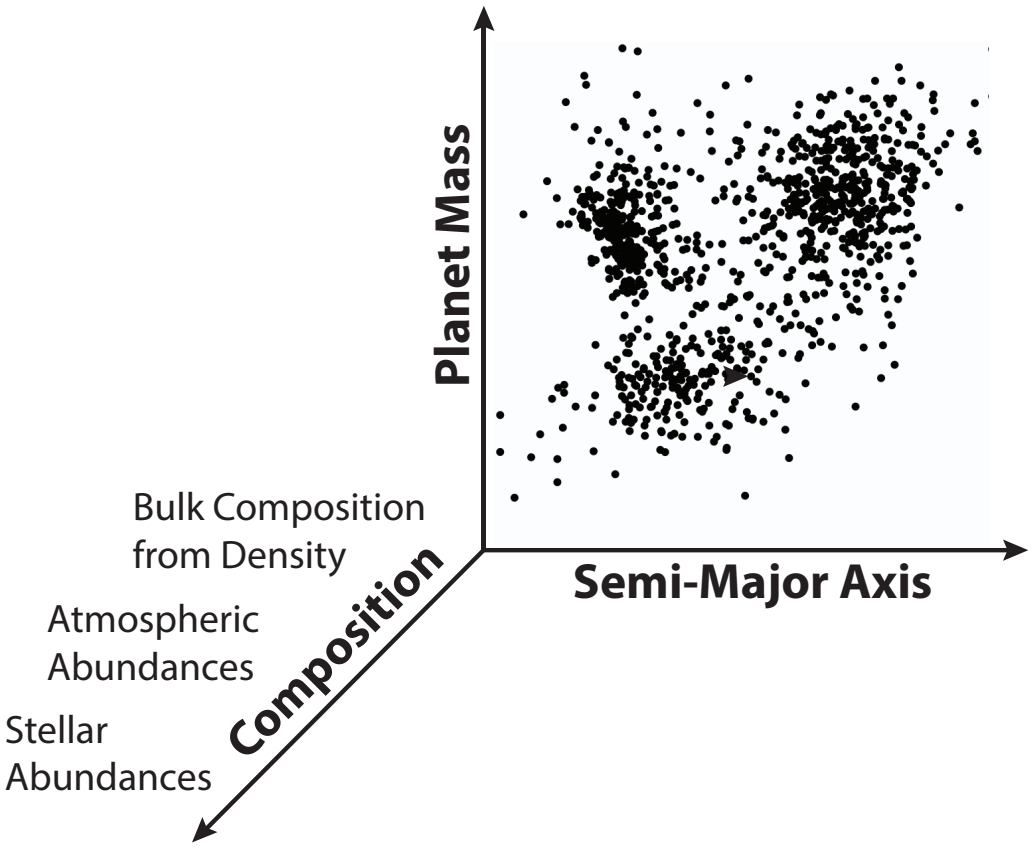

Figure 2.1: A highly schematic and simplified view of planes useful for understanding planet formation. The main purpose of this study is to provide planetary composition information to inform planet formation models.

promising avenue is to move these comparisons into a complementary plane, that of planetary composition, either in bulk composition (Guillot et al., 2006; Burrows et al., 2007; Miller & Fortney, 2011; Mordasini et al., 2014), or atmospheric composition (Madhusudhan et al., 2011; Fortney et al., 2013; Kreidberg et al., 2014b; Barman et al., 2015; Konopacky et al., 2013) as shown in a schematic way in Figure 2.1.

The dramatic rise in the number of observed transiting exoplanets provides a unique opportunity. With radii derived from transit observations and masses derived from radial-velocity or transit-timing variation measurements, we get es-

pecially detailed information about these objects. This gives us a measured density, and therefore some rough information about their bulk composition. A more advanced analysis uses models of planet structural evolution (e.g. Fortney et al. (2007)) to constrain the quantity of heavy elements.

Most of the giant planets we have observed are strongly irradiated hot Jupiters, whose radii are inflated beyond what models predict. Much effort has been put into understanding this discrepancy. A thorough discussion is outside the scope of this chapter, but the various proposed inflation mechanisms are extensively reviewed in Fortney et al. (2010), Baraffe et al. (2014), and Weiss et al. (2013). Unfortunately, without a definite understanding of the inflation process this acts as a free parameter in modeling: the inflationary effect enlarges a planet and added heavy elements shrink it, resulting in a degeneracy that inhibits our ability to obtain useful composition constraints. Still, work has been done to use models to address a the star-planet composition connection, using plausible assumptions about the effect, as a heat source (Guillot et al., 2006) or as a slowed-cooling effect (Burrows et al., 2007). Both studies saw an increase in planet heavy element mass with stellar metallicity.

A promising avenue of investigation are the sample of transiting exoplanets which are relatively cool. Planets that receive an incident flux below around 2×10^8 erg s^{-1} cm^{-2} ($T_{\rm eq} \lesssim 1000$ K) appear to be non-inflated (Miller & Fortney, 2011; Demory & Seager, 2011), obviating the need for assumptions about that effect. Figure 2.2 shows this threshold. Miller & Fortney (2011) (hereafter referred to as MF2011) studied these planets, finding correlations in the heavy element mass with planetary mass and stellar metallicity. In particular, they noted a strong connection between the relative enrichment of planets relative to their parent stars ($Z_{\rm planet}/Z_{\rm star}$) and the planet mass. However, that study was limited

by a small sample size of 14 planets.

In our work that follows, we consider the set of cool transiting giant planets, now numbering 47, and compare them to a new grid of evolution models to estimate their heavy element masses, and we include a more sophisticated treatment of the uncertainties on our derived planetary metal-enrichments. We then examine the connections between their mass, metal content, and parent star metallicity.

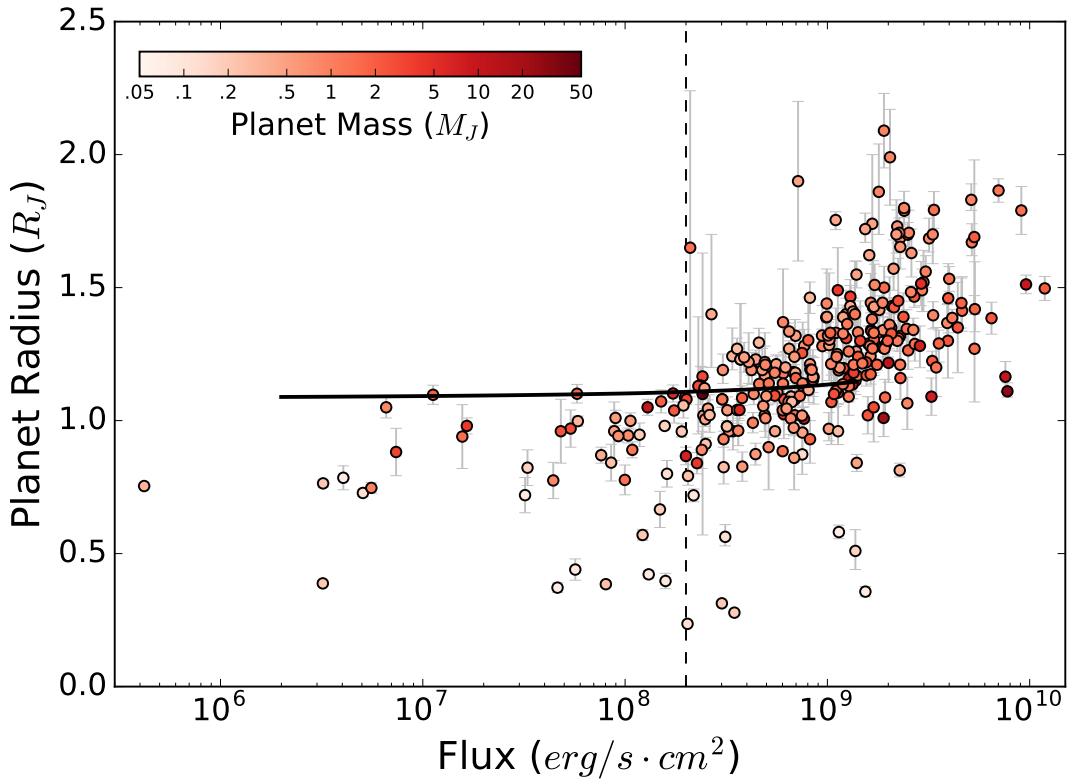

Figure 2.2: Planetary radii for observed planets against stellar insolation. The black line is an 4.5 Gyr., 1 $M_{\rm J}$ pure H/He object, roughly the maximum radius for older, uninflated planets. The dashed vertical line marks the flux cutoff we use to identify the cool, uninflated giants.

2.2 Planet Data and Selection

Our data was downloaded from the Extrasolar Planets Encyclopedia (exoplanets.eu, Schneider et al., 2011)) and the NASA Exoplanet Archive (Akeson et al., 2013). These data were combined, filtered (see below) and checked against sources for accuracy. Some corrections were needed, mostly in resolving differing values between sources; we aimed to consistently use the most complete and up-to-date sources. We tried to include all known planets who met the selection (even if some of their data was found in the literature and not the websites). Critically, we use data from the original sources, rather than the websites (see Table 1).

For our sample, we selected the cool giant planets that had well-determined properties. Typically, this means they were the subject of both transit and radial velocity studies. The mass and radius uncertainties were of particular importance. Planets needed to have masses between $20M_{\oplus}$ and $20M_J$, and relative uncertainties thereof below 50%. Our sample's relative mass uncertainties were typically well below that cutoff, distributed as $10^{+12.8}_{-5.7}$%. We also constrained relative radius uncertainty to less than 50%, but again saw values much lower ($5.0^{+4.6}_{-2.5}$%). Both uncertainty cuts were made to eliminate planets with only rough estimates or upper limits for either value.

As discussed in §2.1, we used a 2×10^8 erg s^{-1} cm^{-2} upper flux cutoff to filter out potentially inflated planets. Consequently, candidates needed to have enough information to compute the time-averaged flux: stellar radius and effective temperature (for both stars, if binary), semi-major axis, and eccentricity. In addition, we needed measured values for the stellar metallicities in the form of the iron abundance [Fe/H]. These tended to have fairly high uncertainties, and were a major source of error in our determination of $Z_{\rm planet}/Z_{\rm star}$.

#	Name	Mass ($M_{\rm J}$)	Radius ($R_{\rm J}$)	Age (Gyr.)	Flux	[Fe/H] (Dex)	Metal ($M_{\oplus}$)	Z_p	Z_p/Z_s
1	CoRoT-8 b	0.22 ± 0.03	0.57 ± 0.02	$0.1 - 3.0$	$1.22 \cdot 10^{8}$	0.30 ± 0.10	$45.91^{+6.99}_{-6.83}$	0.66 ± 0.03	$24.18^{+5.00}_{-6.67}$
2†	CoRoT-9 b	0.84 ± 0.07	1.05 ± 0.04	$1.0 - 8.0$	$6.59 \cdot 10^{6}$	-0.01 ± 0.06	$18.87^{+13.30}_{-18.77}$	$0.07^{+0.04}_{-0.07}$	$5.21^{+2.81}_{-5.21}$
3	CoRoT-10 b	2.75 ± 0.16	0.97 ± 0.07	$0.1 - 3.0$	$5.38 \cdot 10^{7}$	0.26 ± 0.07	$202.98^{+84.09}_{-78.08}$	0.23 ± 0.09	$9.26^{+3.63}_{-4.44}$
4	CoRoT-24 c	0.09 ± 0.04	0.44 ± 0.04	$8.0 - 14.0$	$5.67 \cdot 10^{7}$	0.30 ± 0.15	$21.64^{+9.38}_{-8.17}$	0.77 ± 0.06	$29.18^{+8.55}_{-13.28}$
5	GJ 436 b	0.07 ± 0.01	0.37 ± 0.02	$0.5 - 10.0$	$4.63 \cdot 10^{7}$	-0.32 ± 0.12	$20.07^{+1.68}_{-1.62}$	0.85 ± 0.03	$132.02^{+31.66}_{-43.68}$
6	HAT-P-11 b	0.08 ± 0.01	0.42 ± 0.01	$2.4 - 12.4$	$1.31 \cdot 10^{8}$	0.31 ± 0.05	$20.31^{+2.45}_{-2.36}$	0.79 ± 0.02	$27.76^{+3.09}_{-3.56}$
7	HAT-P-12 b	0.21 ± 0.01	$0.96^{+0.03}_{-0.02}$	$0.5 - 4.5$	$1.91 \cdot 10^{8}$	-0.29 ± 0.05	$11.83^{+3.17}_{-3.23}$	0.18 ± 0.05	$24.75^{+6.92}_{-7.43}$
8†	HAT-P-15 b	1.95 ± 0.07	1.07 ± 0.04	$5.2 - 9.3$	$1.51 \cdot 10^{8}$	0.22 ± 0.08	$42.45^{+30.67}_{-42.35}$	$0.07^{+0.04}_{-0.07}$	$3.00^{+1.65}_{-3.00}$
9	HAT-P-17 b	0.53 ± 0.02	1.01 ± 0.03	$4.5 - 11.1$	$8.97 \cdot 10^{7}$	0.00 ± 0.08	$14.08^{+6.56}_{-6.24}$	0.08 ± 0.04	$6.02^{+2.72}_{-3.25}$
10	HAT-P-18 b	0.18 ± 0.03	0.95 ± 0.04	$6.0 - 16.8$	$1.18 \cdot 10^{8}$	0.10 ± 0.08	$6.08^{+4.35}_{-3.29}$	$0.10^{+0.05}_{-0.06}$	$5.88^{+3.11}_{-4.06}$
11	HAT-P-20 b	7.25 ± 0.19	0.87 ± 0.03	$2.9 - 12.4$	$2.00 \cdot 10^{8}$	0.35 ± 0.08	$662.48^{+111.85}_{-109.11}$	0.29 ± 0.05	$9.35^{+2.06}_{-2.66}$
12	HAT-P-54 b	0.76 ± 0.03	0.94 ± 0.03	$1.8 - 8.2$	$1.04 \cdot 10^{8}$	-0.13 ± 0.08	$47.33^{+9.60}_{-9.22}$	0.20 ± 0.04	$19.06^{+4.54}_{-5.80}$
13	HATS-6 b	0.32 ± 0.07	1.00 ± 0.02	$0.1 - 13.7$	$5.84 \cdot 10^{7}$	0.20 ± 0.09	$8.67^{+7.17}_{-4.70}$	$0.08^{+0.04}_{-0.06}$	$3.80^{+1.98}_{-3.24}$
14	HATS-17 b	1.34 ± 0.07	0.78 ± 0.06	$0.8 - 3.4$	$9.97 \cdot 10^{7}$	0.30 ± 0.03	$196.42^{+35.50}_{-34.17}$	0.46 ± 0.08	$16.56^{+2.93}_{-3.12}$
15	HD 17156 b	3.19 ± 0.03	1.09 ± 0.01	$2.4 - 3.8$	$1.98 \cdot 10^{8}$	0.24 ± 0.05	$58.84^{+8.81}_{-8.75}$	0.06 ± 0.01	$2.40^{+0.43}_{-0.49}$
16	HD 80606 b	3.94 ± 0.11	0.98 ± 0.03	$1.7 - 7.6$	$1.65 \cdot 10^{7}$	0.43 ± 0.03	$215.69^{+52.63}_{-52.23}$	0.17 ± 0.04	$4.58^{+1.13}_{-1.19}$
17	K2-19 b	$0.19^{+0.02}_{-0.04}$	0.67 ± 0.07	$8.0 - 14.0$	$1.49 \cdot 10^{8}$	0.19 ± 0.12	$28.72^{+9.21}_{-7.56}$	0.48 ± 0.09	$22.99^{+6.59}_{-9.31}$
18	K2-24 b	0.06 ± 0.01	0.52 ± 0.05	$1.3 - 8.9$	$8.24 \cdot 10^{7}$	0.42 ± 0.04	$13.38^{+3.30}_{-2.86}$	0.68 ± 0.06	$18.44^{+2.27}_{-2.56}$
19	K2-24 c	0.08 ± 0.02	0.72 ± 0.07	$1.3 - 8.9$	$3.20 \cdot 10^{7}$	0.42 ± 0.04	$10.81^{+3.55}_{-3.32}$	$0.42^{+0.10}_{-0.09}$	11.33 ± 2.73
20	K2-27 b	0.09 ± 0.02	0.40 ± 0.03	$0.5 - 10.0$	$1.58 \cdot 10^{8}$	0.14 ± 0.07	$24.40^{+6.86}_{-6.42}$	0.84 ± 0.04	$43.88^{+6.65}_{-8.19}$
21	Kepler-9 b	0.25 ± 0.01	0.84 ± 0.07	$2.0 - 4.0$	$8.53 \cdot 10^{7}$	0.12 ± 0.04	$23.63^{+7.15}_{-6.80}$	$0.30^{+0.08}_{-0.09}$	$16.06^{+4.69}_{-5.11}$
22	Kepler-9 c	0.17 ± 0.01	0.82 ± 0.07	$2.0 - 4.0$	$3.29 \cdot 10^{7}$	0.12 ± 0.04	$16.14^{+4.81}_{-4.58}$	0.30 ± 0.08	$16.17^{+4.61}_{-4.95}$
23*	Kepler-16 b	0.33 ± 0.02	0.75 ± 0.00	$0.5 - 10.0$	$4.19 \cdot 10^{5}$	-0.30 ± 0.20	$41.49^{+3.11}_{-2.78}$	$0.39^{+0.01}_{-0.02}$	$62.05^{+22.31}_{-40.47}$
24†	Kepler-30 c	2.01 ± 0.16	1.10 ± 0.04	$0.2 - 3.8$	$1.12 \cdot 10^{7}$	0.18 ± 0.27	$42.54^{+30.62}_{-42.44}$	$0.07^{+0.04}_{-0.07}$	$3.81^{+2.30}_{-3.81}$
25	Kepler-30 d	0.07 ± 0.01	0.79 ± 0.04	$0.2 - 3.8$	$4.05 \cdot 10^{6}$	0.18 ± 0.27	$8.70^{+1.95}_{-2.02}$	$0.38^{+0.08}_{-0.07}$	$21.39^{+10.03}_{-21.53}$
26*	Kepler-34 b	0.22 ± 0.01	0.76 ± 0.01	$5.0 - 6.0$	$3.21 \cdot 10^{6}$	-0.07 ± 0.15	$24.42^{+1.97}_{-1.90}$	0.35 ± 0.02	$31.24^{+8.98}_{-14.14}$
27*	Kepler-35 b	0.13 ± 0.02	0.73 ± 0.01	$8.0 - 12.$	$5.06 \cdot 10^{6}$	-0.34 ± 0.20	$14.56^{+2.62}_{-2.40}$	0.36 ± 0.02	$62.22^{+21.89}_{-38.71}$
28	Kepler-45 b	0.51 ± 0.09	0.96 ± 0.11	$0.4 - 1.5$	$8.83 \cdot 10^{7}$	0.28 ± 0.14	$37.08^{+23.05}_{-17.71}$	$0.23^{+0.11}_{-0.12}$	$9.12^{+4.46}_{-7.11}$
29†	Kepler-75 b	10.10 ± 0.40	1.05 ± 0.03	$3.4 - 9.7$	$1.29 \cdot 10^{8}$	0.30 ± 0.12	$0.00^{+133.99}_{-0.00}$	$0.00^{+0.04}_{-0.00}$	$0.00^{+10.84}_{-0.00}$
30	Kepler-89 d	0.16 ± 0.02	0.98 ± 0.01	$3.7 - 4.2$	$1.57 \cdot 10^{8}$	0.01 ± 0.04	$5.25^{+1.23}_{-1.10}$	0.10 ± 0.01	$7.02^{+1.10}_{-1.21}$
31†	Kepler-117 c	1.84 ± 0.18	1.10 ± 0.04	$3.9 - 6.7$	$5.79 \cdot 10^{7}$	-0.04 ± 0.10	$25.14^{+22.10}_{-25.04}$	$0.04^{+0.02}_{-0.04}$	$3.44^{+2.02}_{-3.44}$
32	Kepler-145 c	0.25 ± 0.05	0.39 ± 0.01	$2.1 - 3.1$	$8.03 \cdot 10^{7}$	0.13 ± 0.10	$73.86^{+17.21}_{-16.42}$	0.92 ± 0.03	$50.39^{+10.20}_{-13.43}$

33*	Kepler-413 b	0.21 ± 0.07	0.39 ± 0.01	$0.5 - 10.0$	$3.20 \cdot 10^6$	-0.20 ± 0.20	$60.44^{+21.91}_{-20.85}$	$0.89^{+0.04}_{-0.03}$	$112.32^{+40.09}_{-70.60}$
34	Kepler-419 b	2.50 ± 0.30	0.96 ± 0.12	$1.6 - 4.1$	$4.81 \cdot 10^7$	0.09 ± 0.15	$198.16^{+126.80}_{-100.72}$	$0.25^{+0.13}_{-0.15}$	$15.41^{+8.16}_{-13.45}$
35	Kepler-420 b	1.45 ± 0.35	0.94 ± 0.12	$6.3 - 12.3$	$1.57 \cdot 10^7$	0.27 ± 0.09	$110.51^{+88.89}_{-59.61}$	$0.24^{+0.12}_{-0.16}$	$9.25^{+4.90}_{-7.07}$
36†	Kepler-432 b	5.84 ± 0.05	1.10 ± 0.03	$2.6 - 4.2$	$1.73 \cdot 10^8$	-0.02 ± 0.06	$67.39^{+60.95}_{-67.29}$	$0.04^{+0.02}_{-0.04}$	$2.74^{+1.61}_{-2.74}$
37	Kepler-539 b	0.97 ± 0.29	0.75 ± 0.02	$0.4 - 1.2$	$5.54 \cdot 10^6$	-0.01 ± 0.07	$154.94^{+51.90}_{-48.76}$	0.50 ± 0.03	$36.74^{+5.75}_{-7.07}$
38*	Kepler-1647 b	1.52 ± 0.65	1.06 ± 0.01	$3.9 - 4.9$	$7.91 \cdot 10^5$	-0.14 ± 0.05	$29.22^{+19.76}_{-15.14}$	0.05 ± 0.02	$5.34^{+2.10}_{-2.11}$
39	WASP-8 b	$2.24^{+0.08}_{-0.09}$	$1.04^{+0.01}_{-0.05}$	$3.0 - 5.0$	$1.75 \cdot 10^8$	0.17 ± 0.07	$84.34^{+43.33}_{-38.00}$	$0.12^{+0.05}_{-0.06}$	$5.79^{+2.65}_{-3.27}$
40	WASP-29 b	0.24 ± 0.02	$0.79^{+0.06}_{-0.04}$	$7.0 - 13.0$	$2.05 \cdot 10^8$	0.11 ± 0.14	$25.65^{+6.63}_{-6.09}$	$0.33^{+0.07}_{-0.08}$	$19.28^{+6.18}_{-9.52}$
41	WASP-59 b	0.86 ± 0.04	0.78 ± 0.07	$0.1 - 1.2$	$4.41 \cdot 10^7$	-0.15 ± 0.11	$128.37^{+26.73}_{-25.06}$	0.47 ± 0.09	$48.78^{+13.21}_{-18.26}$
42†	WASP-69 b	0.26 ± 0.02	1.06 ± 0.05	$0.5 - 4.0$	$1.94 \cdot 10^8$	0.14 ± 0.08	$7.23^{+4.96}_{-7.13}$	$0.09^{+0.05}_{-0.09}$	$4.56^{+2.56}_{-4.56}$
43	WASP-80 b	0.54 ± 0.04	1.00 ± 0.03	$0.5 - 10.0$	$1.06 \cdot 10^8$	$-0.13^{+0.15}_{-0.17}$	$20.31^{+8.47}_{-7.74}$	$0.12^{+0.04}_{-0.05}$	$12.28^{+5.37}_{-8.82}$
44	WASP-84 b	0.69 ± 0.03	0.94 ± 0.02	$0.4 - 1.4$	$9.26 \cdot 10^7$	0.00 ± 0.10	$53.82^{+6.79}_{-6.48}$	0.24 ± 0.03	$17.88^{+4.00}_{-5.38}$
45	WASP-130 b	1.23 ± 0.04	0.89 ± 0.03	$2.0 - 14.0$	$1.09 \cdot 10^8$	0.26 ± 0.10	$108.83^{+17.58}_{-17.35}$	0.28 ± 0.04	$11.22^{+2.74}_{-3.63}$
46	WASP-132 b	0.41 ± 0.03	0.87 ± 0.03	$0.5 - 14.0$	$7.62 \cdot 10^7$	0.22 ± 0.13	$33.70^{+6.87}_{-6.40}$	0.26 ± 0.05	$11.63^{+3.38}_{-4.92}$
47	WASP-139 b	0.12 ± 0.02	0.80 ± 0.05	$0.3 - 1.0$	$1.61 \cdot 10^8$	0.20 ± 0.09	$15.64^{+2.93}_{-2.48}$	0.42 ± 0.05	$19.40^{+4.07}_{-5.31}$

Table 2.1: A * indicates circumbinary planets. A † indicates those planets with results adjusted to reflect the fact that a certain portion of their samples could not be modeled (see §2.4 for discussion). Flux is in units of Gerg s^{-1} cm^{-2}. Sources – 1: Bordé et al. (2010), 2: Deeg et al. (2010), 3: Bonomo et al. (2010), 4: Ford et al. (2012), 5: Bean et al. (2006); Southworth (2010), 6: Bakos et al. (2010), 7: Hartman et al. (2011b), 8: Kovács et al. (2010), 9: Howard et al. (2012), 10: (Hartman et al., 2011b), 11: Bakos et al. (2011), 12: Bakos et al. (2015), 13: Hartman et al. (2015), 14: Brahm et al. (2016), 15: Nutzman et al. (2011), 16: Pont et al. (2009) & Naef et al. (2001) & Saffe et al. (2005), 17: Nespral et al. (2017), 18: Petigura et al. (2016), 19: Petigura et al. (2016), 20: Eylen et al. (2016), 21: Holman et al. (2010), 22: Holman et al. (2010), 23: Doyle et al. (2011), 24: Sanchis-Ojeda et al. (2012), 25: Sanchis-Ojeda et al. (2012), 26: Welsh et al. (2012), 27: Welsh et al. (2012), 28: Johnson et al. (2012), 29: Bonomo et al. (2015), 30: Masuda et al. (2013) & Hirano et al. (2012), 31: Bruno et al. (2015), 32: Xie (2014), 33: Kostov et al. (2014), 34: Dawson et al. (2014) & Mancini et al. (2016), 35: Santerne et al. (2014), 36: Ortiz et al. (2015), 37: Mancini et al. (2016), 38: Kostov et al. (2016), 39: Queloz et al. (2010), 40: Hellier et al. (2010), 41: Hébrard et al. (2013), 42: Anderson et al. (2014), 43: Triaud et al. (2015), 44: Anderson et al. (2014), 45: Hellier et al. (2017), 46: Hellier et al. (2017), 47: Hellier et al. (2017)

Determining the age of a planet is necessary to use evolution models to constrain its metal content; unfortunately, this is often a difficult value to obtain. Our ages come from stellar ages listed in the literature, typically derived from a mixture of gyrochronology and stellar evolution models. These methods can produce values with sizable uncertainties, typically given as plausible value ranges. We treat these as flat probability distributions (a conservative choice), and convert values given as Gaussian distributions to 95% confidence intervals.

Because planets do most of their cooling, and therefore contraction, early in their lives (see Fortney et al., 2007, for a discussion), large uncertainties in age are not a major obstacle in modeling older planets. For planets which may be younger than a few Gyr, we cannot rule out that they are very metal-rich, but young and puffy, as the two effects would cancel out. We account for this in our analysis; planets which may be young consequently exhibit higher upper bound uncertainties in heavy element mass. For Kepler-16 (AB)-b, Kepler-413 (AB)-b, and WASP-80 b, no age was given, so we used a range of .5-10 Gyr. This is reasonable because it represents the possibilities of the planets being either young or old, and because the age was a second-order effect on our heavy element assessment (after mass and radius)as seen in Figure 2.3.

2.3 Models

We created one-dimensional planetary models consisting of an inert core composed of a 50/50 rock-ice mixture, a homogenous convective envelope made of a H/He-rock-ice mixture, and a radiative atmosphere as the upper boundary condition. The models are made to satisfy the equations of hydrostatic equilibrium, mass conservation, and the conservation of energy.

$$\frac{\partial P}{\partial m} = -\frac{Gm}{4\pi r^4} \tag{2.1}$$

$$\frac{\partial r}{\partial m} = \frac{1}{4\pi r^2 \rho} \tag{2.2}$$

$$\frac{\partial L}{\partial m} = -T\frac{\partial S}{\partial t} \tag{2.3}$$

Equation 2.3 is not used in the core, where luminosity is neglected. Structures are initially guessed, then iteratively improved until these conditions are met to within sufficiently small error. This computation was done in a new Python code created for this study. Its advantages are its relative speed (a 6 million planet grid takes < 1 hour to create) and its ability to easily try different compositional structures (e.g. heavy elements in the core vs. envelope) and/or equations of state. As a simple visual diagnostic, Figure 2.3 shows the output of our models.

For our atmosphere models, we interpolate on the solar metallicity grids from Fortney et al. (2007), as was done in several other works (including Miller et al. (2009) and Lopez & Fortney (2014). With these models we compute the intrinsic luminosity (L) of a planet model (see equation 2.3), which describes the rate that energy escapes from the interior, at a given surface gravity and isentropic interior profile. These grids are then used to determine the rate of entropy change in the envelope, and the contraction history of a given model planet. The initial entropy is not important; reasonable initial values typically all converge within a few hundred million years (Marley et al., 2007). As such we do not need to consider if planets form in a hot or cold start scenario. Following Miller et al. (2009), we include the small extension in radius due to the finite thickness of the radiative atmosphere.

A fully self-consistent treatment of the atmosphere would use a range of metal-

enriched atmosphere grids to be interpolated to yield consistency between atmospheric metallicity and H/He envelope metal mass fraction. Metal-enriched grids would tend to slow cooling and contraction (Burrows et al., 2007) and yield *larger* heavy element masses than we present here. However, given uncertainties in the upper boundary condition in strongly irradiated giant planets (see, e.g., Guillot (2010) for an analytic analysis,Spiegel & Burrows (2013) for a review of the chemical and physical processes at play, and Guillot & Showman (2002) for an application of a 2D boundary condition), and our uncertainty in where the heavy elements are within the planets (core vs. envelope) it is not clear if such an expanded study is yet warranted.

In creating our models, we had several important factors to consider: where the heavy elements are within the planet, what the composition of these heavy elements is, and how to treat the thermal properties of the core. These questions do not have any clearly superior or well-established solutions. The uncertainties from them, however, were overshadowed by the large uncertainties from available values for mass, radius and (to a lesser extent) age. Therefore, in designing our models, we chose plausible solutions instead of attempting to incorporate all modeling uncertainties into our results.

2.3.1 Heavy Element Distribution

Hydrogen-Helium mixtures are more compressible than typical heavy elements, and so models with heavy elements in a core tend to be larger than models with the same heavy element mass mixed throughout the envelope (see Baraffe et al., 2008, for a discussion). Conversely, modeling planets with pure heavy element cores and pure H/He envelopes requires the most heavy elements of any structure for a given total mass and radius. For some planets in our sample we find this

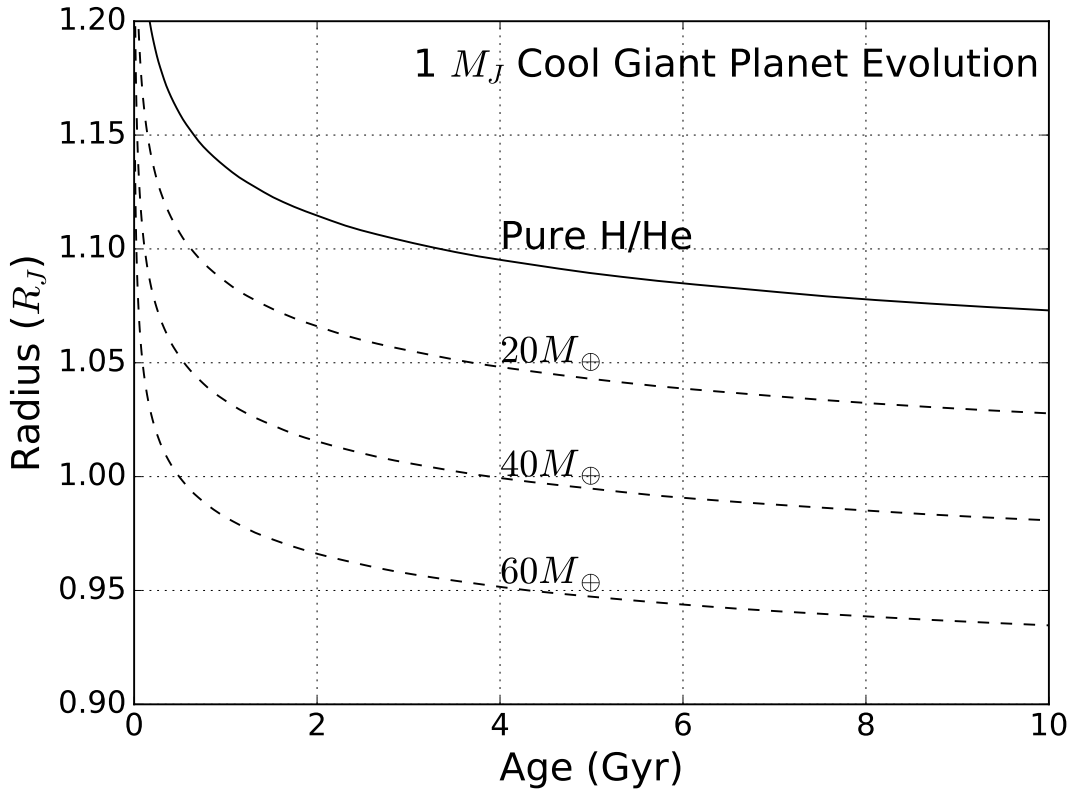

Figure 2.3: The radius evolution over time of 1 M_J planets with low stellar insolation (1×10^7 erg s^{-1} cm^{-2}) containing various quantities of metal. The plot demonstrates that our models have reasonable behavior, shrinking with age and heavy-element enrichment. The amount of metal present has an effect on the radius substantial enough to be observed in exoplanet populations.

kind of model requires implausibly high metal-enrichment to explain a given radius (cores of several *Jupiter masses* for extreme cases), and it is difficult to imagine how such massive cores could form. As such, in our models here we distribute the heavy element mass by putting up to 10 $M_\oplus$ into a pure heavy element core, and then use linear mixing to put any remaining metal mass in the otherwise H/He envelope. This allows us to consistently model both core-dominated low-mass planets and likely better-mixed massive planets.

For our work, we are assuming a homogeneous, isentropic envelope. In our

solar system, however, at least some inhomogeneities must exist (Chabrier et al., 1992), such as helium phase separation in Saturn. Layered semi-convective models are also consistent with structure models (e.g. Leconte & Chabrier, 2012), though more work is needed to understand the origin and maintenance of such layers. At a given metal mass, such structures suppress planetary heat loss, resulting in larger radii at a given age. Therefore, our model would underestimate the heavy-element masses of such planets. Such a model implies that cooler giants could be "anomalously" inflated if they have the right compositional structure Chabrier & Baraffe (2007), but no such planets have been observed. We conclude that our homogeneous model is an acceptable approximation, but look forward to future work in understanding how composition interacts with thermal evolution.

2.3.2 Equations of State

For hydrogen and helium we used the Saumon et al. (1995) equation of state (EOS), with a solar ratio of hydrogen to helium ($Y = 0.27$). For envelopes with metals mixed in, we used additive volumes to adjust the equation of state. Our choice for the metal EOS was also important – denser materials like iron produce noticeably smaller planets (and therefore require a smaller $Z_{\rm planet}$ to explain a given planet). Olivine, a mineral whose EOS is commonly used to represent rock, is less dense than iron. Water, used as a proxy for ices generally, is less dense still. MF2011 showed that changing the metal composition produces differences on the order of 20%, consistent with our models. We chose to use a 50-50 rock-ice mixture, using the Thompson (1990) ANEOS equation of state. This would overestimate $Z_{\rm planet}$ if the metal were actually iron-dominated, but this seems unlikely to occur commonly in giant planets, which are typically expected to form near the snow line (Ida & Lin, 2004).

2.4 Analysis

To apply our models to an observed planet, we take draws from the probability distributions implied by the measurement uncertainties in mass, radius, age. Each draw therefore consists of a mass, radius and age for one planet. The probability distributions are normal, except for the age, which is conservatively modeled as a flat range (see §2.2). For each draw we compute the inferred heavy-element mass. By making many (10,000) draws we have an estimate of the range of heavy-element masses consistent with observations. This procedure is done for each planet in the sample.

The resulting distributions were single peaked and roughly Gaussian overall (see Figure 2.4). For some of our planets, the uncertainty was dominated by the mass or radius, as evidenced by a correlation among the draws for each individual planet. Mass error more commonly dominated the uncertainty at high $Z_{\rm planet}$, and radius error at low $Z_{\rm planet}$. Our reported values show the marginal mean of each distribution, with upper and lower uncertainties computed as the RMS deviation from the mean from draws above the mean and below the mean, respectively. These represent the data reasonably well, but care should be taken not to overlook the correlation with input variables. For our part, we do all computation directly on the samples (see below), and report the uncertainties in the resulting distributions.

Some planets whose $Z_{\rm planet}$ values were clustered near zero (pure H/He) or one (pure ice/rock) generated draws which could not be recreated in our models. This occurred if (for example) the draw was randomly assigned a low value for mass and a high value for its radius, such that it was larger than an analogous pure H/He object. These draws were discarded, but we noted how often this occurred.

For the six planets where this occurred 15.8% - 50% of the time (where at least a 1 σ tail is outside the valid range), the error-bar on that side was adjusted to a $Z_{\rm planet}$ of exactly 0 or 1, as appropriate. These are marked with a † in Table 2.1. For the massive H/He dominated planet Kepler-75b, this occurred more than half the time, so its heavy element derived values are listed as upper limits.

To conduct the regressions described in our results (§2.5), we use a linear Bayesian regression on the log of the values of interest, using uninformative priors on the slope and intercept. The likelihood for the regression was

$$P(\vec{y}|\mathbf{X}, \tilde{\beta}, \sigma^{\mathbf{2}}) = \text{Normal}(\mathbf{X}\tilde{\beta}, \sigma^{\mathbf{2}}\mathbf{I}) \tag{2.4}$$

where $\vec{y}$ is the vector of y points, $X = [\vec{1}, \vec{x}]$ is the matrix of covariates, $\vec{\beta}$ is the coefficients vector (essentially [b,m] from $y = mx + b$), and I is the identity matrix. Using the standard noninformative prior $P(\beta, \sigma^2|\mathbf{X}) \propto \mathbf{1}/\sigma^{\mathbf{2}}$ and the distribution of $\vec{y}$ and the covariate $\vec{x}$ as $P(\vec{y}, \vec{x}) = \prod_i P_i(y_i, x_i)$ we derived the full conditional distributions and implemented a Gibbs sampler. For each fit we initialized with the classical fit, and had a burn in of 1000 steps and thinned the results by keeping only every tenth step to ensure the results were well-mixed. Our fits were performed in logspace so that they were effectively power-law fits.

We considered the possibility that mass and radii observations are not independent. If they are correlated, then sampling more directly from observational data (or posteriors thereof) could improve the uncertainties in our heavy element masses. Such an operation would need to be careful not to extract more information than the data actually provide. Southworth et al. (2007) describes a method of computing surface gravity which is more precise than directly using a planet's derived mass and radius. They instead use orbital parameters, the planet's radius, and the stellar reflex velocity K. These are closer to the observed quantities, and

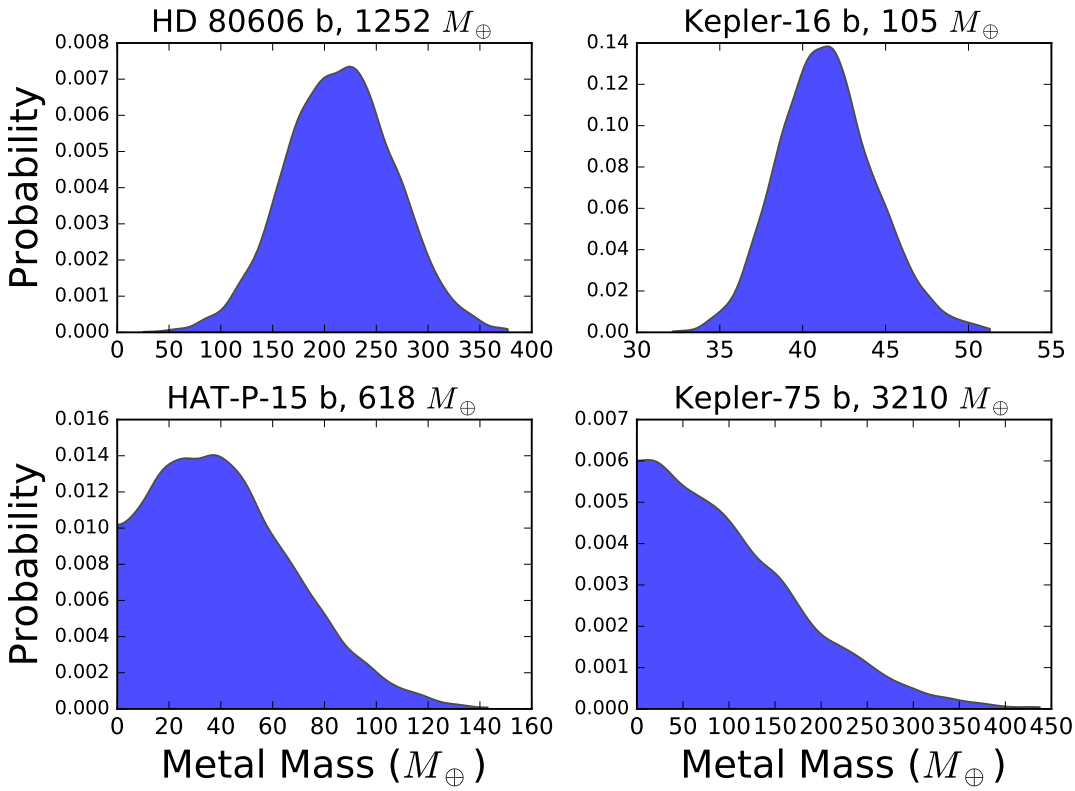

Figure 2.4: Plots of the inferred heavy element masses for four giant planets, using a Gaussian KDE of 10,000 samples each. The top two, HD 80606b and Kepler-16b, have distributions typical of the sample. HAT-P-15b is one of the six planets for which more than a 1σ portion of the distribution extends below the pure H/He limit. Each of these planets has had their lower error bars extended to zero, changes marked with a "†" on Table 1. Kepler-75b is the single planet for which only an upper limit could be determined; its RMS heavy element mass (134 $M_\oplus$) is reported as the upper error.

so avoid unnecessarily compounding uncertainties. We used Southworth's formula as a proxy to estimate how much improvement in uncertainty we might see from such an approach. We found that most of our planets exhibited only modestly better gravity estimates (though a handful were substantially improved, such as HAT-P-18 b). As such, we determined that trying to work more directly from observation data would not be worthwhile for our set of planets. Still, we suggest that studies examining individual planets should consider this approach.

2.4.1 Modeling Uncertainty

In the preceding sections, we listed a number of possible sources of modeling uncertainty. We will now argue that these uncertainties, while present, do not significantly affect our results, especially the fits described in §2.5. To the extent that they are affected, the error should be concentrated in the coefficient of our fits (not the power) because to first order these uncertainties would affect all planets equally.

First, we consider the effect of the heavy-element distribution on the structure and evolution of the planets. Considering the two extreme cases, where the metal is either entirely confined to a core or entirely dissolved into a homogeneous envelope, we compared the resulting models of four representative giant planets against our preferred models. As can be seen in Figure 2.5, these different choices have a clear effect on the inferred metal abundance, but the effect is small compared to observational uncertainties.

To evaluate the effect of EOS uncertainty, we considered the difference between the Saumon-Chabrier H/He EOS that we used and the Militzer & Hubbard (2013) EOS. This EOS is computed from DFT-MD simulations which may be more accurate than the semi-analytic SCvH EOS. We were unable to use it for this work

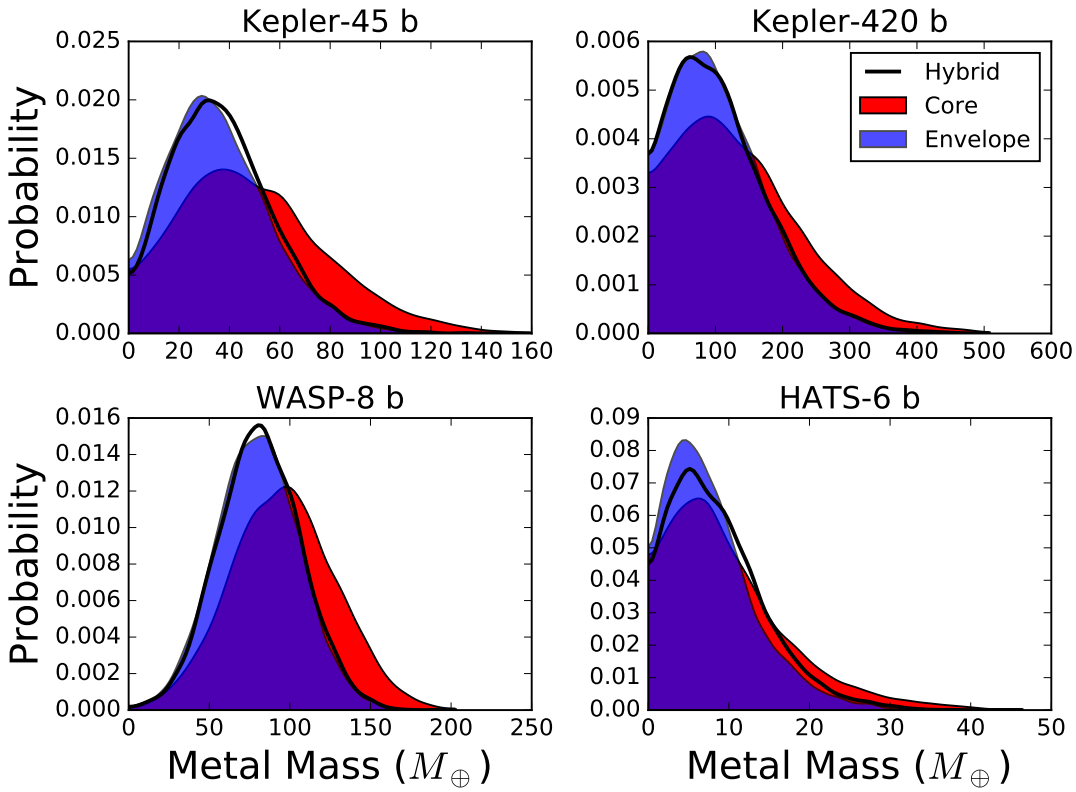

Figure 2.5: A comparison of three Z distribution models of inferred heavy-element abundance for four of our sample planets using a Gaussian KDE. Blue represents a fully homogenous envelope with no core, red is a model with all heavy-elements located in a central core, and the black line is our intermediate model. The spread comes from observational uncertainties on the mass, radius, and age of the planet (see §2.4). Although the model can have a significant effect on the inferred metal abundance, this effect is much smaller than observational uncertainties.

because it only covers densities up to those found in roughly Jupiter-mass planets. Figure 12 from Militzer & Hubbard (2013) shows that for envelope entropies typical of older planets, the deviation in the resulting radius is about 10%. To match this, we might require as much as 15% less metal. In practice the amount is somewhat lower due to next-order effects: e.g., smaller planets evolve slower (less surface area to emit from) and the metal EOS of the planets is unaffected by a H/He EOS change.

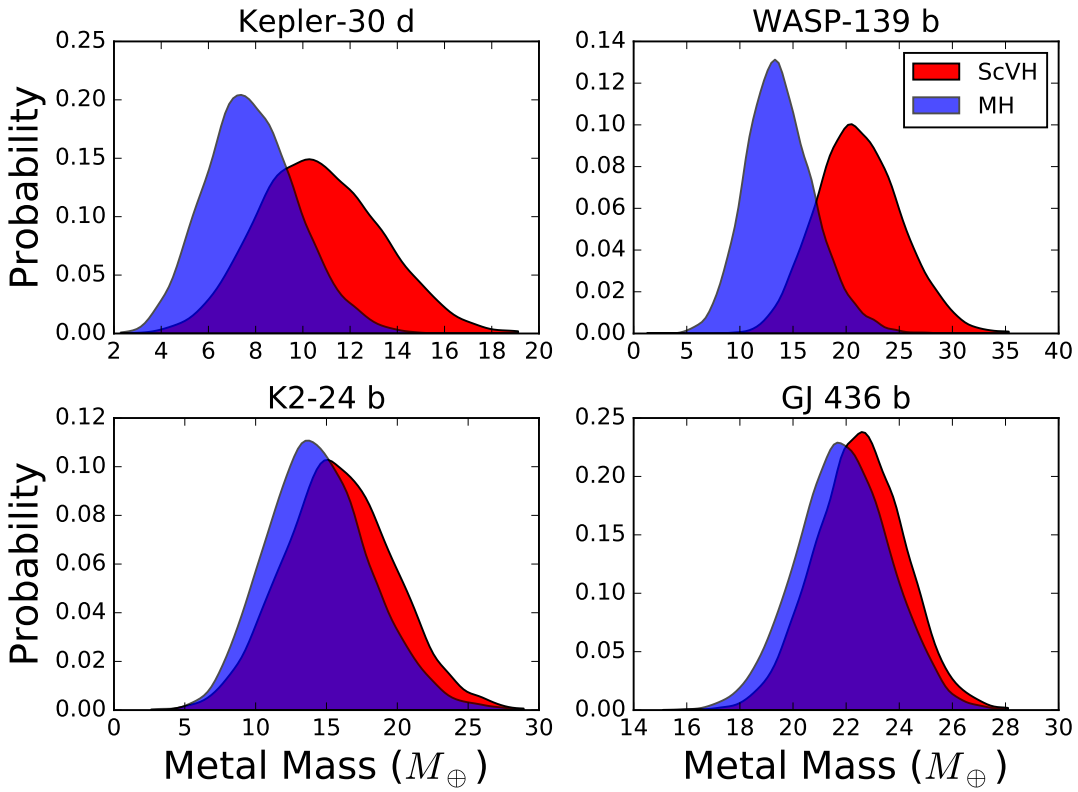

Figure 2.6: A comparison of inferred heavy-element masses for four sample planets using the ScVH and Militzer & Hubbard (2013) EOS' with a Gaussian KDE, assuming a core-only metal distribution. Most planets are only modestly impacted, but our handful of very young planets like WASP-139 b and Kepler-30 d (< 1 Gyr and < 3.8 Gyr) are affected more strongly.

To quantify this, we derived inferred metal-masses of our planets using the Militzer-Hubbard EOS where possible. The results for four planets are shown in Figure 2.6. This sample of planets is *not* representative in mass because the Militzer-Hubbard EOS does not extend to high enough pressures to model super-Jupiters. Most of the results were fairly similar (bottom row), but a few, generally young planets, exhibited more significant differences. The choice of EOS matters, but is usually a next-order effect after observational uncertainties.

As a reference, we applied our model to Jupiter and Saturn. Since these planets

Source	Jupiter	Saturn
Guillot (1999)	10-40	20-30
This Work	37	27
±10% M,R	±20	±5.5
±2 Gigayears	±1.1	±.8

Table 2.2: Inferred total heavy-element mass for Jupiter and Saturn, from Guillot (1999) and this work. For reference, we also show the uncertainties which would result if we had 10% uncertainties in mass and radius, and separately for a 2 Gyr uncertainty in age. Note that the central values lie within the estimate from Guillot.

have well-determined properties that include some gravitational moments, we can use them as a test of our model's validity. Our inferred heavy-element mass should resemble estimates from better-constrained models that make use of these gravitational moments (e.g. Guillot (1999)) but the same H/He equation of state. A state-of-the-art model for Jupiter in Hubbard & Militzer (2016) favors metal masses around 22 $M_{\oplus}$(but note that it uses a different EOS).

As we see from Table 2.2, our inferred metal masses fall within a plausible range for Jupiter and Saturn. Furthermore, we show the errors resulting from uncertainties in mass and radius (10% each) to demonstrate that these are the dominant sources of uncertainty in our study. Also, we see that the error from age uncertainty for these somewhat old planets is not very significant.

2.5 Results

We examined our results for connections between three quantities connected through the core-accretion model: the planetary mass M, its heavy element mass M_z, and the stellar metallicity [Fe/H]. We also considered the metal mass fraction of the planet $Z_{\rm planet}$ and its ratio to that of the parent star $Z_{\rm planet}/Z_{\rm star}$.

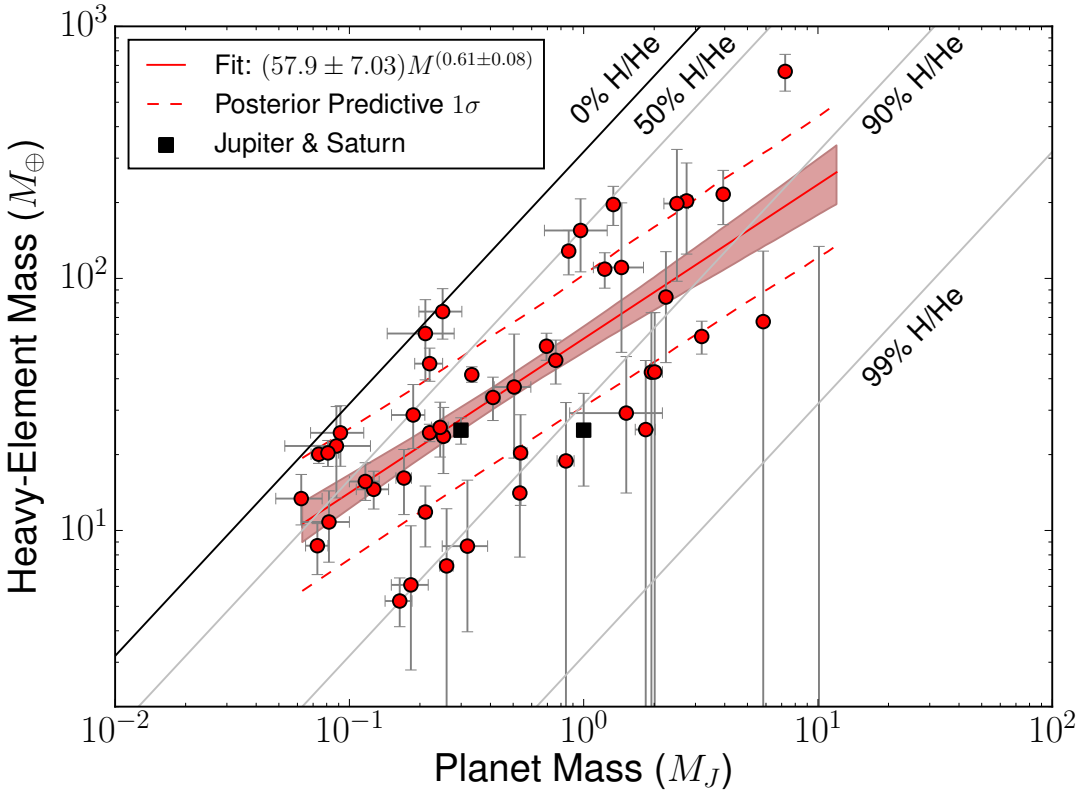

Figure 2.7: The heavy element masses of planets and their masses. The lines of constant $Z_{\rm planet}$ are shown at values of 1 (black), 0.5, 0.1, and .01 (Gray). Distributions for points near $Z_{\rm planet} = 1$ tend to be strongly correlated (have well-defined $Z_{\rm planet}$ values) but may have high mass uncertainties. No models have a $Z_{\rm planet}$ larger than one. The distribution of fits (see §2.4 for discussion) is shown by a red median line with 1 σ shaded region. The dotted line is the 1 σ predictive region. Note Kepler-75b at 10.1 $M_{\rm J}$ which only has an upper limit.

2.5.1 Relation to Planet Mass

There exists a clear correlation between planet mass and heavy element content. We can see that as we move towards more massive planets, the total mass of heavy elements increases, but the bulk metallicity decreases (Figure 2.7). Using Kendall's Tau with the mean values of metal mass and total planet mass, we measure a correlation of .4787 and a p-value of 2.07×10^{-6}, strongly supporting

a correlation. This is consistent with a formation model where an initial heavy element core accretes predominantly, but not exclusively, H/He gas (e.g. Pollack et al. (1996)). Indeed, it appears likely that all of our sample planets have more than a few $M_\oplus$ of heavy-elements and usually far more (though we cannot determine a minimum exactly), consistent with both MF2011 and theoretical core-formation models (Klahr & Bodenheimer, 2006). A fit to the log of the data gives $M_z = (57.9 \pm 7.03)M^{(.61\pm.08)}$, or roughly $M_z \propto \sqrt{M}$ and $Z_{\rm planet} \propto 1/\sqrt{M}$. Our parameter uncertainties exclude a flat line by a wide margin, but the distribution has a fair amount of spread around our fit. The intrinsic spread was the factor $10^\sigma = 1.82 \pm .09$ (because σ was calculated on the log of the variables), which means that 1σ of the data is within a factor of 1.82 of the mean line. While some of this may be from observational uncertainty, it seems likely that other effects, such as the planet's migration history and the stochastic nature of planet formation, also play a role. With this in mind, using planet mass alone to estimate the total heavy element mass appears accurate to a factor of a few.

2.5.2 Effect of Stellar Metallicity

The metallicity of a star directly impacts the metal content of its protoplanetary disk, increasing the speed and magnitude of heavy element accretion. We examined our data for evidence of this connection. MF2011 observed a correlation for high metallicity parent stars between [Fe/H] and the heavy element masses of their planets (see also Guillot et al. (2006) and Burrows et al. (2007) for similar results from inflated planets). If we constrain ourselves to the fourteen planets in MF2011, we see the same result. However, the relation becomes somewhat murky for our full set of planets (see Figure 2.8). Applying Kendall's Tau to the most likely values of metal mass and [Fe/H], we measure a correlation of .08845 and a

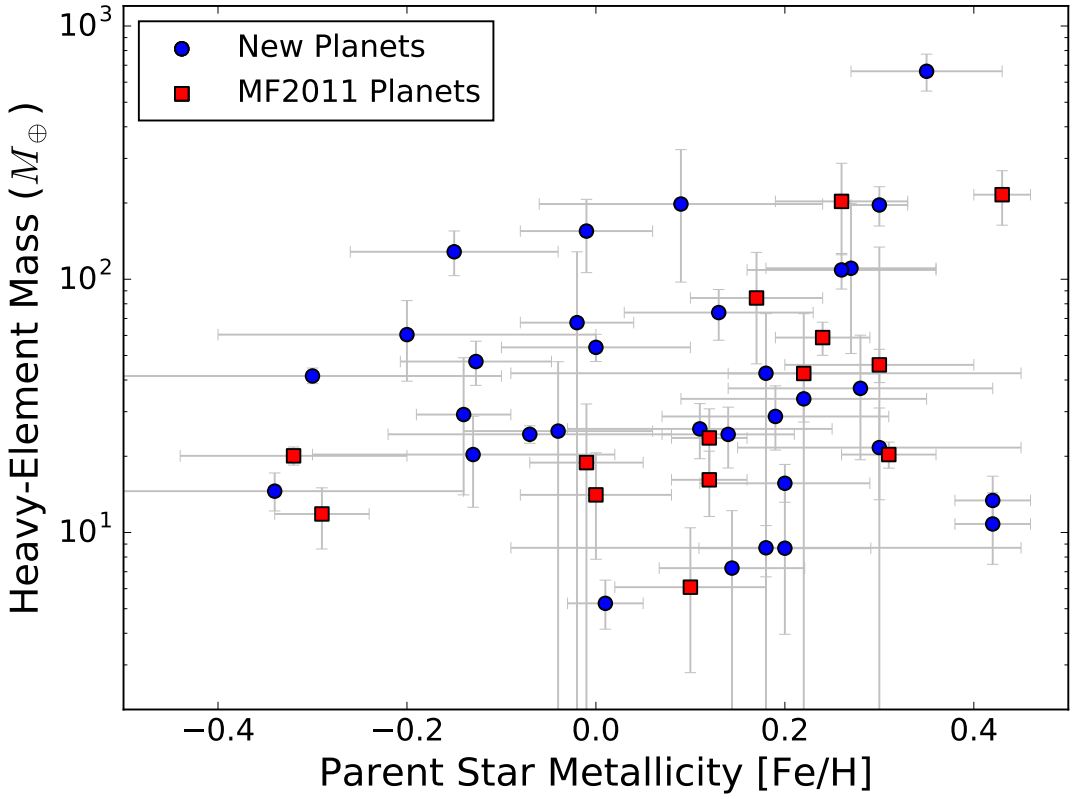

Figure 2.8: The heavy element masses of planets plotted against their parent star's metallicity. Our results for the planets studied in MF2011 are in blue, and the remaining planets in our data set are in red. A correlation appears for [Fe/H] in the blue points, but washes out with the new data. Still, it appears that planets with high heavy element masses occur less frequently around low iron-metallicity stars.

p-value of .3805, which indicates no correlation. Some of the reason for this may lie with the high observational uncertainty in our values for stellar metallicity, but it is still difficult to believe that there is a direct power-law relationship.

Transit surveys should not be biased in stellar metallicity, so we can instead consider how the distribution of planet mass and metallicity vary as a function of stellar metallicity. Most of the planets with heavy element masses above 100 $M_\oplus$ orbit metal-rich stars; there is no clear pattern for planets with lower metal masses. Considering the connection between planet mass and heavy element mass,

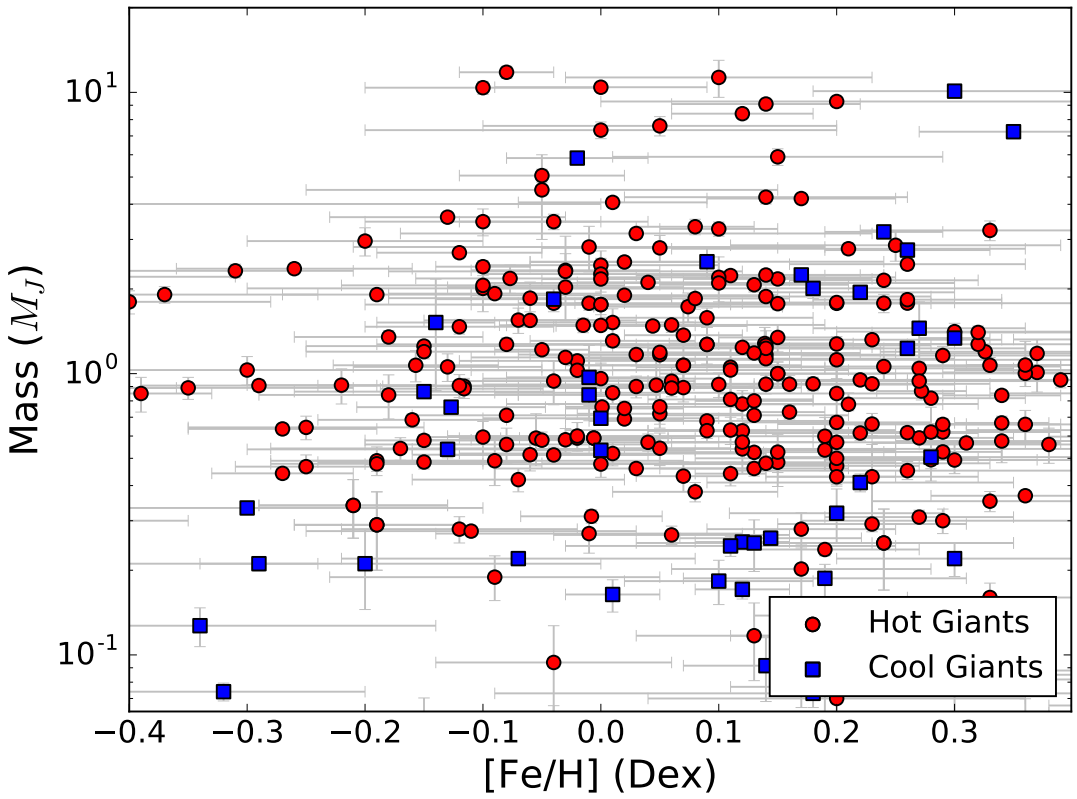

Figure 2.9: Planet mass plotted against parent star metallicity for transiting planets with RV masses. Planets in our sample are in blue. Planets in red were too strongly insolated to pass the flux cut (the inflated hot Jupiters). Note the lack of planets around low-metallicity stars above about 1 M_J. This, combined with the findings on Figure 2.8, suggests that planets around low-metallicity stars are unable to generate the giant planets which typically have massive quantities of heavy elements.

we note that planets more massive than 2-3 Jupiters are found far less often around low-metallicity stars (see Figure 2.9). Presumably, these trends are connected. This is similar to one of the findings of Fischer & Valenti (2005) in which the number of giant planets and the total detected planetary mass are correlated with stellar metallicity. The population synthesis models in Mordasini et al. (2012) also observe and discuss an absence of very massive planets around metal-poor stars. In the future, a more thorough look at this connection should take into account

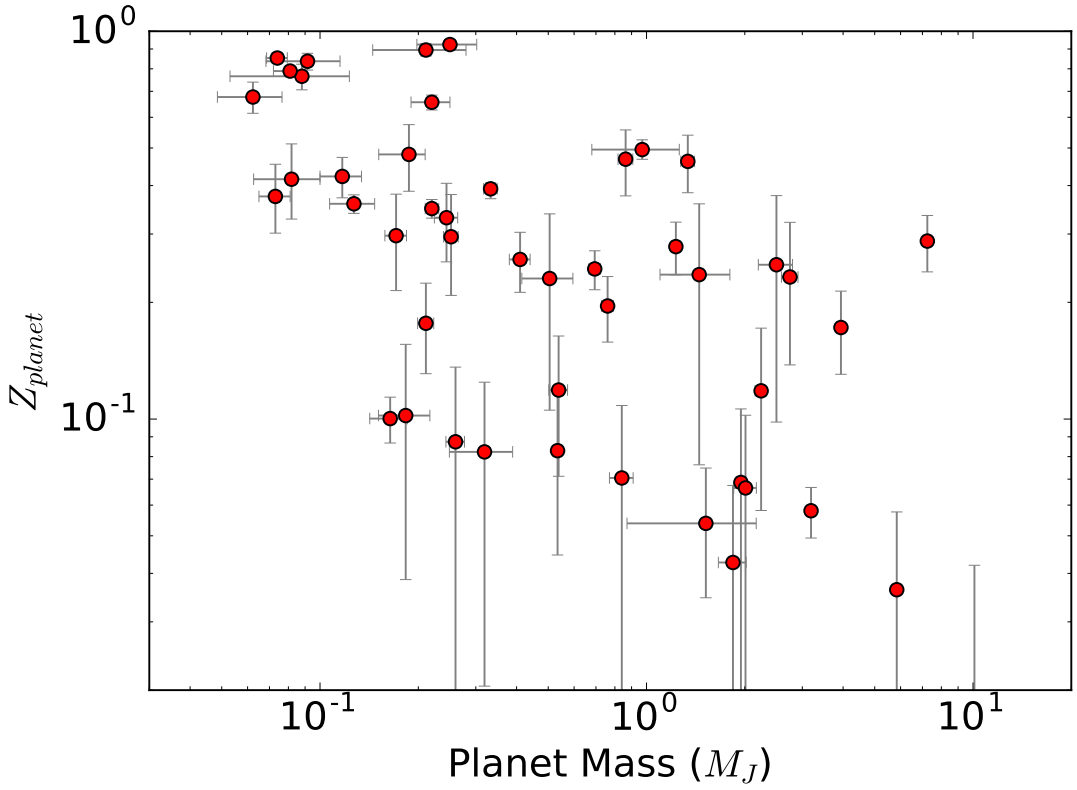

Figure 2.10: The heavy element fraction of planets as a function of mass. We observe a downward trend with a fair amount of spread. Compare especially with Figure 2.11, which shows the same value relative to the parent star.

stellar metal abundances other than iron and put an emphasis on handling the high uncertainties in measurements of stellar metallicity.

2.5.3 Metal Enrichment

A negative correlation between a planet's metal enrichment relative to its parent star was suggested in MF2011 and found in subsequent population synthesis models (Mordasini et al., 2014), so we revisited the pattern with our larger sample. We see a good relation in our data as well (Figure 2.11), and using Kendall's tau as before, we find a correlation of .4398 with a p-value of 1.3×10^{-5}. The

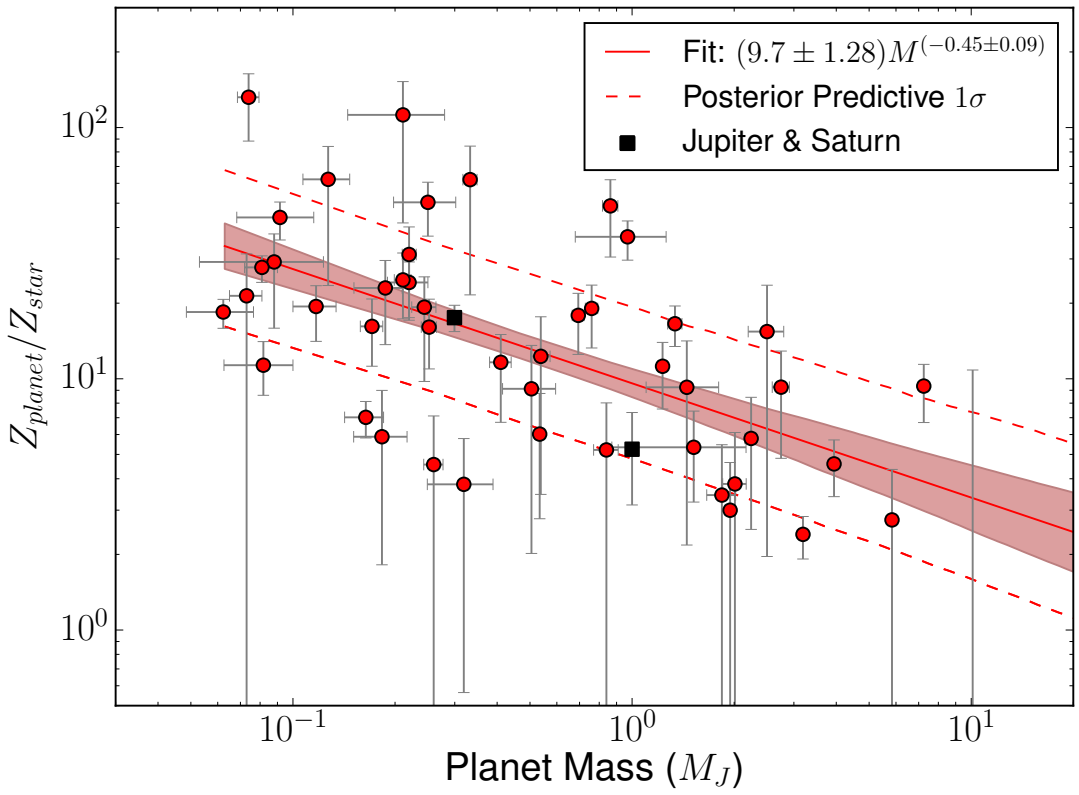

Figure 2.11: The heavy element enrichment of planets relative to their parent stars as a function of mass. The line is our median fit to the distribution from bootstrapping, with 1, 2, and 3 σ error contours. Jupiter and Saturn are shown in blue, from Guillot (1999). The pattern appears to be stronger than considering $Z_{\rm planet}$ alone against mass.

exponent for the fit shown in Fig. 2.11 ($-.45 \pm .09$) differs somewhat from the planet formation models of Mordasini et al. (2014) (between -0.68 and -0.88). The pattern appears to be stronger than if we considered only the planetary metal fraction $Z_{\rm planet}$ alone (shown in Figure 2.10). This supports the notion that stellar metallicity still has some connection to planetary metallicity, even though we do not observe a power-law type of relation. Jupiter and Saturn, shown in blue, fit nicely in the distribution. Our results show that even fairly massive planets are enriched relative to their parent stars. This is intriguing, because it suggests

that (since their cores are probably not especially massive) the envelopes of these planets are strongly metal-enriched, a result which can be further tested through spectroscopy. Note that we calculate our values of $Z_{\rm star}$ by assuming that stellar metal scales with the measured iron metallicity [Fe/H], using the simple approximation $Z_{star} = .014 \times 10^{[Fe/H]}$ (given our [Fe/H] uncertainties, a more advanced treatment would not be worthwhile). Considering other measurements of stellar metals in the future would be illuminating. For instance, since oxygen in a dominant component of both water and rock, perhaps there exists a tighter correspondence between $Z_{\rm planet}$ and the abundance of stellar oxygen, rather than with stellar iron. We also considered the possibility that orbital properties might relate to the metal content, perhaps as a proxy for the migration history. We plot the residual from our mass vs. $Z_{\rm planet}/Z_{\rm star}$ fit against the semi-major axis, period, eccentricity, and parent star mass in Figure 2.12. No pattern is evident for any of these. Given the number of planets and the size of our error-bars in our sample, we cannot rule out that any such patterns exist, but we do not observe them here. We also considered the residual against the stellar flux. Any giant planets with radius inflation which had made it into our sample would appear as strong outliers below the fit, since we would have mistaken inflation for lower heavy element masses. Therefore, the lack of a pattern here suggests our flux cut is eliminating the inflated hot Jupiters as intended.

2.5.4 Heavy Element Masses in Massive Planets

The extreme values for some of the heavy element masses are noteworthy. HAT-P-20 b, the upper-right point in Figure 2.7, contains over 600 $M_\oplus$ of metal. It is a 7.2 M_J planet orbiting a metal-rich star ([Fe/H] = $.35 \pm 0.08$), so we expect it would be metal-rich. Still, it is surprising that a planetary nebula can have so

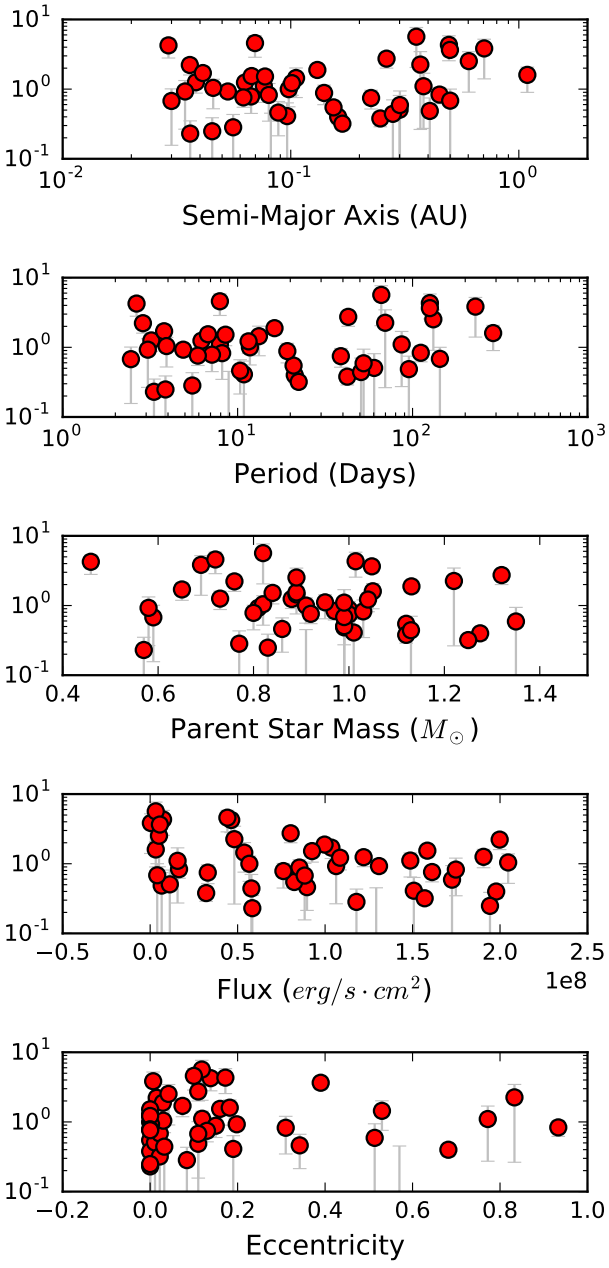

Figure 2.12: The relative residuals (calculated/fit) to the fit of $Z_{\rm planet}/Z_{\rm star}$ against mass, (Fig. 2.11) plotted against the semi-major axis, period, parent star mass, flux, and eccentricity. No relation is apparent. The lack of a residual against flux implies that we have successfully cut out the inflated hot Jupiters; had we not, the high flux planets would be strong lower outliers.

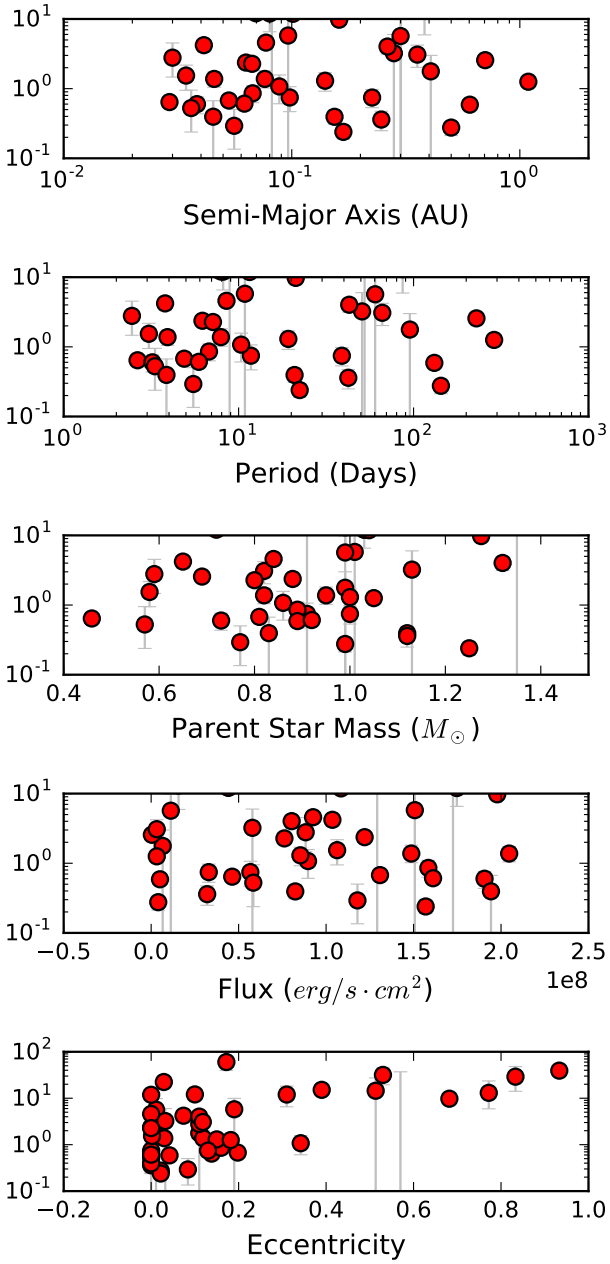

Figure 2.13: Same as Figure 2.12, but for the fit on heavy-element mass against total mass seen in figure 2.7. The spread is somewhat higher in this case, but it exhibits a similar lack of correlation with flux.

much metal to put into just one planet. This is not a high estimate; our choice of a 10 $M_\oplus$ core yields a value lower than if more of the metal were located in a core (see §2.3.1). A core-dominated equivalent could have as much as 1000 $M_\oplus$ of metal. As such, it is much more plausible that the planet is envelope-dominated. The extreme metal content of HAT-P-20 b has been observed before (Leconte et al., 2011) and is not unique (e.g. Cabrera et al. (2010)). Such planets raise questions about how such extreme objects can form (see also Leconte et al. (2009) for a similar discussion for other massive giant planets). These planets would presumably have had to migrate through their system in such a way as to accumulate nearly all of the metal available in the disk.

However, in contrast with HAT-P-20b is Kepler-75b, at 10.1 M_J, our most massive planet in the sample. Its metal-enrichment is significantly smaller than HAT-P-20b. One could entertain the suggestion that HAT-P-20b formed via core-accretion, but that Kepler-75b is a low-mass brown dwarf that formed through a different mechanism. At any rate, the future of determining whether a given object is a planet or low mass brown dwarf via characteristics like composition, rather than mass, which we advocate (and see also Chabrier et al., 2014) is promising.

2.6 Interpretation

One might expect that core accretion produces giant planets with total metal masses of approximately $M_z = M_\mathrm{core} + Z_* M_\mathrm{env}$, where the core mass $M_\mathrm{core} \sim 10 M_\oplus$ depends on atmospheric opacity but is not known to depend strongly on final planet mass, a large fraction of disk solids are assumed to remain entrained with the envelope of mass M_env as it is accreted by the core, and the mass fraction of the disk in metals is assumed to match that of the star, Z_*. Such a model would predict that a planet of total mass $M_p = M_\mathrm{core} + M_\mathrm{env}$ has a metallicity $Z_{pl} \equiv$

M_z/M_p that is related to that of the star by $Z_{pl}/Z_* = 1 + (M_{\rm core}/M_p)(1 - Z_*)/Z_*$. This expression falls off substantially more rapidly with planet mass than the $Z_{pl}/Z_* \approx 10(M_p/M_J)^{-0.5}$ fit in Figure 2.11.

This lack of good agreement is not surprising given that the above model does not predict the high metallicities of solar system giants. These have long been interpreted as coming from late-stage accretion of additional planetesimal debris (e.g. Mousis et al. (2009)). In keeping with this solar system intuition, we instead propose that the metallicity of a giant planet is determined by the isolation zone from which the planet can accrete solid material. We assume that a majority of solids—which we treat interchangeably with metals in this initial investigation—eventually decouple from the disk gas and can then be accreted from the full gravitational zone of influence of the planet. An object of mass M, accreting disk material with surface density Σ_a at distance r from a star of mass M_*, can accumulate a mass

$$M_a = 2\pi r(2 f_H R_H)\Sigma_a = 4\pi f_H \left(\frac{M}{3M_*}\right)^{1/3} \Sigma_a r^2 \tag{2.5}$$

where $f_H \sim 3.5$ is the approximate number of Hill radii $R_H = r(M/3M_*)^{1/3}$ from which accretion is possible as long as the orbital eccentricity of accreted material is initially less than $(M/3M_*)^{1/3}$ (Lissauer, 1993). Thus, under our assumption that solids have decoupled from the gas, a planet of mass M_p can accrete a total solid mass of

$$M_z \approx 4\pi f_H f_e Z_* \left(\frac{M_p}{3M_*}\right)^{1/3} \Sigma r^2 \ , \tag{2.6}$$

where Σ is the total surface density of the disk and $f_e Z_* \Sigma$ is the surface density in solids. The parameter f_e allows for an enhancement in the metal mass fraction of the disk compared to the solar value, Z_*, for example due to radial drift of solid

planetesimals through the gas nebula. No enhancement corresponds to $f_e = 1$. We note that Equation 2.6 applies independent of the solid mass fraction of the planet because M_p is taken to be the final observed planet mass, including any accreted solids.

For comparison, the standard isolation mass of a planet forming in a disk with total surface density Σ is

$$M_{iso} = \left[4\pi f_H (3M_*)^{-1/3} \Sigma r^2\right]^{3/2} \tag{2.7}$$

which may be calculated using Equation 2.5 with $M_a = M = M_{iso}$ and $\Sigma_a = \Sigma$. Recalling that $Z_{pl} = M_z/M_p$, Equations 2.6 and 2.7 combine to yield

$$\frac{Z_{pl}}{Z_*} = f_e \left(\frac{M_p}{M_{iso}}\right)^{-2/3} \tag{2.8}$$

For $f_e = 1$, when $M_p = M_{iso}$, the total mass of the planet equals the total disk mass in its isolation region and $Z_{pl}/Z_* = 1$, as, for example, would happen if an isolation-mass planet formed by accumulating all material within its isolation zone. For $M_p < M_{iso}$, the planet's metallicity exceeds the metallicity of the star because the planet has not been able to accrete all isolation-zone gas but we assume that it is able to accrete all of the region's solids.

Equation 2.8 encapsulates the physics of our model, but to compare with observed planets, we re-express this result in terms more easily related to the expected population of protoplanetary disks from which planets form—Toomre's Q parameter (Safronov, 1960; Toomre, 1964) and the disk aspect ratio H/r. In a Keplerian disk, $Q = c_s\Omega/(\pi G\Sigma) = (H/r)(\pi r^2\Sigma/M_*)^{-1}$, where c_s is the isothermal sound speed, Ω is the orbital angular velocity, $H = c_s/\Omega$ is the disk scale height,

and G is the gravitational constant. Thus,

$$\frac{Z_{pl}}{Z_*} \approx 3 f_H f_e \frac{H}{r} Q^{-1} \left(\frac{M_p}{M_*}\right)^{-2/3} \tag{2.9}$$

Figure 2.14 replots the values and best fit line of Figure 2.11, overlaying Z_{pl}/Z_* calculated using Equation 2.9 with $f_e = 1$ for each planet's M_p and M_*. We use a fiducial value of $H/r = 0.04$ (corresponding to e.g., 2 AU at 200 K) and plot curves for $Q = 1$, 5, and 20. The $Q = 5$ curve provides a good match for the best fit line, while $Q = 1$ and $Q = 20$ bound the remaining data points. We omit data points corresponding to planet masses in excess of the total local disk mass, $M_p > \pi r^2 \Sigma = (H/r) Q^{-1} M_*$, which removes the portion of the $Q = 20$ curve corresponding to the highest planet masses. For $f_e > 1$, the values of Q plotted in Figure 2.14 should be multiplied by f_e. For modest enhancements in the solid to gas ratio in the disk, limits on the total disk mass could preclude formation of the most massive planets in the sample in the highest Q disks, potentially explaining the lack of points in the bottom-right portion of the plot. Values of $Q < 1$ imply gravitational instability and cannot be maintained for extended periods in a disk, so the fact that our modeled Z_{pl}/Z_* does not require $Q < 1$ for any value of f_e is encouraging. For reference, at Jupiter's location $r = 5$AU in the minimum mass solar nebula $\Sigma = 2 \times 10^3$g cm^{-2} $(a/\mathrm{AU})^{-3/2}$ (Hayashi, 1981), $Q \approx 25$.

Why might a planet remain smaller than its isolation mass? For our model, the reason is irrelevant. The planet could have accreted its envelope at a different location in the disk at an earlier time when solids were unable to decouple from the gas. It could even be a remnant fragment formed by gravitational instability. Whatever its formation process, our model only asserts that it accretes most of its metals at some point concurrent with or after it has accumulated most of the gas it will accrete from the nebula. Hence, its metallicity is determined by the mass

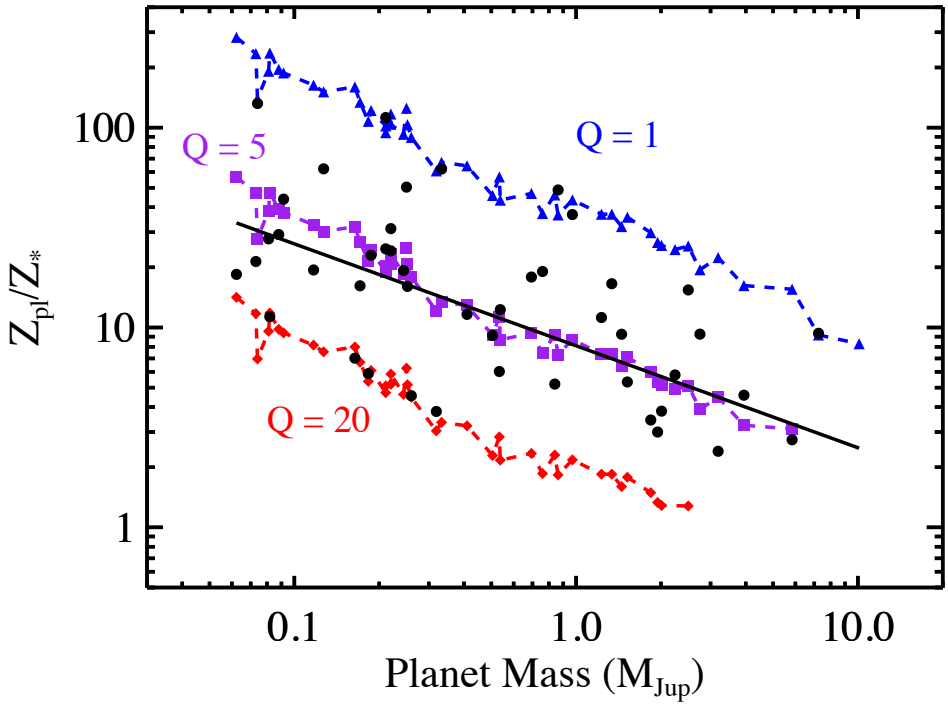

Figure 2.14: Metallicity ratio calculated using Equation 2.9 with $f_e = 1$ using M_p and M_* for each of the planets in Figure Y. We set $H/r = 0.04$ and plot curves for $Q = 1$ (blue triangles), 5 (purple squares), and 20 (red diamonds). The best fit line (in Figure 2.11, solid black) for the data (black circles) is displayed for reference.

in solids contained within its gravitational feeding zone. However, for a plausible scenario, we may again appeal to studies of Jupiter formation, which suggest that the planet's final mass is determined by the mass at which the planet truncates gas accretion by opening a large gap in the disk (e.g. Lissauer et al. (2009)).

Gap opening and the planetary starvation that results remains a topic of continuing research (e.g. Crida et al. (2006),Fung et al. (2014),Duffell & Dong (2015)). Here we simply note that the planet masses observed in our sample are consistent with a classic theory of gap starvation. Tidal torques opposed by viscous accretion

yield a gap width

$$\Delta = \left(\frac{f_g}{\pi \alpha} \frac{M_p}{M_*} \frac{r^2}{H^2} \right)^{1/3} R_H \quad , \tag{2.10}$$

where $f_g \approx 0.23$ is a geometric factor (Lin & Papaloizou, 1993). Assuming that gas accretion through the gap becomes inefficient for $\Delta / R_H = f_S \sim 5$ (Lissauer et al., 2009; Kratter et al., 2010), a planet mass M_p set by gap truncation implies the disk viscosity parameter (Shakura & Sunyaev (1973), Armitage (2011))

$$\alpha = \frac{f_g}{\pi f_S^3} \frac{M_p}{M_*} \left(\frac{H}{r} \right)^{-2} \quad . \tag{2.11}$$

These values—displayed in Figure 2.15 for the same planets plotted in Figure 2.14—span a reasonable theoretical range for protoplanetary disks, particularly in dead zones, where most giant planets are thought to form (e.g. Turner et al. (2014), Bai (2016)).

We note that Equations 2.9 and 2.11 do not depend directly on the planet's distance from its star, r. Instead, they are functions of H/r, which depends weakly on r for typical disks, and of Q, which may be thought of as a parametrization of the disk mass. Hence, our model applies regardless of whether the observed planets have migrated from their formation locations. For relatively low-mass disks, such migration is in fact required. For the minimum mass solar nebula used above, for example, $M_{iso} = 0.6 M_J (r/\mathrm{AU})^{3/4}$. Giant planets separated by less than 1AU from their host stars most likely did migrate from more distant formation locations (e.g. Dawson & Murray-Clay, 2013).

2.7 Discussion and Conclusions

There is a strong connection between planet mass and metal content. From a sample of 47 transiting gas giants, we find that the heavy-element mass increases

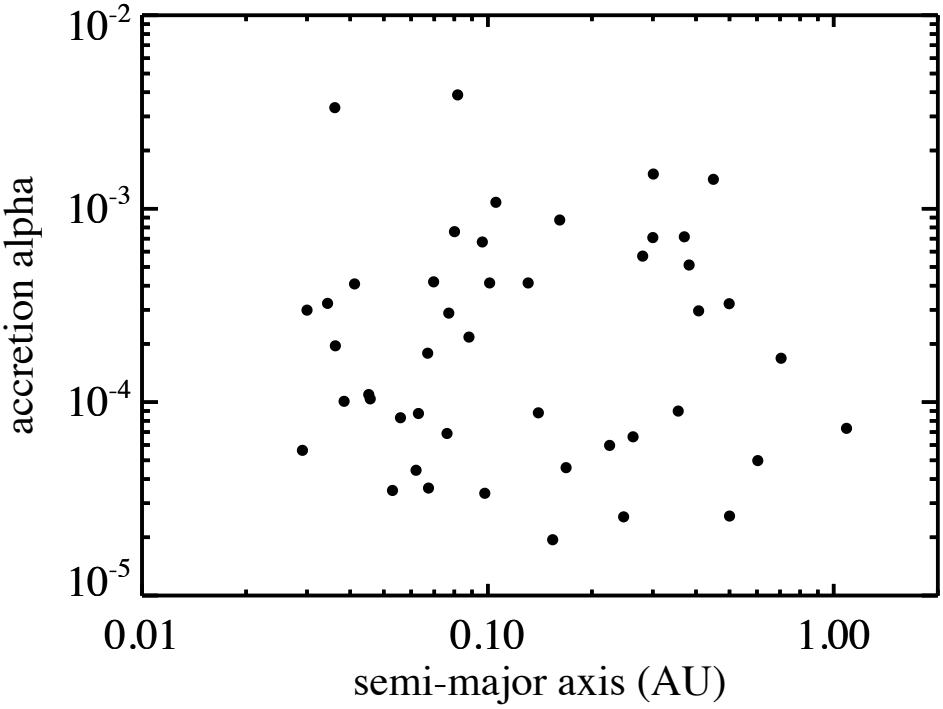

Figure 2.15: Implied values of the disk viscosity parameter α, calculated using Equation 2.11, for the scenario that the total planet masses observed in our sample are limited to less than the isolation mass at their formation locations due to gap starvation. These values span a reasonable theoretical range for protoplanetary disks.

as $\sqrt{M}$, so $Z_{\rm planet}$ decreases as $1/\sqrt{M}$. We also see that our planets are consistently enriched relative to their parent stars, and that they likely all have more than a few $M_\oplus$ of heavy-elements. These results all support the core-accretion model of planet formation and the previous results from MF2011 that metal-enrichment is a defining characteristic of giant planets. We have also shown that our results for $Z_{\rm planet}/Z_{\rm star}$are comfortably consistent with a simple planet formation model using plausible values for disk parameters. Our results were not consistent with a more naive model of formation in which a fixed-mass core of heavy-elements directly accretes parent-star composition nebular material.

This work suggests that spectroscopy of the atmospheres of gas giants should also yield metal-enrichments compared to parent star abundances (Fortney et al., 2008), as is seen in the solar system. We suggest that this growing group of < 1000 K planets should be a sample of great interest for atmospheric observations with the *James Webb Space Telescope*. Since the bulk metallicity of the cool planets can be determined, atmospheric studies to determine metal-enrichments can be validated. For most of our planets more massive than Saturn, the heavy elements values are high enough that most metals are in the envelope, rather than the core (See Figure 2.7), so our $Z_{\rm planet}$ values are upper limits on $Z_{\rm atmosphere}$. Atmospheric observations to retrieve the mixing ratios of abundant molecules like H_2O, CO, CO_2, and CH_4 could show if most heavy elements are found within giant planet envelopes or within cores. In comparison, for hot Jupiters > 1000 K we cannot estimate with confidence the planetary bulk metal enrichment since the radius inflation power is unknown.

Some connection between planetary heavy element mass and stellar metallicity is suggested by our work, but the correlation is not strong. A fruitful area of future investigation will be in analyzing stellar abundances other than iron. Learning which stellar metals most strongly correlate with planetary bulk metallicity (for instance, Fe, Mg, Si, Ni, O, C) would hint at the composition of planetary heavy elements and could provide insights into the planet formation process. With the continued success of ground-based transit surveys, along with K2 (Howell et al., 2014), and the 2017 launch of *TESS*, we expect to see many more "cooler" gas giant planets amenable to this type of analysis, which will continue to provide an excellent opportunity for further exploring these relations. With this continuing work on bulk metal-enrichment of planets, and the spectroscopy of planetary atmospheres, the move towards understanding planet formation in the mass /

semi-major axes / composition planes should be extremely fruitful.

3. Hot Jupiter Radius Inflation

3.1 Introduction

The longest standing open question in exoplanetary physics is what causes the inflated radii of "hot Jupiters", gas giant planets on short period orbits heated to equilibrium temperatures $T_{\rm eq} > 1000$ K (Miller & Fortney, 2011). Since the first detection of planet HD 209458b (Charbonneau et al., 2000; Henry et al., 2000), the radii of the vast majority of these transiting gas giants have exceeded the expected radius of $\sim$1.1 times that of Jupiter, sometimes approaching 2 Jupiter radii. This excess radius appears to correlate with the level of incident stellar irradiation (Guillot & Showman, 2002; Laughlin et al., 2011), rather than e.g. semi-major axis (Weiss et al., 2013). A wide range of theories have been proposed to explain this, most of which postulate an additional "anomalous" power which heats the convective interior of the planet, leading to larger radii. Typically, these theories are tested by directly modeling the physics to determine if they can produce large enough radii to explain the observations (e.g. Tremblin et al. (2017); Ginzburg & Sari (2016)). We shall take the a more complete approach by determining what anomalous powers are needed to explain the radii of the whole observed population, and then considering what models are most consistent with this.

This approach is feasible thanks to the work of surveys such as WASP, HAT, and Kepler, which have identified a large number of transiting giant planets. Follow-up radial-velocity measurements have yielded mass measurements for many of these. Merging data from the NASA Explanet Archive (Akeson et al., 2013) and exoplanet.eu (Schneider et al., 2011), we examine the set of transiting planets with measured masses and radii with relative uncertainties of less than 50%, in the mass range 20 $M_\oplus < M <$ 13 M_J. The resulting flux-radius-mass data is shown in Figure 3.1. Several patterns are apparent. First, many planets with high incident flux are anomalously large – these are the hot Jupiters. The flux at which this the excess radii become apparent has been estimated to occur at 0.2 Gerg s^{-1} cm^{-2}(Miller & Fortney, 2011), equivalent to an equilibrium temperature $T_{eq} \approx 1000$ K. Second, the degree of radius inflation increases steadily with flux. Finally, the degree of radius inflation is greater at lower masses. This is more visible in Figure 3.2, which plots radius against planetary mass.

In modeling the interior structure of a transiting giant planet with a measured mass, there are two key variables which are not directly observable: the bulk heavy-element abundance and the anomalous power. Planets at fluxes below the inflation threshold, including Jupiter and Saturn, are well described by evolution models with zero anomalous power. In this cool giant regime, we can directly infer the heavy-element mass from the observables. Our previous work, Thorngren et al. (2016), did this for the ∼50 known cool transiting giant planets (those with $T_{eq} < 1000$ K), and observed a correlation between the planetary heavy-element mass and the total planet mass of $(M_z/M_\oplus) \approx 58(M/M_J)^{.61}$. That cool giant sample and this hot giant sample do not differ much in semi-major axis (typically $\sim$ .1 vs. $\sim$ .03 AU), so we do not expect that their formation mechanisms or composition trends to differ. Thus for this work, we apply this relation with its

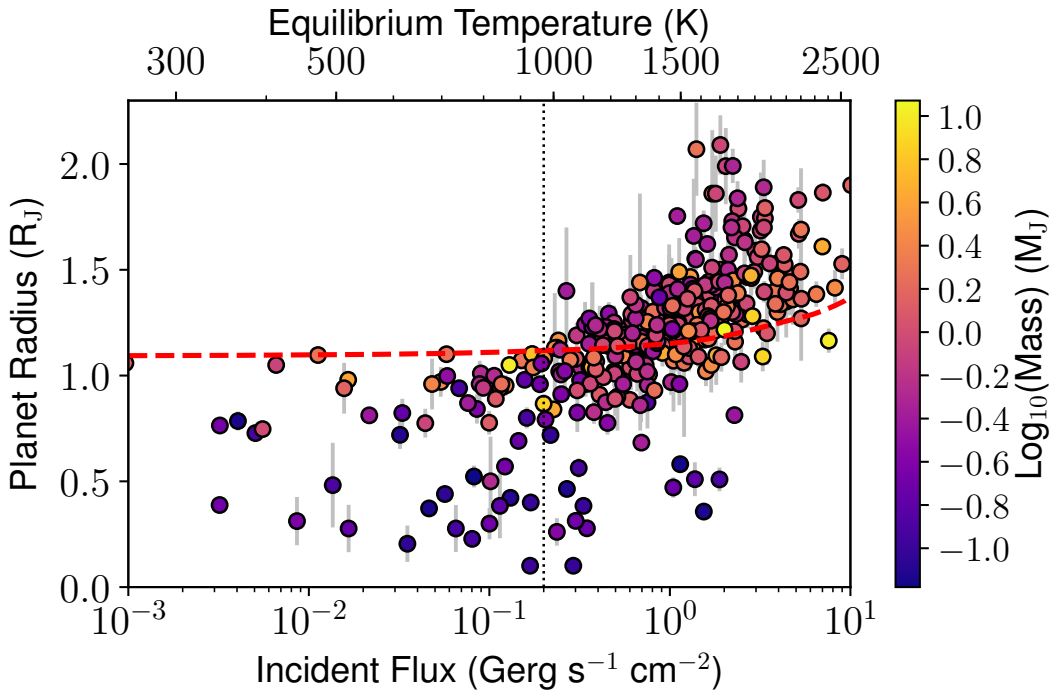

Figure 3.1: The radii of transiting giant exoplanets plotted against their incident flux (or equilibrium temperature) and colored by mass on the log scale. The dotted red line is the radius of a Jupiter-mass pure H/He model with no inflation effect, an approximate upper limit on the non-inflated case. The dotted vertical line is the empirical flux cutoff for inflation (Miller & Fortney, 2011; Demory & Seager, 2011). Beyond this level planets are anomalously large, with the excess radius correlated with flux. Less massive planets exhibit the strongest effect.

predictive uncertainty as a population-level prior on the heavy-element masses of the hot Jupiters. By doing this, we constrain one of the two unobserved variables, allowing us to infer planetary anomalous power. Individually, planets may vary in composition so by themselves our predictions are not particularly precise. However, since planets as a population will follow the trend line, a hierarchical Bayesian model based on this prior allows us to combine information from our whole sample to infer the shape of the anomalous power as a function of the flux $\epsilon(F)$. The use of the flux as a predictor was suggested by Guillot & Showman (2002) and Weiss et al. (2013), among others.

A key advantage of this approach is that it is robust against certain sources of modeling error. In Thorngren et al. (2016), we discussed the modest systematic uncertainties inherited from the equations of state and the distribution of metals within the planet (e.g. core vs mixed into the envelope). These issues, as well as statistical uncertainty regarding the mass-metallicity trend and our use of fixed-metallicity atmospheres, could lead to an error in the radius of the model planets. Two factors would act to ameliorate these effects. First, the effects of radius suppression from metallicity would act on planets regardless of temperature, and so the first order errors in deriving the mass-metallicity trend and the impact of metals on hot giant radii would cancel out. Second, because our sample contains a broad cross-section of different masses and fluxes for $M > 0.5 M_J$, biases which relate to the planet mass such as atmospheric metallicity are evenly applied to all flux levels. Thus, this type of error may impact the overall magnitude of $\epsilon(F)$, but will have much less effect on the shape of the function. These features do not eliminate systematic error, but they do allow for more confidence in our results.

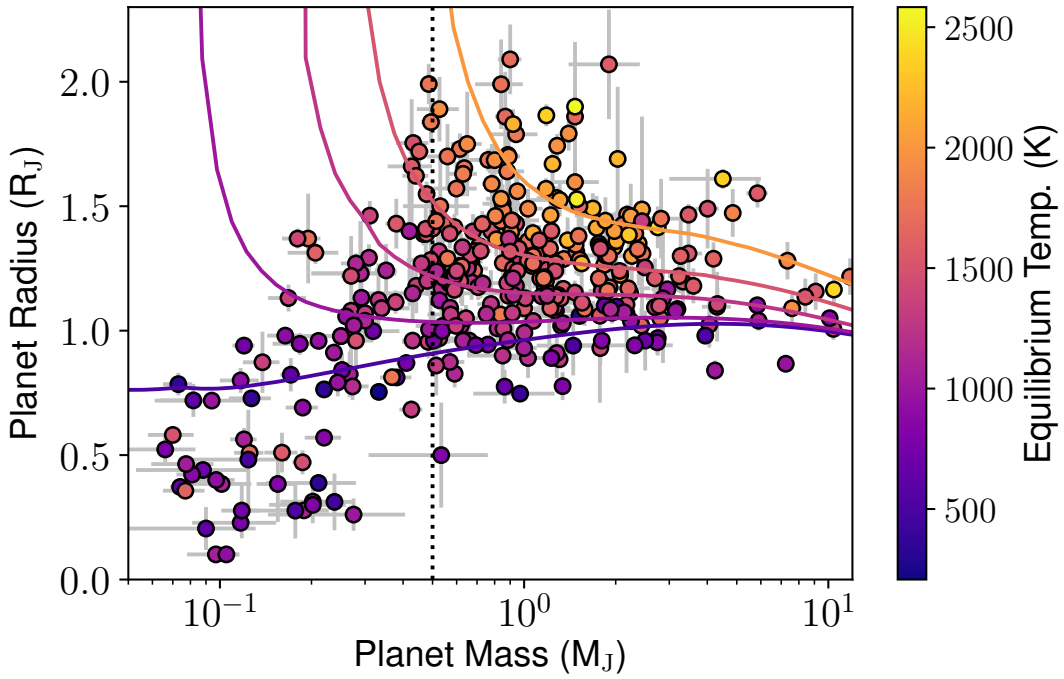

Figure 3.2: The radii of transiting giant exoplanets plotted against their masses, colored by equilibrium temperature. The solid lines are the radii of model planets of average (posterior mean) composition and inflation power using our Gaussian Process results described below for various equilibrium temperatures (500, 1000, 1250, 1500, 2000 K) on the same color scale. For each given $T_{\rm eq}$, models show the radii increasing dramatically at lower masses, coinciding with the absence of planets in that region. This upturn is a feature of any plausible model of anomalous power. Since it seems plausible that a mass-loss process affects this low-mass population, we restrict our study to planets with $M > 0.5 M_J$

3.2 Lack of Inflated Sub-Saturns

An interesting feature is apparent in the mass radius relationship. Figure 3.2 shows the masses and radii of our sample of planets, along with prediction lines of constant temperature and inflation power. The relationship between the temperature (color) and inflation power is posterior to our model (discussed later), but the general shape of the lines themselves is generic, and appears for any mass-independent model of inflation power. It is apparent that with decreasing mass and constant inflation power, the radius anomaly becomes larger exponentially. This is not seen in the observed planet radii. In fact, giant planets are not observed with surface gravity less than about 3 m/s^2, even though our models allow it and the transits of such large planets would be readily detectable. This might be the result of an inflation mechanism which is inefficient at low masses, but this possibility is weakened by examining the frequency of planets in mass-flux space (see Fig. 3.3).

Consider the population of high-mass Jupiters compared to lower-mass Saturns, separating the groups at $0.5M_J$. Among Jupiters, many high-flux planets are observed: 58% (164/281) have more than 1 Gerg s^{-1} cm^{-2}. Among Saturns, we find only 22% (21/97) which experience this level of insolation. This discrepancy does not appear to result from any observational biases. It is possible that significant mass loss could occur if planets inflate too much. Because radii increase with decreasing mass, any mass loss that occurs might experience positive feedback. This is similar to what was seen in Baraffe et al. (2004), though their mass loss rate appears to have been too high (Hubbard et al., 2007). The best alternative hypothesis appears to be that Saturns preferentially stop migration further from the parent star and that planets at these masses also experience a significantly

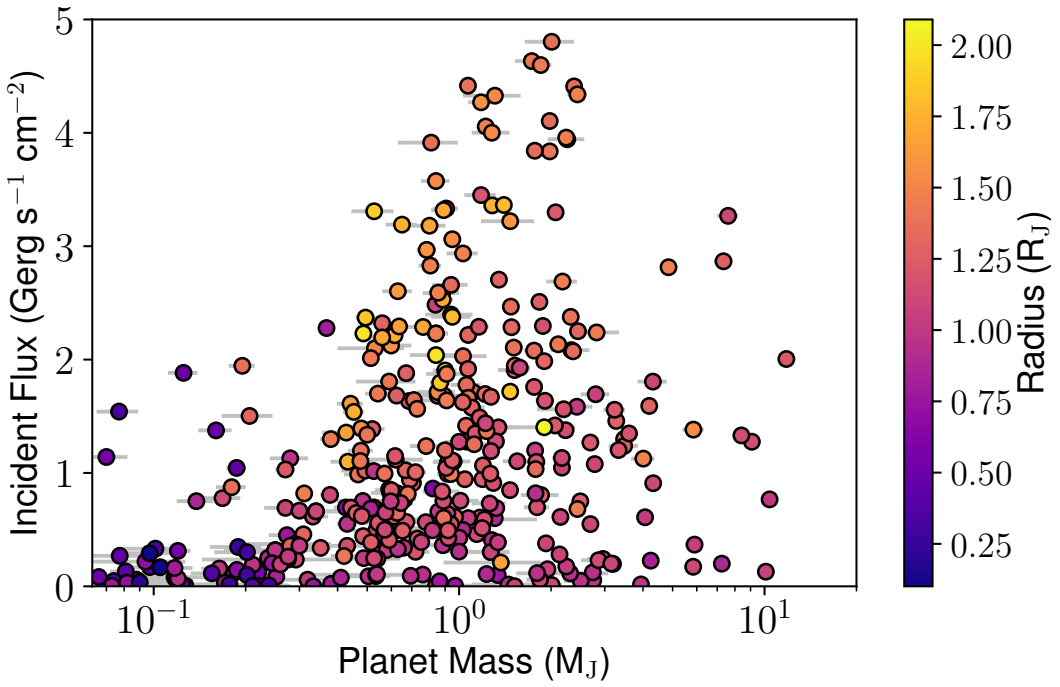

Figure 3.3: The mass vs. flux of observed transiting giant planets, colored by radius. Below about 0.4 M_J, considerably fewer high-flux planets are detected, an effect not seen in low-flux planets. Transit observational biases do not explain this. Runaway mass loss could explain both this and the lack of low-mass highly-inflated planets, though biases from formation and migration models might also exist.

less efficient inflation effect. Further study will require more advanced models, which we leave to future work. To avoid this issue, we restrict our attention to planets with $M > 0.5 M_{\rm J}$.

3.3 Planet Models

Our interior structure models are broadly the same as those in Thorngren et al. (2016), with only two changes for this work on inflated giant planets. We solve the equations of hydrostatic equilibrium, conservation of mass, and an equation of state (EOS) based on the SCvH (Saumon et al. (1995)) solar H/He EOS and the EOS of a 50/50 ice/rock mixture (Thompson, 1990).

$$\frac{\partial P}{\partial m} = -\frac{Gm}{4\pi r^4} \tag{3.1}$$

$$\frac{\partial r}{\partial m} = \frac{1}{4\pi r^2 \rho} \tag{3.2}$$

$$\rho = \rho(P, T) \tag{3.3}$$

Metals were fully mixed into the convective envelope using the additive volumes approximation. No core was included because for planets of this mass the radius difference would be minor (see Thorngren et al. (2016)). Heat flow out of the planet (and therefore thermal and structural evolution) was regulated using the atmospheric models of Fortney et al. (2007). Additional details and analysis of the effect of our modeling choices can be found in Thorngren et al. (2016). Sample evolution calculations are shown in Figure 3.4.

The most important modeling addition is the inclusion of an additional heating

power $\epsilon F \pi R^2$. The resulting power balance of the interior of the planet is

$$\frac{\partial E}{\partial t} = \pi R^2 (\epsilon F - 4F_{int}) \tag{3.4}$$

Here F_{int} is the intrinsic flux of energy radiated out of the planet as computed by the atmosphere model. Note that our definition of ϵ differs slightly from other authors, such as Komacek & Youdin (2017), who deposit the energy at a particular depth within the planet. Using their results, our definitions agree for their models where the power is deposited at the radiative-convective boundary or deeper. Otherwise, our ϵ is smaller than theirs by a factor < 1 depending on depth and stage of evolution.

The other change was an improvement to the thermal evolution integration system. The new system uses the SciPy (van der Walt et al., 2011) function Odeint to adaptively integrate the changes in planet internal entropy. We have also added a system to detect when the planet is near thermal equilibrium (when $\epsilon F \pi R^2 \approx L_{int}$), and quickly completes the evolution accordingly. This serves to handle the stiffness of the ODE near an equilibrium of high specific entropy.

3.4 Bayesian Statistical Analysis

Our statistical analysis is based on a hierarchical Bayesian approach, with two levels in the hierarchy. The lower level consists of our beliefs about the properties of individual planets given the observations and our planetary mass-metallicity relation from Thorngren et al. (2016) as a prior on bulk metallicity. The upper level combines information about the individual planets to infer population level patterns in anomalous power. The variables we will use are listed and described in Table 3.1.

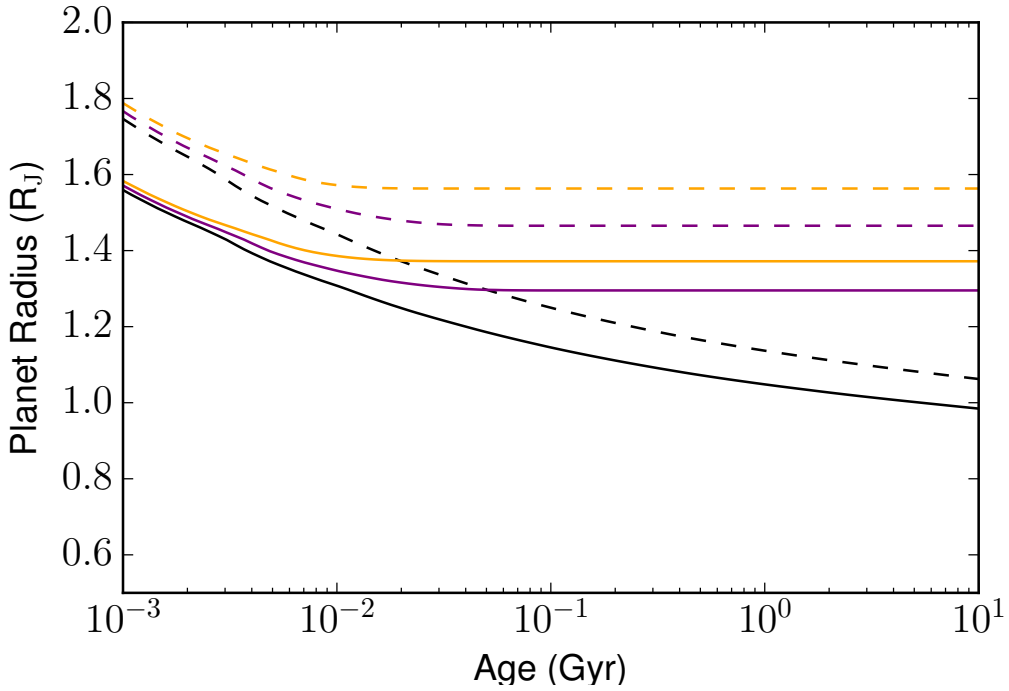

Figure 3.4: Example outputs of our evolution models for a 1 M_J planet at 2 Gerg s^{-1} cm^{-2}for different heavy-element masses and values of heating efficiency. Solid and dashed lines have 60 and 30 $M_\oplus$ of heavy elements respectively, and black, purple, and orange lines have 0, 1, and 2% heating efficiencies respectively. The plot extends to extremely young ages to illustrate the transition from rapidly cooling young planets to the nearly static older planets. Planets in our sample are generally older than a gigayear, so the effects of the heavy-element abundance and heating efficiency are not easily disentangled.

Parameters	
M_z^i, $\vec{M}_z$	The bulk heavy-element mass of the i^{th} planet, all planets.
M^i, $\vec{M}$	The true mass of the i^{th} planet, all planets.
t^i, $\vec{t}$	The true age of the i^{th} planet, all planets.
ϵ^i, $\vec{\epsilon}$	The anomalous heating efficiency (see section 3.3) of the i^{th} planet, all planets.
Hyperparameters	
$\vec{\phi}_p = [\epsilon_0, k]$	The vector of hyperparameters for the power-law model of $\epsilon(F)$.
$\vec{\phi}_l = [\epsilon_0, F_0, k]$	The vector of hyperparameters for the logistic function model of $\epsilon(F)$.
$\vec{\phi}_g = [\epsilon_0, F_0, s]$	The vector of hyperparameters for the Gaussian model of $\epsilon(F)$.
$\vec{\phi}_{gp} = [\sigma_1, l]$	The vector of hyperparameters for the Gaussian process model of $\epsilon(F)$.
Constants	
α, β, σ_z	Fitted values from the planetary mass-metallicity relationship.
R_{obs}^i, σ_r^i	The observed radius and uncertainty of the i^{th} planet.
M_{obs}^i, σ_m^i	The observed mass and uncertainty of the i^{th} planet.
t_0^i, t_1^i	The observational lower and upper limits on the age of the i^{th} planet.
F^i	The time-average incident flux onto the i^{th} planet.

Table 3.1: A list of variables used in the Bayesian model. The superscript is the index of the planet (numbered 1 to $N = 281$), whereas an arrow refers to the variable for all of the planets as a vector. E.g. the 10^{th} component of $\vec{M}_z$ is M_z^{10}. Parameters refers to model parameters of the lower hierarchical level of the model, and hyperparameters refers to those of the upper level. Constants are known, fixed values which describe the results of previous studies, and so do not need to be sampled. α, β, and σ_z are from Thorngren et al. (2016) and the remainder are from various telescope-based observational studies retrieved from on exoplanets.eu (Schneider et al., 2011) and the NASA Exoplanet archive (Akeson et al., 2013) (see Section 3.1).

3.4.1 Planetary Statistical Models

We wish to understand the observed radii of giant planets, which have normally distributed errors, in terms of our interior structure models $R(t, M_z, M, \epsilon, F)$. As such, we construct the following normal likelihood for observing the i^{th} planet's radius to be R_{obs} given the structure models parameters:

$$p\left(R^i_{obs}\middle|t^i, M^i_z, M^i, \epsilon^i\right) = \mathcal{N}\left(R^i_{obs}\middle|R(t^i, M^i_z, M^i, \epsilon^i, F^i), \sigma^i_r\right) \tag{3.5}$$

Here $\mathcal{N}$ refers to the normal distribution, and $\mathcal{N}(x|\mu, \sigma)$ is the PDF of $\mathcal{N}(\mu, \sigma)$ evaluated at x (similarly for the uniform $\mathcal{U}$ and log-normal $\mathcal{LN}$ distributions). The observed flux F^i is known to a sufficient accuracy (compared to the other observations) that we will neglect the effect its uncertainty has on the model radius uncertainty. Previous studies provide us with observational constraints on M_i and t^i, which we will use as priors. Combined with the motivated prior on M^i_z from our mass metallicity relationship, we have:

$$t^i \sim \mathcal{U}(t^i_0, t^i_1) \tag{3.6}$$

$$M^i_z \sim \mathcal{LN}\left(\alpha + \beta \log(M^i), \sigma_z\right) \tag{3.7}$$

$$M^i \sim \mathcal{N}\left(M^i_{obs}, \sigma^i_m\right) \tag{3.8}$$

$\mathcal{LN}(\mu, \sigma)$ is the base-10 log-normal distribution with location μ and scale σ (i.e. the $\log_{10}$ of the variable is distributed as $\mathcal{N}(\mu, \sigma)$). Using these priors, we can write a posterior distribution for the structure model parameters (t^i, M^i_z,M^i, ϵ^i)

as follows:

$$
\begin{aligned}
p(t^i, M_z^i, M^i, \epsilon^i | R_{obs}^i) =& p(R_{obs}^i | t^i, M_z^i, M^i, \epsilon^i) p(t^i, M_z^i, M^i, \epsilon^i) / p(R_{obs}^i) && (3.9)\\
\propto& p(R_{obs^i} | t^i, M_z^i, M^i, \epsilon^i) p(t^i) p(M_z^i | M^i) p(M^i) p(\epsilon^i) && (3.10)\\
\propto& \mathcal{N}\left(R_{obs}^i | R(t^i, M_z^i, M^i, \epsilon^i, F^i), \sigma_r^i\right) \times && (3.11)\\
& \mathcal{U}(t^i | t_0^i, t_1^i) \times \mathcal{LN}\left(M_z^i | \alpha + \beta \log(M^i), \sigma_z\right) \times \\
& \mathcal{N}\left(M^i | M_{obs}^i, \sigma_m^i\right) \times p(\epsilon)
\end{aligned}
$$

The purpose of this model is to infer ϵ^i. If we apply a simple uniform prior $\epsilon^i \sim \mathcal{U}(0, 5\%)$, we can infer the interior structure parameters for the i^{th} planet. Figure 3.5 shows the results of this approach for HD 209458 b. Unfortunately, as seen in the figure, data from a single planet does not provide enough information to infer much about ϵ^i. In the next section, we describe a hierarchical model which combines the information from many planets to draw conclusions about the anomalous power as a function of flux $\epsilon(F)$.

3.4.2 Models of Anomalous Power

For convenience, we define the function Q^i as follows:

$$
\begin{aligned}
Q^i(t^i, M_z^i, M^i, \epsilon^i) \equiv& \mathcal{N}\left(R_{obs}^i | R(t^i, M_z^i, M^i, \epsilon^i, F^i), \sigma_r^i\right) \times && (3.12)\\
& \mathcal{U}(t^i | t_0^i, t_1^i) \times \mathcal{LN}\left(M_z^i | \alpha + \beta \log(M^i), \sigma_z\right) \times \\
& \mathcal{N}\left(M^i | M_{obs}^i, \sigma_m^i\right)
\end{aligned}
$$

We include the model parameters as explicit arguments, and let the constants be indicated by the index i. This function reduces the right hand side of Eq. 3.11 to $Q^i(t^i, M_z^i, M^i, \epsilon^i) p(\epsilon^i)$. To combine information from many planets together,

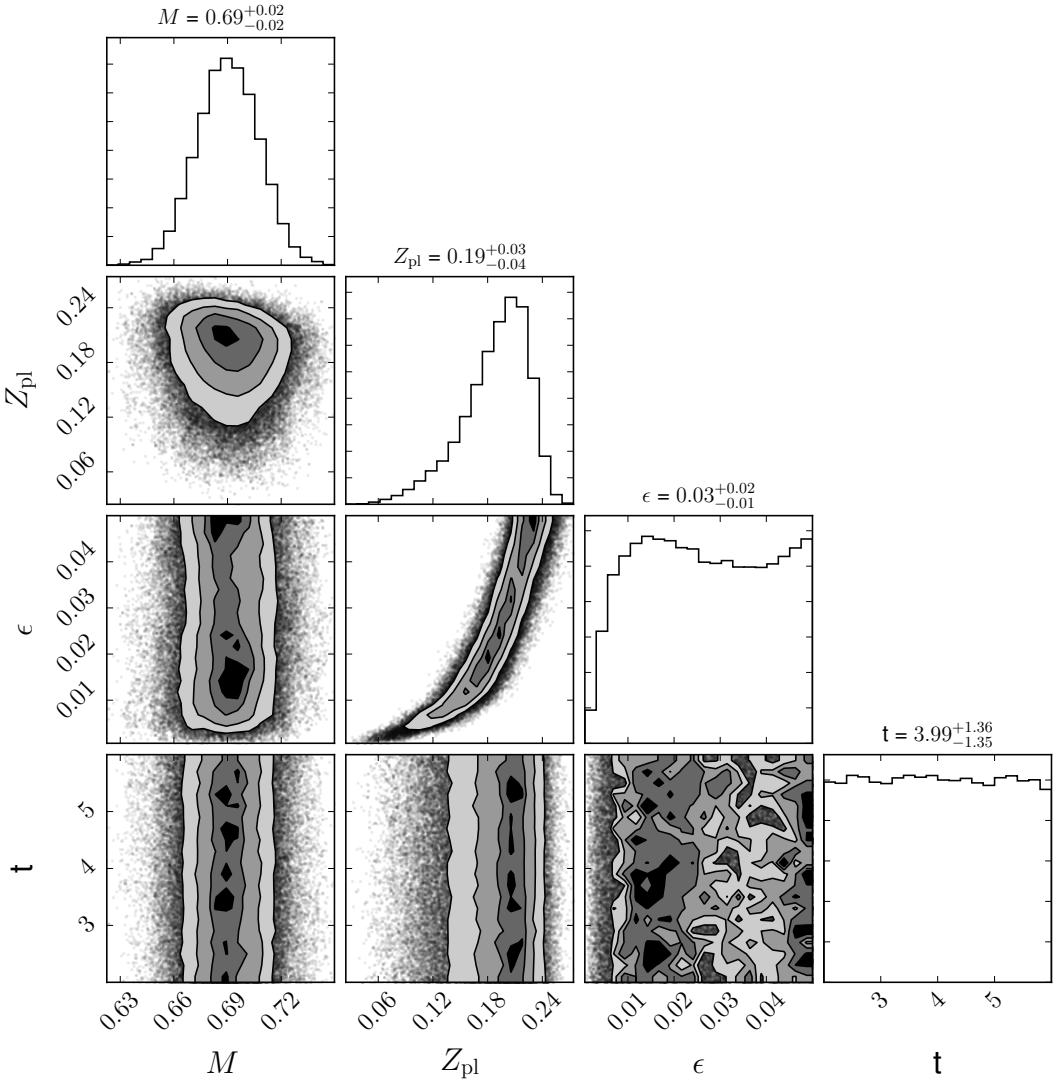

Figure 3.5: Inferred parameters for HD 209458 b, using equation 3.11. The parameters are mass in Jupiter masses, planetary metal mass fraction, inflation efficiency, and age in gigayears. The planet is old enough that its age uncertainty has little effect on the other parameters. As expected, the main driver of ϵ uncertainty is $Z_{\rm pl}$. For this planet, we disfavor an inflation efficiency below $\sim 1\%$. Together with other planets, some of which disfavor high ϵ, this forms the basis for our inference of $\epsilon(F)$.

we assume that the planet parameters t^i, M_z^i, and M^i as well as R_{obs}^i are a priori independent between planets, and thus we can simply multiply their probabilities together. For this equation we will leave the prior on ϵ^i in the general form $p(\vec{\epsilon})$.

$$p\left(\vec{t}, \vec{M}_z, \vec{M}, \vec{\epsilon} \middle| \vec{R}_{obs}\right) \propto p(\vec{\epsilon}) \prod_{i=1}^{N} Q^i(t^i, M_z^i, M^i, \epsilon^i) \tag{3.13}$$

We can now focus on constructing models of ϵ^i. First, we consider the models in which the heating efficiency ϵ is given by a deterministic function of several hyperparameters $\vec{\phi}$. We will refer to this function generally as $\epsilon(F^{(i)}, \vec{\phi})$, and consider several specific functions (power-law, logistic, and Gaussian), differentiated by their subscripts. These models were chosen because they all allow for low heating efficiencies at low fluxes, but exhibit differing behavior at high fluxes. The power-law model is a classic and simple model for many astronomical phenomena, the logistic model captures the possibility that the inflation effect "turns on" at some flux, and the Gaussian model covers the case that heating efficiency declines at high flux.

$$\epsilon_p(F, \vec{\phi}_p) = \epsilon_0 F^k \tag{3.14}$$

$$\epsilon_l(F, \vec{\phi}_l) = \frac{\epsilon_0}{1 + (F/F_0)^{-k}} \tag{3.15}$$

$$\epsilon_g(F, \vec{\phi}_g) = \epsilon_0 \exp\left(-\frac{\log_{10}(F/F_0)^2}{2s^2}\right) \tag{3.16}$$

For each of these models, we choose the follow weakly informative proper priors

for the hyperparameters:

$$p(\vec{\phi}_p) \propto \mathcal{U}(\bar{\epsilon}|0, 5\%) \times \mathcal{N}(k|0, 2) \tag{3.17}$$

$$p(\vec{\phi}_l) \propto \mathcal{U}(\epsilon_0|0, 5\%) \times \mathcal{N}(F_0|1, 2) \times \mathcal{N}(k|3, 1) \tag{3.18}$$

$$p(\vec{\phi}_g) \propto \mathcal{U}(\epsilon_0|0, 5\%) \times \mathcal{LN}(F_0|1, 2) \times \mathcal{LN}(s|0, 2) \tag{3.19}$$

In the power-law case, the uniform distribution demands ϵ_0 and k be such that that no planet's ϵ leave the $[0, 5\%]$ bounds. In the logistic case, the prior on k is fairly informative, demanding that the transition be somewhat similar to the scale of the data; this parameter would be poorly constrained otherwise. Now we substitute $\epsilon(F^i, \vec{\phi})$ into Eq. 3.13, which together with the hyperpriors gives us the following posterior:

$$p\left(\vec{t}, \vec{M}_z, \vec{M}, \vec{\phi} \middle| \vec{R}_{obs}\right) \propto p(\vec{\phi}) \prod_{i=1}^{N} Q^i(t^i, M_z^i, M^i, \epsilon(F^i, \vec{\phi})) \tag{3.20}$$

The Gaussian process (GP hereafter) model takes a slightly different form. In it, we model $\log_{10}(\epsilon)$ as a GP with mean 0 and covariance matrix K. We use the squared exponential kernel with a small white noise component $\sigma_2^2 = 10^{-3}$ for numerical convenience, which amounts to a relative spread of about 7% in linear space. Thus, the covariance matrix for the process is given by:

$$\mathbf{K}_{\mathrm{j,k}}(\vec{\phi}_{gp}) = \sigma_1^2 \exp\left(-\frac{\log_{10}(F_j/F_k)^2}{2l^2}\right) + \sigma_2^2 \delta_{j,k} \tag{3.21}$$

We define some weakly informative priors for $\vec{\phi}_{gp}$ as follows:

$$p\left(\vec{\phi}_{gp}\right) \propto \mathcal{LN}(\sigma_1^2|0, 1) \times \mathcal{LN}(l|0, 1) \tag{3.22}$$

Because we do not have simple normal distributions for them, we cannot marginalize out $\vec{\epsilon}$, and instead must keep them as parameters hierarchically connected through the GP prior. To provide an appropriate lower boundary condition on the function, we include an independent portion of the prior on ϵ^i (in combination with the GP) such that the model is:

$$p(\vec{\epsilon}_{gp}) \propto \mathcal{LN}(\vec{\epsilon}|0, \mathbf{K}(\vec{F}, \vec{\phi_{gp}})) \prod_{i=1}^{N} \mathcal{U}(\epsilon^i|0, 5\%) G^i(\epsilon^i) \tag{3.23}$$

$$G^i(\epsilon^i) \equiv \begin{cases} 1 & \text{for } F_i \geq 10^8 \\ \mathcal{LN}(\epsilon^i| -2, 1) & \text{for } F_i < 10^8 \end{cases} \tag{3.24}$$

The lognormal portion is the Gaussian Process. The G^i component is useful because it sets an appropriate lower boundary condition for $\epsilon(F)$. Experimentation reveals that this boundary condition has little effect when $F > 2$ Gerg s^{-1} cm^{-2}(the region of interest); we merely include it to best represent our belief about the function for the full range of fluxes. With these priors and likelihood, Bayes Theorem yields the posterior for the GP model:

$$p\left(\vec{t}, \vec{M}_z, \vec{M}, \vec{\epsilon}, \vec{\phi}_{GP} \middle| \vec{R}_{obs}\right) \propto p(\vec{\phi}_{gp}) \mathcal{LN}\left(\vec{\epsilon} \middle| \vec{0}, \mathbf{K}(\vec{F}, \vec{\phi_{gp}})\right) \times \prod_{i=1}^{N} Q^i(t^i, M_z^i, M^i, \epsilon^i) \mathcal{U}(\epsilon^i|0, 5\%) G^i(\epsilon^i) \tag{3.25}$$

Finally, we constructed a simple model for the thermal tides model of hot Jupiter inflation (Arras & Socrates, 2009). We adapt the scaling relations of Socrates (2013), $L \propto T_{\rm eq}^3 R^4 P^{-2}$, where L is the total anomalous power, P is the period, T_{eq} is the equilibrium temperature, and R is the planet radius. We model this as follows, where ϵ_0 is a model parameter, using the present-day radius and flux for

simplicity.

$$\epsilon_t(F) = \epsilon_0 R^2 P^{-2} F^{-.25} \tag{3.26}$$

3.4.3 Statistical Computation

We wish to use a Metropolis-Hastings MCMC (Hastings, 1970) sampler to draw samples from the posteriors given above. However, if we do this with no further simplifications, we will end up exploring the parameters very slowly. This is because the models listed above have a very large number of parameters (~ 1100) thanks to the many nuisance parameters (M_z^i, M^i, etc) which each have one parameter per planet. The complexity of our Metropolis-Hastings sampler scales with dimension at roughly $\mathcal{O}(d^2)$: $\mathcal{O}(d)$ posterior PDF evaluations (see Roberts & Rosenthal, 2004) that cost $\mathcal{O}(d)$. However, we are really only interested in $\vec{\phi}$ for the various models, plus $\vec{\epsilon}$ in the GP case. We can save a great deal of computational effort by directly sampling marginal distribution and rewriting the posteriors as follows:

$$p\left(\vec{\phi}\middle|\vec{R}_{obs}\right) = \int p\left(\vec{t}, \vec{M}_z, \vec{M}, \vec{\phi}\middle|\vec{R}_{obs}\right) d\vec{t} d\vec{M}_z d\vec{M} \tag{3.27}$$

$$= \int p(\vec{\phi}) \prod_{i=1}^{N} Q^i(t^i, M_z^i, M^i, \epsilon(F^i, \vec{\phi})) d\vec{t} d\vec{M}_z d\vec{M} \tag{3.28}$$

$$= p(\vec{\phi}) \prod_{i=1}^{N} \int Q^i(t^i, M_z^i, M^i, \epsilon(F^i, \vec{\phi})) dt^i dM_z^i dM^i \tag{3.29}$$

$$= p(\vec{\phi}) \prod_{i=1}^{N} \widetilde{Q}^i(\epsilon(F^i, \vec{\phi})) \tag{3.30}$$

We use $d\vec{t}$ and the like as shorthand for integration over every component of $\vec{t}$ in sequence over their full domain; Eq. 3.28 has 843 nested integrals! $\widetilde{Q}^i$ is defined

as Q^i integrated over t^i, M_z^i, and M^i:

$$\widetilde{Q}^i(\epsilon) \equiv \int Q^i(t^i, M_z^i, M^i, \epsilon) dt^i, dM_z^i, dM^i \tag{3.31}$$

In this way, we have rewritten the $3N$ dimensional integral in Eq. 3.28 as N separate 3 dimensional integrals in Eq. 3.29. This rewrite of the posteriors is possible because the planet parameters are only connected to each other through the hierarchical prior on ϵ. The GP posterior can be simplified in a similar fashion:

$$p\left(\vec{\epsilon}, \vec{\phi} \middle| \vec{R}_{obs}\right) \propto p(\vec{\phi}) \mathcal{LN}\left(\vec{\epsilon} \middle| \vec{0}, \mathbf{K}(\vec{F}, \vec{\phi_{gp}})\right) \prod_{i=1}^{N} \widetilde{Q}^i(\epsilon^i) \mathcal{U}(\epsilon_0 | 0, 5\%) G(F^i, \epsilon^i) \tag{3.32}$$

Using this formulation to get posterior samples relies on our ability to compute $\widetilde{Q}^i(\epsilon)$ up to a constant of proportionality. This is easier than it might appear. Eq. 3.31 is proportional to the single planet posterior PDF (Eq. 3.11) for $p(\epsilon) \propto \mathcal{U}(0, 5\%)$, marginalized over t^i, M_z^i, and M^i. We chose this prior for epsilon because we do not believe that ϵ will exceed 5%. We can estimate this marginal PDF by sampling from the posterior and applying a Gaussian kernel density estimate (KDE) with reflected boundaries (see Silverman, 1986) to the ϵ samples. Fig. 3.6 shows the results of this procedure for WASP-43 b. Doing this for each planet i gives us $\widetilde{Q}^i(\epsilon)$. These can be plugged into the marginalized models (assuming $0 < \epsilon < 5\%$), radically reducing the dimension.

As estimated above, our sampler scales with dimension at roughly $\mathcal{O}(d^2)$, so breaking it up into many sub-samplers is highly desirable. The result is a much more computationally efficient sampling system, at the cost of no longer having posterior samples of the structure parameters.

Scatterplot matrices of our upper-level model posteriors are shown in figures 3.7-3.10, and the those of the lower level model for HD 209458 b are shown in

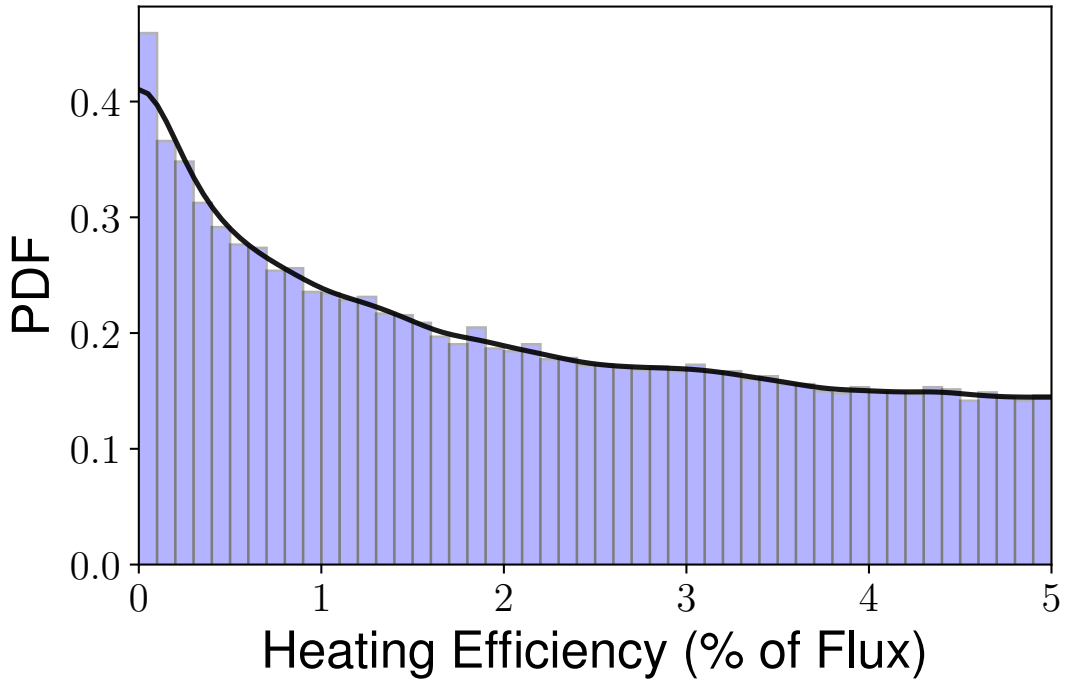

Figure 3.6: The histogram and kernel density estimate (the black line) of the posterior inflation power ϵ (proportional to $\widetilde{Q}^i(\epsilon)$) for WASP-43 b. In this case, smaller values of ϵ are more likely, but larger values are not ruled out. Note that the KDE matches the histogram, as is required for us to be able to use it as a likelihood for the upper level of the hierarchical model.

figure 3.5. The upper-level posteriors are provided in an accompanying data file. The plots were made using corner.py (Foreman-Mackey, 2016).

To compare different models, we are unable to use the more familiar model selection criteria, the BIC/AIC, as these are only defined for non-hierarchical models. This is because in the hierarchical case the number of parameters is not well-defined (Gelman et al., 2014b). Probably the most Bayesian approach is to compare the Bayes factors (also called the evidence) of the models. However Gelman et al. (2014a) (Chapter 7.4) advise against their use in the case of continuous variables with uninformative priors as we have here. Furthermore, computing Bayes factors here would he computationally expensive. Instead, we make use of the Deviance Information Criterion (DIC), which is similar to the AIC in interpretation, but which makes use of an estimate of the effective number of parameters (Spiegelhalter et al., 2002), derived from the variance of the log posterior likelihood. The empirical DIC from a set of samples is:

$$\mathrm{DIC} = -2\log\left(p(\mathbf{y}|\hat{\epsilon})\right) + 4\mathrm{Var}_s\left[\log(p(\mathbf{y}|\vec{\epsilon}_s))\right] \tag{3.33}$$

Here, $\hat{\epsilon}$ is the posterior mean of $\vec{\epsilon}$ and Var_s is the variance of the log likelihood across samples. Note that while the samples in question are taken using the posterior, this computation is done using the likelihood. In the results, the model with the more negative DIC is favored. The interpretation of ΔDIC is similar to that of the AIC and BIC, in which differences of $>\sim 6$ are strong evidence in favor of the model with the lesser DIC (e.g. Kass & Raftery (1995) for BIC).

To produce posterior predictive mass-flux-radius relations, we assume the planets are old (5 Gyr.), and for given M and F, we draw M_z from Eq. 3.8 and ϵ_i from $\epsilon(F, \vec{\phi})$ marginalized over the posterior $p(\vec{\phi}|\vec{R}_{obs})$. These sampled values are then

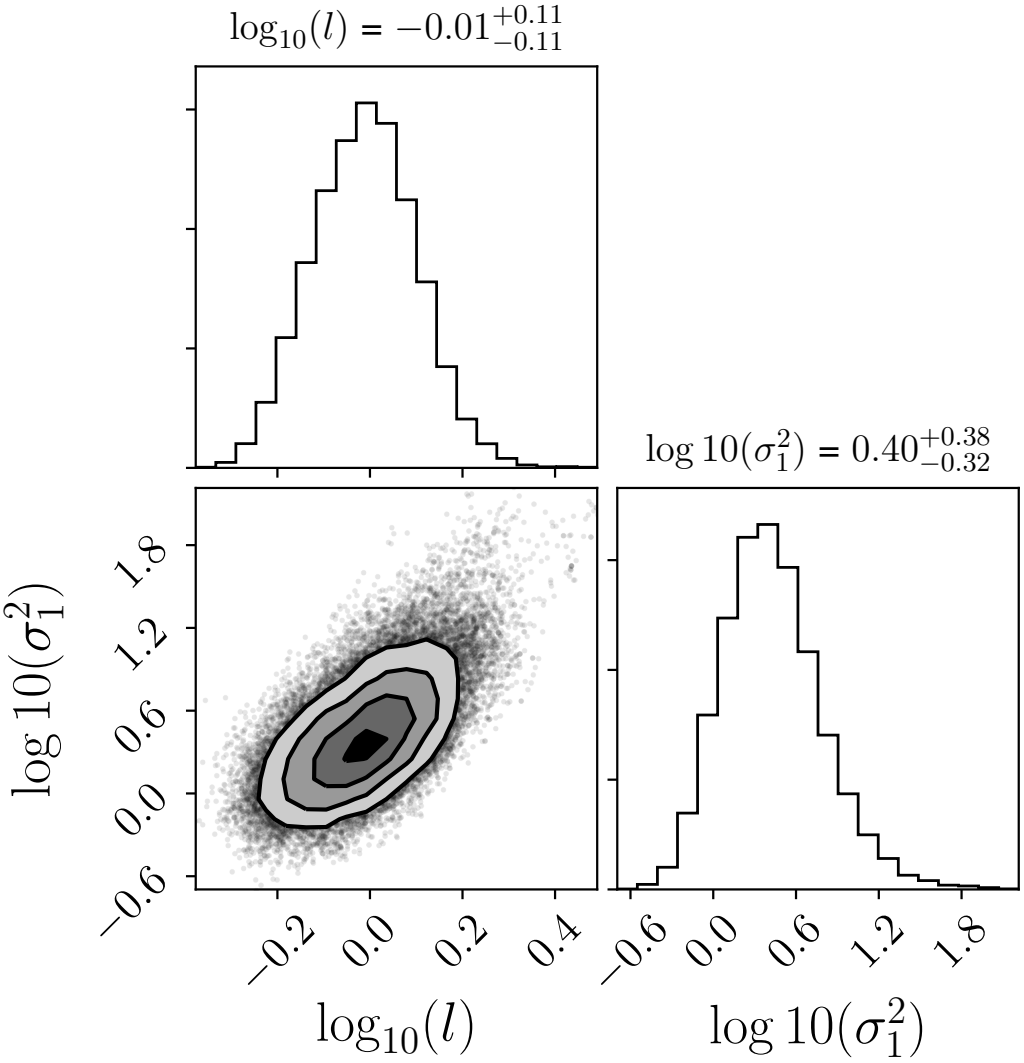

Figure 3.7: A scatterplot matrix of the GP hyperparameter posterior (see eq. 3.21). It is fairly well-behaved, but has a long right tail. This is a common feature for Gaussian processes.

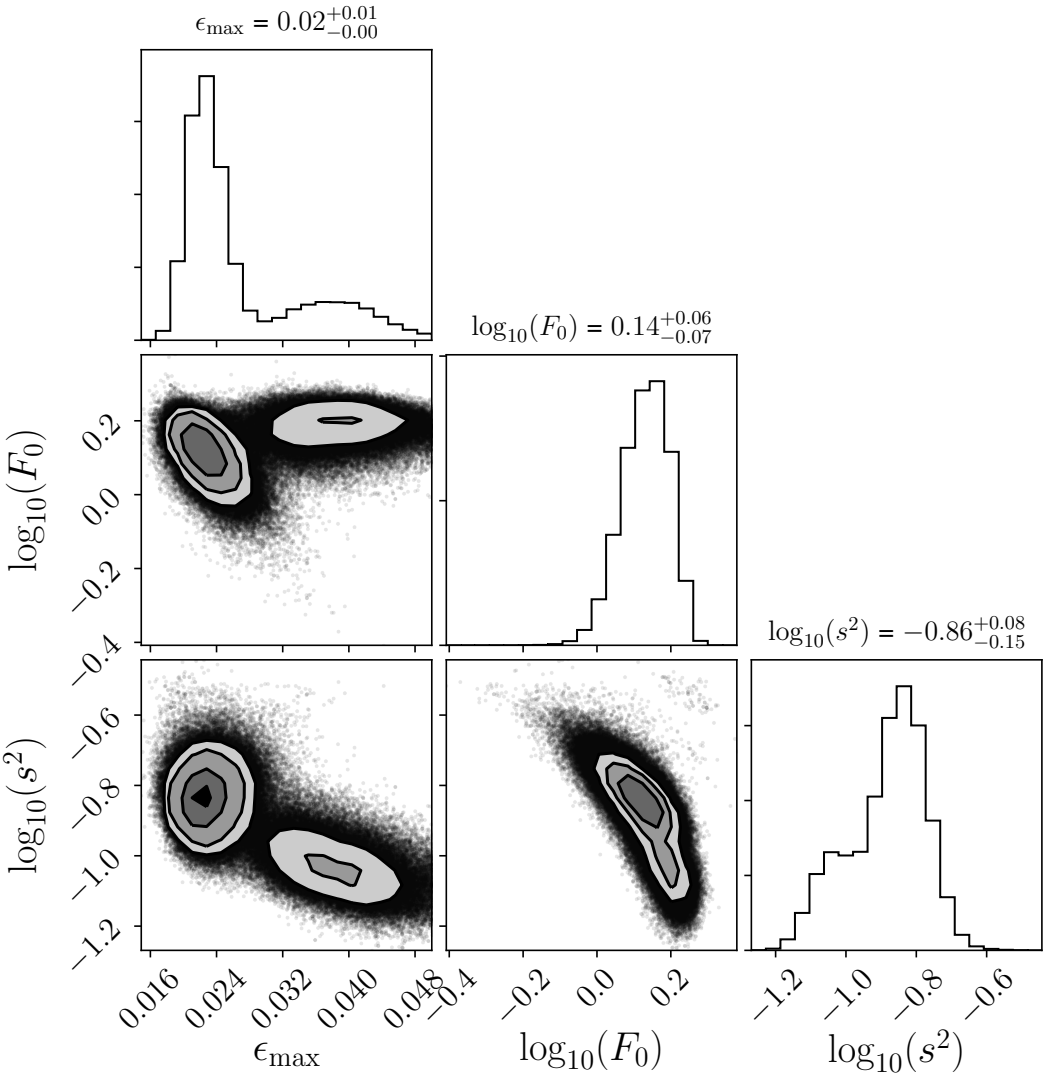

Figure 3.8: A scatterplot matrix of the Gaussian function hyperparameter posterior (see eq. 3.16). Two modes were observed, differing primarily in height $\epsilon_{\max}$; the model with a peak of $\epsilon \approx 2\%$ is favored over the model with peak $\epsilon \approx 3.5\%$ by a probability ratio of about 75% to 25%. The discovery of more giant planets around the ≈ 1500 K peak will help to resolve this further.

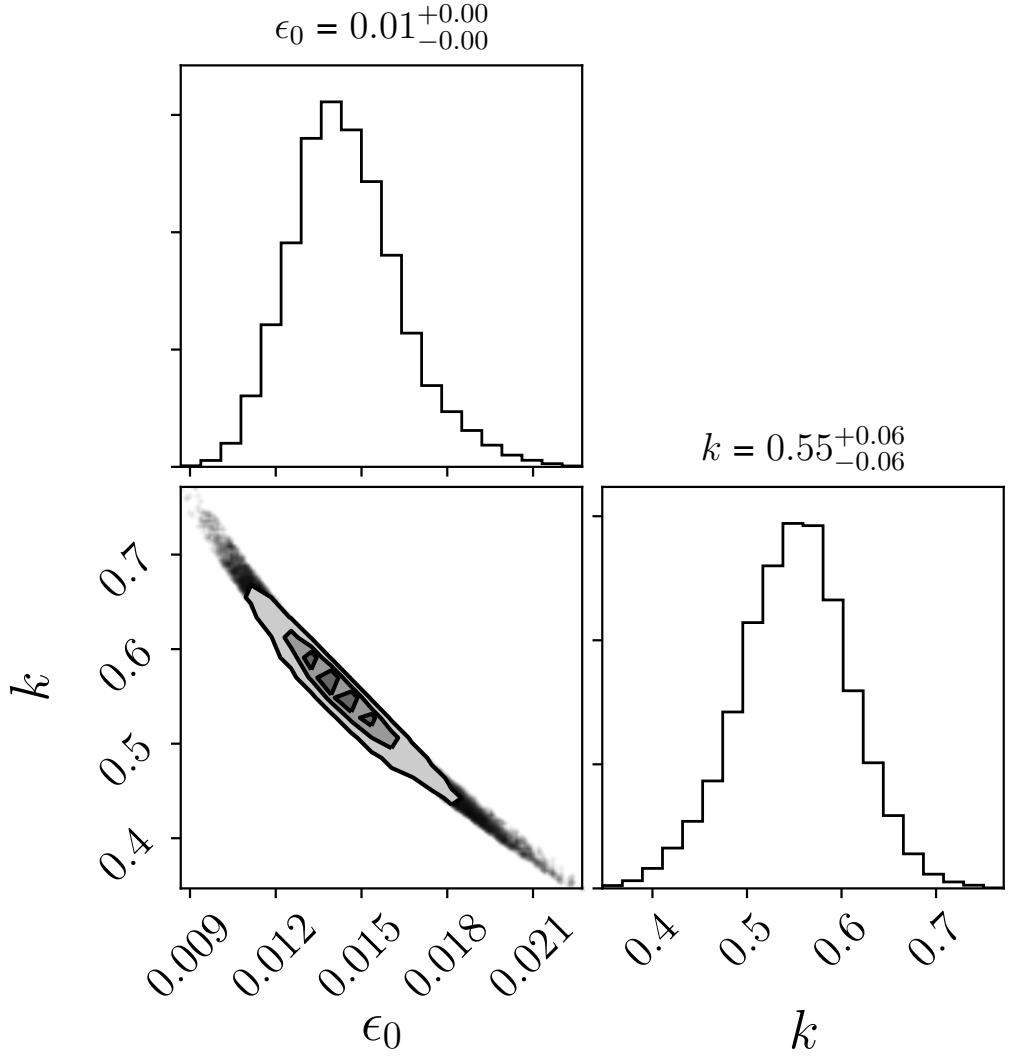

Figure 3.9: A scatterplot matrix of the power law hyperparameter posterior (see eq. 3.14. A strong correlation between the coefficient F_0 and the power k is seen. This likely reflects the constraint that the function achieve adequate power for the many planets at around $T_{eq} \approx 1300$ K, yet avoid exceeding 5% for the hottest planets, which would exceed the bounds of our grid. Such constraints are difficult for the power-law to achieve. Regardless, as a result of its overestimate of high T_{eq} radii, this model had a comparatively disfavorable DIC.

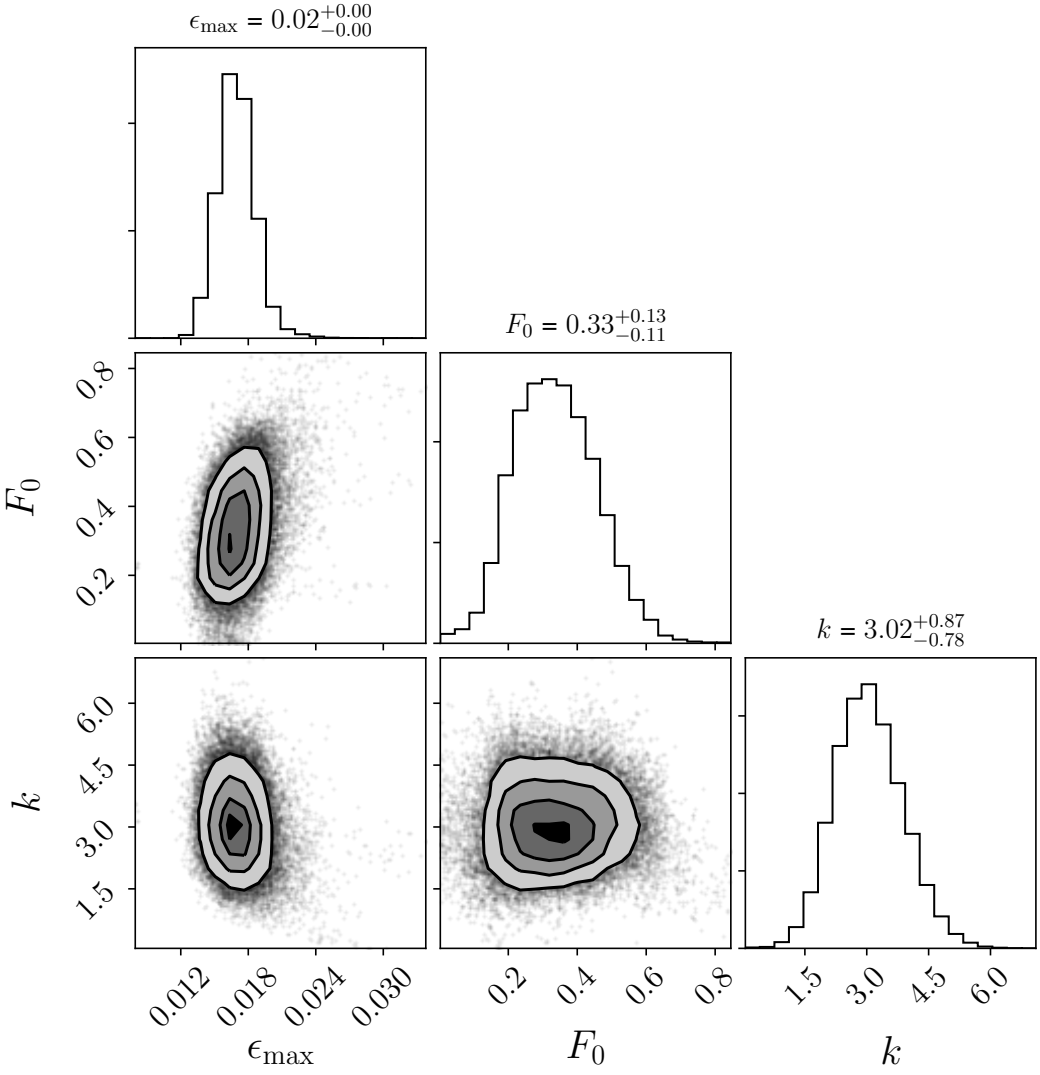

Figure 3.10: A scatterplot matrix of the logistic function hyperparameter posterior (see eq. 3.15). Thanks to our prior on k, which demanded the transition be similar to the scale of the data, the resulting posterior is well-behaved and easy to sample from. The model is not bad, but its DIC indicates that it is still inferior to a model which decreases at high equilibrium temperatures.

plugged into the structure models $R(t, M_z, M, \epsilon, F)$. The result is a probability distribution in R for the given parameters.

3.5 Results

The results for $\epsilon(F)$ are shown in Figure 3.11. All functional forms yield similar results below about 0.5 Gerg s^{-1} cm^{-2}, but differ significantly above this. The GP model reaches a peak at around 1600 K and decreases towards zero with high statistical confidence, as shown by the uncertainty bounds. At high fluxes, the uncertainty in heating power is roughly constant, and so declines as a fraction of flux. Figure 3.2 shows the predicted radius for a given mass of 5 Gyr old planets of average (posterior mean) composition and inflation power using the GP model. The predictions align well with planets of similar mass and temperature. The shape of $\epsilon(F)$ presented by the GP is corroborated by comparison of the DIC values. Of the parametric models, the Gaussian model is most favored, with a DIC of -1723. The logistic model was next, at -1648, followed by the power-law model at -1641. We interpret this to mean that ϵ decreases towards zero at high fluxes with high statistical significance, in agreement with our conclusions from the GP approach. The DIC of the GP model is -1723, so there is no significant preference between it and the Gaussian model. We present the Gaussian model since it takes a simple analytic form, as a percent of flux and with flux in units of Gerg s^{-1} cm^{-2}:

$$\epsilon = \left(2.37^{+1.3}_{-.26}\right) \mathrm{Exp}\left[-\frac{\left(\log(F) - \left(.14^{+.060}_{-.069}\right)\right)^2}{2\left(.37^{+.038}_{-.059}\right)^2}\right] \tag{3.34}$$

Note that for planets whose interiors are in thermal equilibrium where $E_{in} = E_{out}$ and therefore $dR/dt = 0$ (which may happen quite early – see Fig. 3.4), the

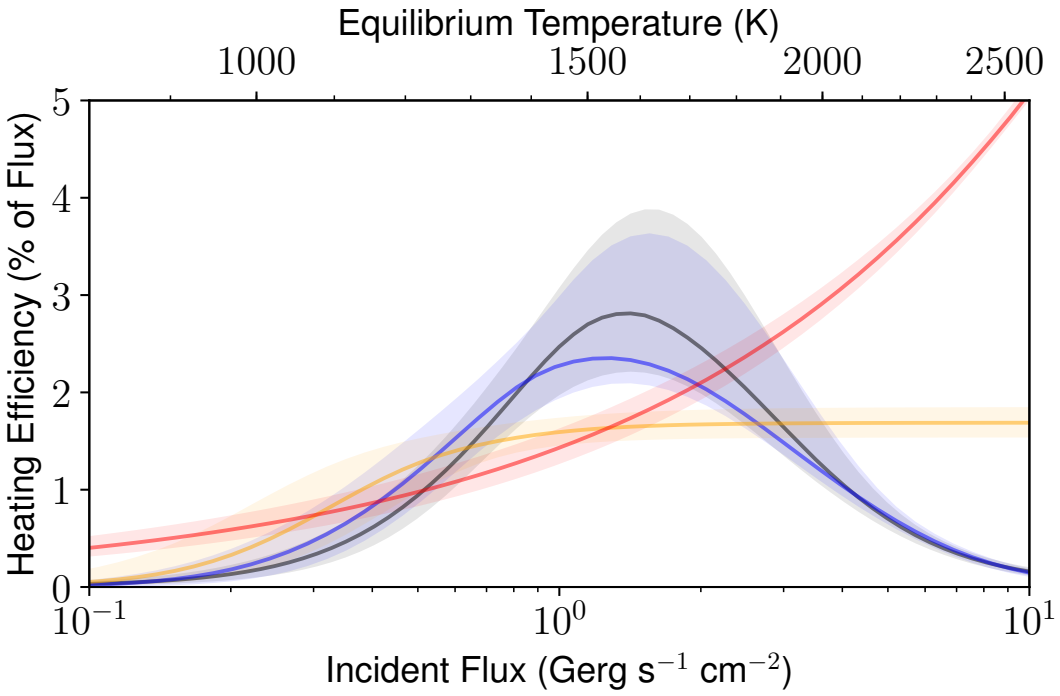

Figure 3.11: The posteriors of our statistical models of inflation power (as a percent of flux) against incident flux, with 1σ uncertainty bounds. The red line is a power-law model, yellow is logistic, blue is Gaussian, and black is the GP. The Gaussian model is strongly favored over the other parametric models by the DIC model selection criterion, and the GP strongly indicates a negative relationship at high flux. This decrease in inflation efficiency at higher fluxes is important, because it matches predictions from the Ohmic dissipation mechanism of hot Jupiter inflation.

intrinsic temperature is directly related to ϵ as:

$$T_{int} = \left(\frac{\epsilon F}{4\sigma}\right)^{\frac{1}{4}} = \epsilon^{\frac{1}{4}} T_{\rm eq} \tag{3.35}$$

where σ is the Stefan-Boltzmann constant, and the conversion from flux to equilibrium temperature assumes an ideal black body with full heat redistribution.

To visualize why the Gaussian model is preferred, we compute the posterior predictive radius distributions, and compare them to the radii of our observed

planets. Figure 3.12 compares these predictions for the favored GP model and the next-best logistic model to the observed radii as a function of incident flux, divided into six mass bins. The models only diverge at high fluxes, about 2 Gerg s^{-1} cm^{-2}. Beyond this, the logistic model systematically overestimates the radii, and the GP does not. To make this clear, Figure 3.13 shows the residual to the expected radius (the radius anomaly) for high fluxes under a no inflation model, the logistic model, and the Gaussian model. Here, the increasing bias of the logistic model for the 30 planets at such high fluxes is apparent. Even a flat ϵ at high flux predicts overly large planets, hence our conclusion that $\epsilon(F)$ must decline.

For our model of thermal tides (Arras & Socrates, 2009), we examined the scaling relations for thermal tides from Socrates (2013) (Eq. 3.26), and found this potential power source to much too strongly increase with flux to reproduce the observed radii. The variance also appears overly high; for example, the scaling relations force ϵ to vary by more than an order of magnitude just in planets with fluxes between 0.8 and 1.2 Gerg s^{-1} cm^{-2}. As a result, we encountered considerable difficulty getting the model (see section 3.4.1) to fit. We were only able to fit a model by imposing the regularizing constraint that ϵ for any individual planet cannot exceed 4.5%, a level far above what is otherwise needed to explain the observed radii. Under this requirement, we measure $\log_{10}(\epsilon_0) = -1.61 \pm .065$, Figure 3.14 shows the the inferred heating efficiencies for the sample planets as a function of flux. The MCMC was able to fit the bulk of the data by placing them in the $.5 - 3\%$ range, but the scaling is far too extreme. In explaining the bulk of the planets, a huge 43% (122/281) of the data exceeded the upper bound. Without the constraint, very few of the planets actually end up inflated; the range of coefficients to ϵ_0 given by the scaling relation from Socrates (2013) is simply

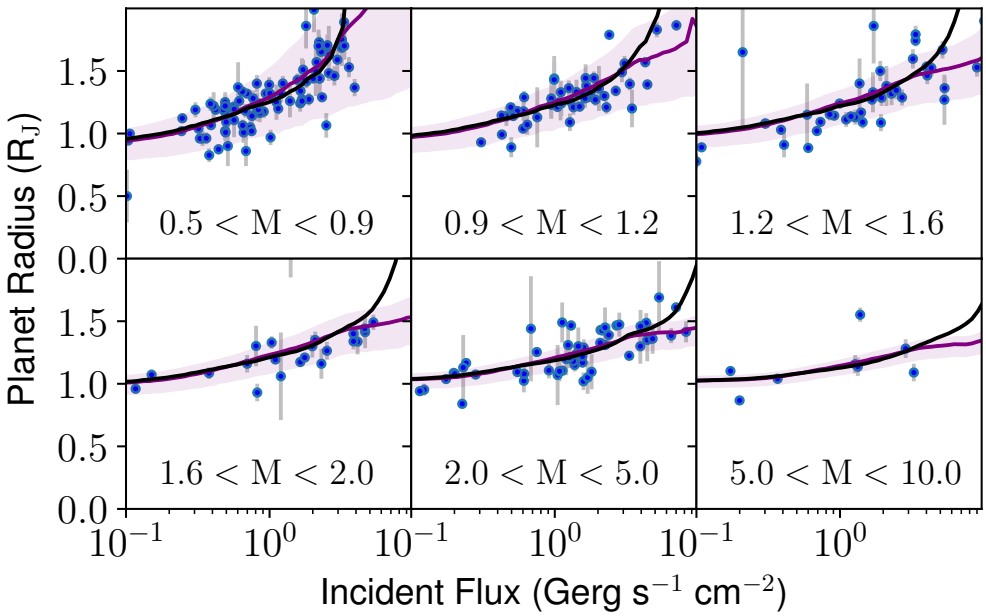

Figure 3.12: The radii of transiting giant planets against flux, divided into six mass bins. The blue line and region are the Gaussian model's predicted radius and 1 σ uncertainty bounds. The black line is the prediction for the next best model, the logistic function. The latter makes similar predictions but over-predicts radii of high flux planets, so the DIC favors the Gaussian model by a statistically significant margin. This is more obvious looking directly at the residuals, which are shown in Fig. 3.13.

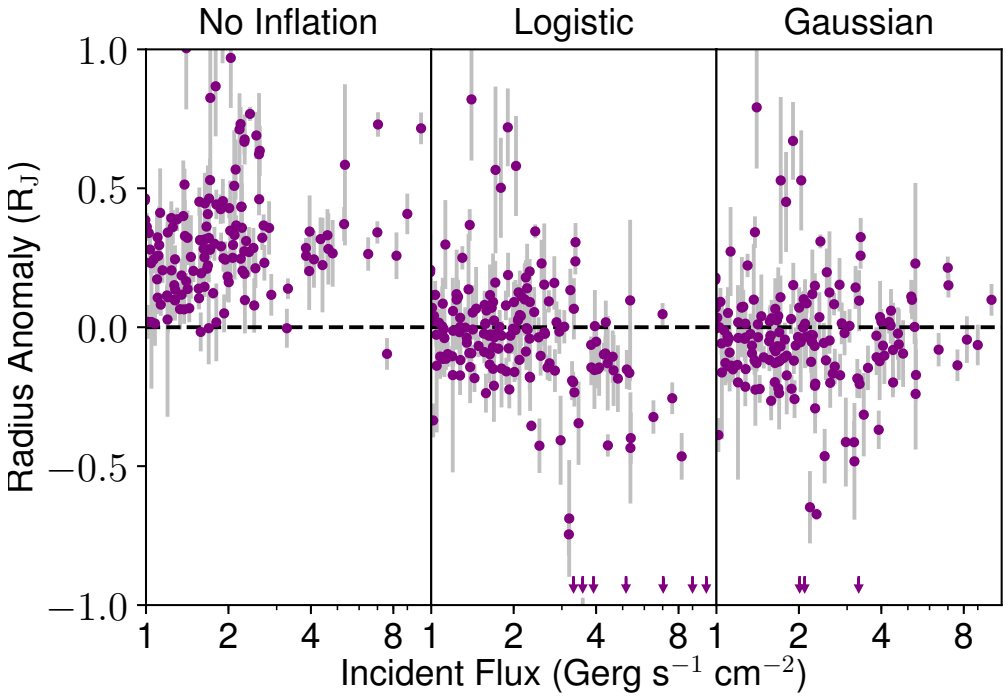

Figure 3.13: The difference between observed and predicted radius plotted against incident flux assuming typical composition planets under the cool giant model (no inflationary effect), the logistic model, and the Gaussian model (see Fig. 3.11). Arrows show the handful of planets where the model exceeded the observed radius by more than 1 R_J, which typically occurs only for very hot, very low mass planets whose radii are extremely sensitive to bulk metallicity. Heavy-element abundance variations Thorngren et al. (2016) are sufficient to explain the scatter (see Fig. 3.12). Error-bars depict observational error only. The plot illustrates why our statistical tests prefer the Gaussian model over the logistic model: the logistic model consistently overestimates the radii of planets at high fluxes, while the Gaussian model does not.

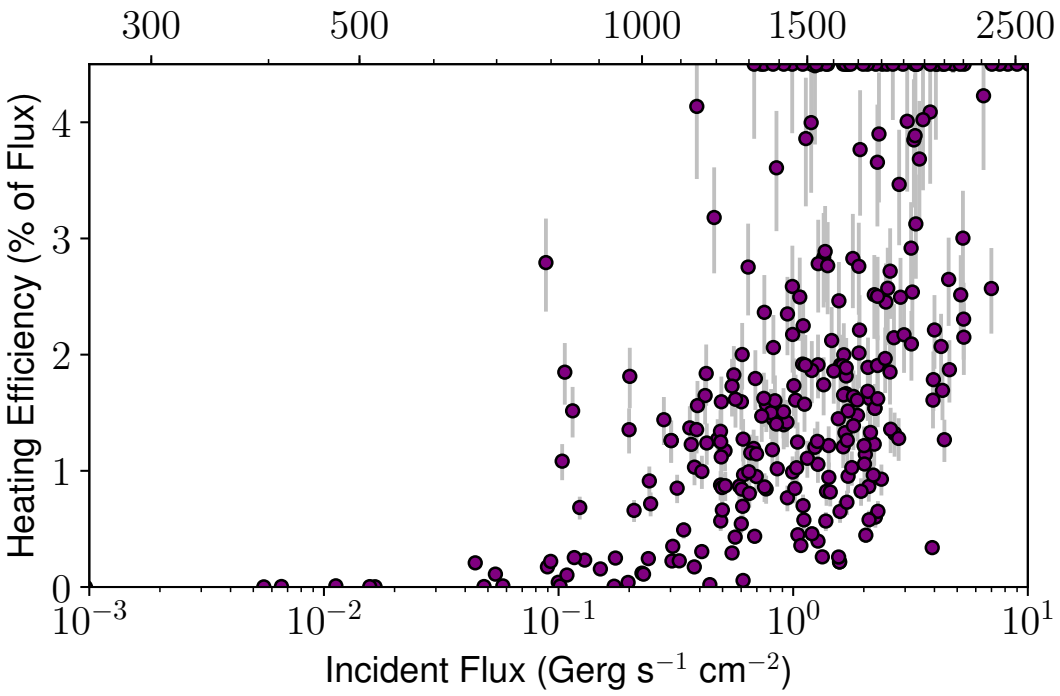

Figure 3.14: The posterior heating efficiencies for our sample planets as a function of flux, using the thermal tides scaling relationship from Socrates (2013) but leaving a constant scaling factor as a fit parameter. The match with observations was poor, as it forces ϵ to vary by orders of magnitude in ways not apparent in the planet radii. The DIC was -1642, much lower than the GP or gaussian models, though this was likely affected by our constraint that $\epsilon < 4.5\%$. A large fraction of the data (43% or 122/281) exceeded this upper bound and was clipped down to 4.5%.

too large. As such, we conclude that the dominant source of inflation power in the observed population does not follow the thermal tides scaling relation.

3.6 Discussion

The Gaussian shape is significant because it exclusively matches predictions of hot Jupiter inflation from the Ohmic dissipation mechanism. Under this model, magnetic interactions transfer energy from the atmosphere of a planet into its

interior (Batygin & Stevenson, 2010). The effect is initially increasing with greater atmospheric temperatures and therefore ionization, but at very high temperatures the magnetic drag on atmospheric winds (Perna et al., 2010) inhibit the process (Menou, 2012; Batygin et al., 2011). Batygin et al. (2011) predicts a scaling with equilibrium temperature as $\epsilon \propto (1500\mathrm{K}/\mathrm{T_{eq}})^4$. Menou also derives scaling laws for this effect, estimating the peak ϵ to occur at 1600 K, depending on the planetary magnetic field strength (Menou, 2012). Ginzburg & Sari (2016) supports this conclusion, estimating a peak ϵ to occur at 1500 K, with power-law tails on either side. Finally, MHD simulations in Rogers & Komacek (2014) find a peak at 1500-1600 K. Figure 3.11 shows that the posteriors of our favored models match these predictions well. If Ohmic dissipation is responsible for our observation, then our measured $\epsilon(F)$ is presumably the average over various planetary magnetic field strengths.

A noteworthy difficulty with identifying our results with the Ohmic dissipation model is the depth at which the anomalous heat is deposited. Our model assumes that anomalous heating is efficiently conducted into the interior adiabat. Ohmic heating, however, is generally believed to be deposited at pressures low enough that only a portion of the deposited energy is inducted into the adiabat and a delayed cooling effect is produced (Spiegel & Burrows, 2013; Wu & Lithwick, 2013; Komacek & Youdin, 2017). Indeed, Rogers & Komacek (2014) do not see sufficient heating to explain the observed radii. As well as differing from our modeling assumptions, this appears inconsistent with the results of Hartman et al. (2016), who observe re-inflation of giants as their parent stars age and brighten over their main-sequence lifetime. This effect would be prohibitively slow in the shallow deposition case (Ginzburg & Sari, 2016). Thus if Ohmic heating is to explain our results, it must either violate these predictions or be modified by an

additional effect which ushers the heat further into the planet. The advection effects proposed by Tremblin et al. (2017) show that such effects are plausible and that there is still a great deal left to understand about atmospheric flows in hot Jupiters.

As the results of Tremblin et al. (2017) stand, our observations to not seem to support them as the sole cause of inflation. They predict observable inflation occurring well below the observed 0.2 Gerg s^{-1} cm^{-2}threshold, and do not appear to support a decrease in efficiency at high flux. However, our results might align better if temperature-dependent wind speeds are considered within their model, which could slow flows both at especially low and high $T_{\rm eq}$. Slower winds at high $T_{\rm eq}$ would be a natural consequence of magnetic drag (Perna et al., 2010). We view our results here as support for the idea that magnetic drag is quite important in the hottest atmospheres.

Other candidate inflation models do not match our results very well. Tidal heating may introduce non-negligible energy into planet interiors, but cannot fully explain the anomalous radii (Miller et al., 2009; Leconte et al., 2010), and would not reproduce our relationship with flux. The thermal tides mechanism (Socrates, 2013) appears to predict more variation in ϵ than can plausibly exist (see Fig. 3.14). Delayed cooling models propose that no anomalous heating occurs and that radii anomalies instead result from phenomena which prevent the escape of formation energy, such as enhanced atmospheric opacities (Burrows et al., 2007) or inefficient heat transport in the interior (Chabrier & Baraffe, 2007). This energy would otherwise rapidly radiate away. The issue with these proposals is that they do not inherently depend on flux and cannot explain the results of Hartman et al. (2016). Furthermore, in the case of layered convection (see Leconte & Chabrier, 2012) resulting in delayed cooling (Chabrier & Baraffe, 2007), structure evolution

simulations in Kurokawa & Inutsuka (2015) show that layered convection would not occur in young giants, and that even if layers are imposed, they would need to be implausibly thin ($1 - 1000$cm) to achieve the observed radii.

The situation for Saturn-mass planets (those excluded from our model) remains puzzling. As described in Section 3.2, these exhibit a different relationship with flux than Jupiter mass planets (Fig. 3.2) and have been found less frequently in high flux orbits than their higher-mass analogs (Fig. 3.3). Inefficiency in the heating mechanism, perhaps by lower magnetic field strengths, could explain the former observation, but not the latter. Furthermore, Pu & Valencia (2017) recently showed that Ohmic dissipation should occur in Neptunes, so we can reasonably expect that it would work on Saturns as well. Some observational biases are doubtless present, but would likely not produce the effects seen. Thus it seems possible that mass loss is occurring. However, the exact mechanism would be unclear; for example, neither XUV driven mass-loss (Yelle, 2004; Lopez et al., 2012) nor boil-off (Owen & Wu, 2016) appear to significantly affect planets in this mass range. As such, the cause of these observations is an open question.

There is still much work to be done in understanding hot Jupiter radius inflation. A promising avenue are the case of "reinflated" hot Jupiters, which are planets whose radii may be increasing over time as their stars evolve off the main sequence and brighten (Lopez & Fortney, 2016). Grunblatt et al. (2017) have conducted promising observations of two potentially re-inflated planets around sub-giant stars. Our posterior radius predictions are closer to their observations under the re-inflated case, but more planets will be needed to establish strong statistical significance. Comparing the main-sequence reinflation results of Hartman et al. (2016) with structure models could reveal the timescale of re-inflation, which is closely related to the depth of energy deposition (Komacek & Youdin,

2017; Ginzburg & Sari, 2016). If re-inflation does indeed occur, delayed cooling models are ruled out. Follow-up work of Tremblin et al. (2017) to determine how their results would be affected by temperature-dependant wind speeds would also be helpful. Finally, further magnetohydrodynamic simulations are needed to properly understand heat flow in the outer layers of these planets. Our results add to this picture by providing strong evidence of a heating efficiency drop at high temperatures and thereby pointing us towards the Ohmic dissipation model; they also suggest that 3-D atmospheric circulation models need to take magnetic fields into account.

4. Atmosphere and Interior Composition

4.1 Introduction

Spectroscopic characterization of exoplanet atmospheres has proven to be an invaluable tool in understanding the nature and formation of giant planets. Under the core accretion model of giant planet formation (see Pollack et al., 1996), these planets are records of the disks from which they formed. For example, the C/O ratio of a planet may depend on where it formed relative to the ice lines of water, methane, CO, and CO_2 and the relative accretion of solids and gas (Öberg et al., 2011; Madhusudhan et al., 2014; Mordasini et al., 2016; Espinoza et al., 2017). Many studies have collected emission and transmission spectra for purpose of determining molecular abundances, e.g. Swain et al. (2010); Line et al. (2014); Kreidberg et al. (2018); Wakeford et al. (2018), often using the *Spitzer* and/or *Hubble* Space Telescopes. These observations can also reveal the presence of hazes and clouds (e.g. Fortney, 2005; Sing et al., 2011; Gibson et al., 2012; Mandell et al., 2013; Morley et al., 2013; Kreidberg et al., 2014a) as well as atmospheric temperature structure, including whether a temperature inversion is present (Knutson et al., 2008; Fortney et al., 2008; Burrows et al., 2008; Madhusudhan et al., 2011;

Evans et al., 2016).

With the recent successful launch of the Transiting Exoplanet Survey Satellite (*TESS*; see Ricker et al., 2015), many more planets amenable to spectroscopic follow-up are likely to be discovered (Barclay et al., 2018; Sullivan et al., 2015; Huang et al., 2018). Additionally, the *James Webb Space Telescope* (*JWST*; see Gardner et al., 2006) will allow for measurements in new wavelength ranges with unprecedented precision (Beichman et al., 2014; Bean et al., 2018).

An important driver in atmospheric measurements is determining the metallicity of the planetary atmosphere (Fortney et al., 2013), which can be compared to predictions of formation models. However due to degeneracies in determining atmospheric abundances (first identified in Benneke & Seager, 2012), error bars on the abundances of atoms and molecules of interest can often be large (see also Griffith, 2014; Line & Parmentier, 2016; Heng & Kitzmann, 2017; Fisher & Heng, 2018). This can manifest itself as a strong prior dependence (see e.g. Oreshenko et al., 2017). As such, it would be helpful to have an additional source of information or constraint about the atmosphere's metallicity.

Interior structure models can help in this case. For planets with known masses and radii, we can infer the bulk metallicity Z_p through the use of planet evolution models which are used to understand the planetary radius over time, as in Thorngren et al. (2016). The equations of state for the most common metals (say, oxygen and carbon) at megabar pressures are similar enough (e.g. compare Thompson, 1990; French et al., 2009) that this approach is insensitive to the exact metals in question. Iron's high density makes it an exception, but its lower abundance (Asplund et al., 2009) makes this unimportant for our purposes.

Of course even knowing Z_p exactly does not directly imply an atmosphere metallicity. Even in the simplest model where the atmosphere and the entire H/He

envelope share the same composition, some metals will likely be sequestered in the core. In more complex models, interior composition gradients could lead to an increasing metallicity with depth in the H/He envelope (e.g. Leconte & Chabrier, 2012; Vazan et al., 2016). However, cases where Z increases going outward in the planet will not be long-lived, succumbing either to Rayleigh-Taylor instability or ordinary convection. Therefore the planet's bulk metallicity serves as an upper limit on the atmospheric metallicity. We define the "visible metal fraction f" – that observed in the atmosphere – as the ratio of atmospheric metallicity Z to the bulk metal, Z_p:

$$Z = fZ_p \tag{4.1}$$

The atmosphere cannot be more metal-rich than the interior, so $0 \leq f \leq 1$, and Z_p is an *upper limit* on the metallicity of the atmosphere.

Using this approach, we have previously helped to constrain metallicity in retrievals for two cases already. For GJ 436b (Morley et al., 2017), interior structure models were helpful in contextualizing the inferred high atmospheric metallicity and connecting it to the large intrinsic flux suggested by the spectrum. For WASP-107b (Kreidberg et al., 2018), we were able to help rule out a high-metallicity atmosphere, in agreement with the spectroscopic observations.

In this work, we seek to provide upper limits on atmospheric metallicity to assist with atmospheric retrieval modeling for every planet with sufficient data to support this. We also discuss prior predictive distributions for the atmospheric metallicity, as well as fits to the upper limits so that future planet discoveries can easily produce limit estimates for planets with measured masses and radii.

Our data consists of transiting planets with RV and/or TTV follow up, downloaded and merged from the NASA Exoplanet Archive (Akeson et al., 2013) and Exoplanets.eu (Schneider et al., 2011). We consider only planets nominally massed

between 20 $M_\oplus$ and 20 M_J whose relative mass and radius uncertainties are $< 50\%$. We exclude hot Saturns, which we define as planets with mass $M < .5M_J$ and flux $F > 0.5$ Gerg s^{-1} cm^{-2}, as these planets are not well modeled by the inflated radius fits of Thorngren & Fortney (2018). An exception was made to include the potential JWST GTO object WASP-52 b, which was just over the line ($M = .46$ M_J, $F = .65$ Gerg s^{-1} cm^{-2}) but appears to be well-modeled. These criteria resulted in the selection of 403 planets: 70 Saturns, 35 cool Jupiters, and 298 hot Jupiters. The boundary between cool and hot Jupiters, by our definition, is .2 Gerg s^{-1} cm^{-2}, below which significant radius inflation does not occur (Miller & Fortney, 2011; Demory & Seager, 2011).

4.2 Methods

Following Fortney et al. (2013), consider a mass M of gas with a metal mass fraction Z. The mass of the hydrogen and helium is $M(1-Z)$, and the mass of the metals (everything else) is MZ. Thus, given the mean molecular mass of the hydrogen (μ_H) and metals (μ_Z), the number of hydrogen and metal molecules is $N_H = M(1-Z)(X/(X+Y))/\mu_H$ and $N_Z = MZ/\mu_Z$ respectively. From this, we can compute the metal abundance ratio Z:H (by number) as:

$$Z{:}H = \frac{N_Z}{N_H} = \frac{MZ/\mu_Z}{M(1-Z)(X/(X+Y))/\mu_H} \tag{4.2}$$

$$= \frac{1+Y/X}{(Z^{-1}-1)(\mu_Z/\mu_H)} \tag{4.3}$$

Satisfyingly, this is independent of mass and only depends on Z, the H/He mass ratio Y/X, and the ratio of the mean molecular masses μ_Z/μ_H. For our calculations, we use $\mu_H = 2$ AMU (molecular hydrogen), $\mu_Z = 18$ AMU (water), and $Y/X = .3383$ (Asplund et al., 2009). Models reflecting individual planetary

chemistry can be similarly constructed; as Heng (2018) reminds, "atmosphere metallicity" is ambiguous, so extra care should be taken here. Often in atmosphere modeling, this is parameterized in units relative to the metal abundance of the solar photosphere $Z{:}H_\odot = 1.04 \times 10^{-3}$ (Asplund et al., 2009). We will use these units implicitly for the remainder of this chapter.

In some atmospheric retrievals, the authors have opted not to lock different metal abundances to fixed ratios (e.g. Oreshenko et al., 2017). For these cases Eq. 4.3 can still be useful. To handle this, one must compute the total metallicity from the individual abundances (potentially making assumptions about unmodelled abundances). One should also compute the mean molecular mass of the metals if they differ significantly from the assumed 18. Using the new mean molecular mass of the metals μ_Z, our tabulated $Z{:}H$ can simply be scaled by a factor of $18/\mu_Z$. Note that this procedure only informs us of the total metal abundance, not individual molecular abundances.

From here we can proceed in two different ways. First, in §4.2.1, we will combine Eq. 4.3 with the mass metallicity relation from Thorngren et al. (2016). This results in a distribution for $Z{:}H$ which depends only on f and the planet mass. This is a useful as a baseline expectation for the planet population, but when considering individual planets we wish to also account for their observed radii, insolation, and age to get a more precise estimate. For this, we combine Bayesian statistical models with interior structure models in §4.2.2, which we then apply separately to each planet from our sample in turn. The results of these calculation are discussed in §4.3.

4.2.1 Prior Predictive

A simple way to estimate the bulk metallicity of the planet is to make use of the planetary mass-metallicity relation we identified in Thorngren et al. (2016), which takes the following form:

$$M_Z = \alpha' M^{\beta'} 10^{\pm \sigma_Z} \tag{4.4}$$

When M_Z and M are in Jupiter masses, $\alpha' = .182$, $\beta' = .61$, and $\sigma_Z = .26$. We can neglect uncertainty in the parameters because the predictive uncertainty is dominated by the residual spread σ_Z. This can be easily converted to a prior on bulk Z_p as follows:

$$\log(M_Z) = \alpha + \beta' \log(M) \pm \sigma_Z \tag{4.5}$$

$$\log(M_Z/M) = \alpha + (\beta' - 1) \log(M) \pm \sigma_Z \tag{4.6}$$

$$\log(Z_p) = \alpha + \beta \log(M) \pm \sigma_Z \tag{4.7}$$

Here, $\alpha = \log_{10}(\alpha') = -.7395$ and $\beta = \beta' - 1 = -.39$ for brevity. Combining equations 4.3 and 4.7, we can produce a prior on the relative number fraction of metals:

$$Z{:}H = \frac{1 + Y/X}{(\mu_Z/\mu_H)(f^{-1} 10^{-\alpha \pm \sigma_Z} M^{-\beta} - 1)} \tag{4.8}$$

From this, we can compute the expected amount of metal in an atmosphere given the mass of the planet and f. The maximum atmospheric metal abundance $Z{:}H_{\max}$ occurs when $f = 1$. To account for the additional information available from radius, age, and flux, we will include structure evolution modeling using a Bayesian framework in the next section. These techniques are not wholely

separate, however: Eq. 4.8 is the prior predictive distribution with respect to that more sophisticated model.

4.2.2 Statistical Models

Our statistical model seeks to identify structure parameters which reproduce the observed radius $R_{\rm obs}$, accounting for the observational uncertainty σ_R. The parameters we consider are the planet mass M in Jupiter masses, the bulk planet metallicity Z_p, the anomalous heating efficiency ϵ, and the age of the planet t in Gyr. Thus, we construct the following likelihood:

$$p(R_{\rm obs}|M, Z_p, \epsilon, t, \sigma_R) = \mathcal{N}(R_{\rm obs}|R(M, Z_p, \epsilon, t), \sigma_R) \tag{4.9}$$

Here, $R(M, Z_p, \epsilon, t)$ refers to the radius output of our structure models, and $\mathcal{N}(\mu, \sigma)$ is the a normal distribution with mean μ and standard deviation σ; $\mathcal{N}(x|\mu, \sigma)$ indicates the distribution's PDF should be evaluated at x (the same notation will be used for other distributions later).

The priors for M and t are the observed mass and age of the planet, with the latter truncated between 0 and 14 Gyr, since we are confident that the planets are not older than the universe.

$$p(M) \sim \mathcal{N}(M_{obs}, \sigma_M) \tag{4.10}$$

$$p(t) \sim \mathcal{TN}(t_{obs}, \sigma_t, 0, 14) \tag{4.11}$$

We use $\mathcal{TN}(\mu, \sigma, x_0, x_1)$ to refer to a truncated normal distribution with mean μ, standard deviation σ, and upper and lower limits x_0, x_1. The prior for Z_p comes

from the mass-metallicity relation (Eq. 4.7).

$$p(Z_p|M) \sim \mathcal{LN}(\alpha + \beta \log_{10}(M), \sigma_Z) \tag{4.12}$$

We use $\mathcal{LN}(\mu, \sigma)$ to indicate a log normal distribution, where the $\log_{10}$ of the parameter is normally distributed with mean μ and standard deviation σ.

Hot Jupiter radius inflation represents a complicating factor in constructing evolution models for these objects. We handle the anomalous heating efficiency ϵ using the Gaussian process posterior predictive results from Thorngren & Fortney (2018). There we inferred anomalous heating as a function of flux by adjusting it to match the modelled radius to the observed radius. The composition was assumed to follow the same distribution as the warm giant planets, since they are in similar mass and orbital regimes. Because of their extra degree of freedom, we see larger (but manageable) uncertainties on the bulk metallicities for hot Jupiters.

$$p(\epsilon) \sim \mathcal{LN}(\epsilon(F), \sigma_\epsilon(F)) \tag{4.13}$$

Thus, we are using the trends in composition and heating efficiency ϵ that reproduced observed radii of the giant planet population as the priors for individual planets. Combining the likelihood (Eq. 4.9) and priors (Eq. 4.10- 4.13), we obtain a posterior proportional to:

$$p(M, Z_p, \epsilon, t|R_{obs}, \sigma_R) \propto p(R_o|M, Z_p, \epsilon, t, \sigma_R)p(M)p(Z_p|M)p(\epsilon)p(t) \tag{4.14}$$

$$\propto \mathcal{N}(R_{\rm obs}|R(M, Z_p, \epsilon, t), \sigma_R)\mathcal{N}(M|M_{obs}, \sigma_M) \tag{4.15}$$

$$\mathcal{LN}(Z_p|\alpha + \beta \log_{10}(M), \sigma_M)\mathcal{LN}(\epsilon|\epsilon(F), \sigma_\epsilon(F))$$

$$\mathcal{TN}(t|t_{obs}, \sigma_t, 0, 14)$$

We sampled from this posterior separately for each planet using a Metropolis-Hastings sampler (Hastings, 1970), drawing 10,000 samples in each of four independent chains, burning in for 100,000 samples and recording only every 100^{th} sample (thinning) thereafter. Convergence was evaluated using the Gelman-Rubin diagnostic (Gelman & Rubin, 1992) and acceptance rates, as well as visual inspection of the autocorrelation plots, trace plots, and corner plots (Foreman-Mackey et al., 2013). As an example, Fig. 4.1 depicts the posterior distribution for WASP-43b. We can see that its metallicity is $Z_p = .35 \pm .08$, uncorrelated with other parameters because the primary source of uncertainty (in this case) is the radius measurement. With these posterior samples in hand, we can derive a distribution for Z:H from Z_p using Eq. 4.3, assuming $f = 1$, which yields Z:H of $80.35 \pm 27.5\times$ solar. We use the 95^{th} percentile of this distribution as our upper limit, which for WASP-43b is $131\times$ solar.

4.3 Results

4.3.1 Known Planets

Our main results are the upper limits on atmospheric metallicity Z:H_{max}, a selection of which are shown in Table 4.3.1 along with the input parameters we used for each planet. The posterior means and standard deviations of Z_p and Z:H_p are also shown for reference. Added caution is advisable for using the Z_p values, as these distributions are more sensitive to the prior on ϵ than the upper limits are. Nevertheless, they are reasonable estimates.

Figure 4.2 shows the upper limits Z:H_{max} plotted against planetary mass, along with the prior for Z:H from Eq. 4.8. The prior shows the expected mass-dependence of the metallicity for $f = 1$, going from $\sim 100\times$ solar at Neptune

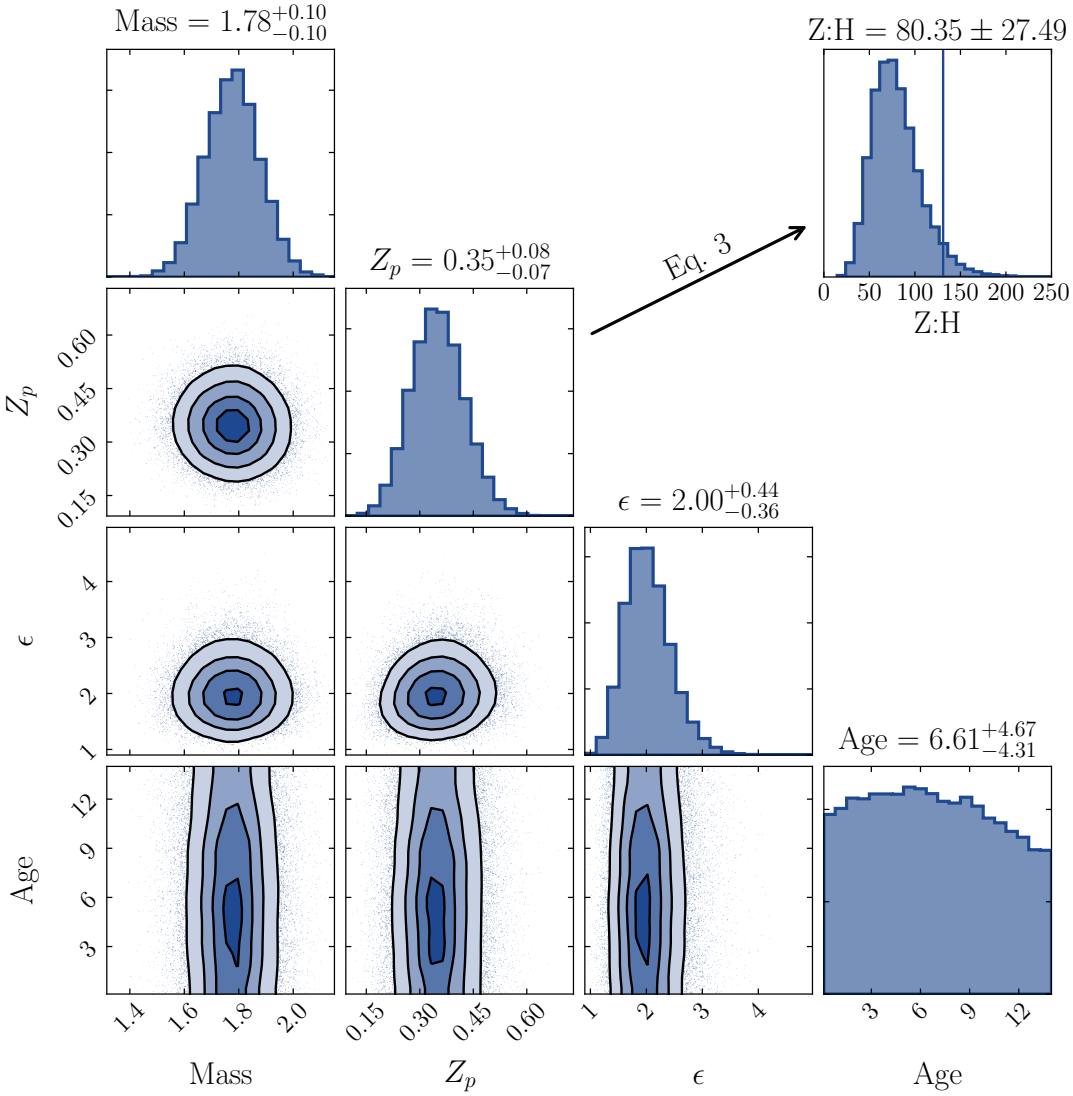

Figure 4.1: A corner plot of the posterior (Eq. 4.15) for WASP-43 b. The parameters are the mass of the planet in Jupiter masses, the bulk metallicity of the planet (metal fraction by mass), the anomalous heating efficiency (the fraction of incident flux deposited in the interior; see Thorngren & Fortney (2018)) in percent, and the age in Gyr. A small degree of Gaussian smoothing was applied to the 2-D histograms to make them clearer. The top right histogram shows the Z:H distribution derived from the Z_p posterior using Equation 4.3, and the upper limit at the 95th percentile (131× solar).

Name	Mass	Radius	Flux	$T_{\rm eq}$	a	e	Period	$Z_{\rm p}$	Z:H	Z:H_{max}
HAT-P-26 b	0.07 ± 0.02	0.63 ± 0.04	0.271	1046	0.0479	0.12	4.2345	0.66 ± 0.03	281.06 ± 39.1	348.5
HD 209458 b	0.73 ± 0.04	1.39 ± 0.02	1.061	1471	0.0475	0.00	3.5247	0.16 ± 0.02	28.07 ± 3.8	34.4
WASP-12 b	1.47 ± 0.07	1.90 ± 0.06	8.933	2505	0.0234	0.05	1.0914	0.09 ± 0.02	13.70 ± 3.8	20.4
WASP-17 b	0.78 ± 0.23	1.87 ± 0.24	1.890	1699	0.0515	0.00	3.7354	0.17 ± 0.07	30.62 ± 19.7	61.4
WASP-39 b	0.28 ± 0.03	1.27 ± 0.04	0.358	1121	0.0486	0.00	4.0553	0.22 ± 0.03	40.51 ± 8.3	54.5
WASP-43 b	1.78 ± 0.10	0.93 ± 0.08	0.821	1379	0.0142	0.00	0.8135	0.35 ± 0.07	80.35 ± 27.5	130.6
WASP-52 b	0.46 ± 0.02	1.27 ± 0.03	0.647	1299	0.0272	0.00	1.7498	0.23 ± 0.02	42.43 ± 4.8	50.6
WASP-107 b	0.12 ± 0.01	0.94 ± 0.02	0.068	740	0.0550	0.00	5.7215	0.24 ± 0.04	46.55 ± 9.3	62.9

Table 4.1: Planetary parameters, orbital parameters, and derived quantities for a selected subset of the planets modeled. $T_{\rm eq}$ is the equilibrium temperature for a zero-albedo planet with full atmospheric redistribution of heat. Z_p is the bulk metal mass fraction of the planet, Z:H is the corresponding atmosphere abundance (eq. 4.3) assuming a fully mixed planet ($f = 1$), and Z:H_{max} is the corresponding upper limit (the 95$^{\rm th}$ percentile of Z:H). Units are M_J, R_J, Gerg s^{-1} cm^{-2}, K, AU, days. The full table contains 403 planets and is available for download in Thorngren & Fortney (2019). Discovery and data sources – HAT-P-26 b: Hartman et al. (2011a); HD 209458 b: Henry et al. (2000), Southworth (2010); WASP-12 b: Hebb et al. (2009), Collins et al. (2017); WASP-17 b: Anderson et al. (2010), Southworth et al. (2012); WASP-39 b: Faedi et al. (2011); WASP-43 b: Hellier et al. (2011), Gillon et al. (2012); WASP-52 b: Hébrard et al. (2013); WASP-107 b: Anderson et al. (2017).

masses to $< 10\times$ solar for brown dwarfs. The 1σ range for the prior is shown as a shaded region; at small masses, Z_p is typically closer to the asymptote in Z:H at $Z_p = 1$ (see Eq. 4.3), leading to larger uncertainties. The upper limits are generally higher than the prior mean, as expected.

For some planets, Z_p was potentially close to one. This typically occurs for low mass planets near the cutoff of $20M_\oplus$, or planets with larger uncertainties in mass or radius. As $Z_p \to 1$, Z:$H \to \infty$, so we cannot provide meaningful upper-limits on Z:H in that range. To reflect this, we have identified the 21 planets whose posterior Z_p has a 99^{th} percentile exceeds 0.9, and removed the upper limit. We chose to strike the entry rather than remove the planet from the table so that readers will at least know that these planets are consistent with very large values of Z:H.

For comparison, we applied our models to Jupiter and Saturn. Since these are not inflated and have tiny mass, radius, and age uncertainties, our methods produce values with negligible error bars. Of course, for these cases, the assumption that observational error dominates modeling uncertainties (discussed in Thorngren et al., 2016) is not valid, but the comparison is still worth making. For Jupiter we obtain $Z_p = .12$ and Z:$H \leq 17.7$; Guillot (1999) compute $.03 \leq Z_p \leq .12$, and the observed atmospheric value is Z:$H \approx 3.5$ (Atreya et al., 2018). For Saturn, we get $Z_p = .291$ and Z:$H \leq 51$; Guillot (1999) compute compute $.21 \leq Z_p \leq .31$, and the observed atmospheric value is Z:$H \approx 10$ (Atreya et al., 2018). In both cases, the metal abundance seen in the atmosphere is about 20% of the value we compute for the bulk (the upper limit). By mass, $f \approx 0.2$ (see §4.2) also. These limits and actual values are shown in Figure 4.2.

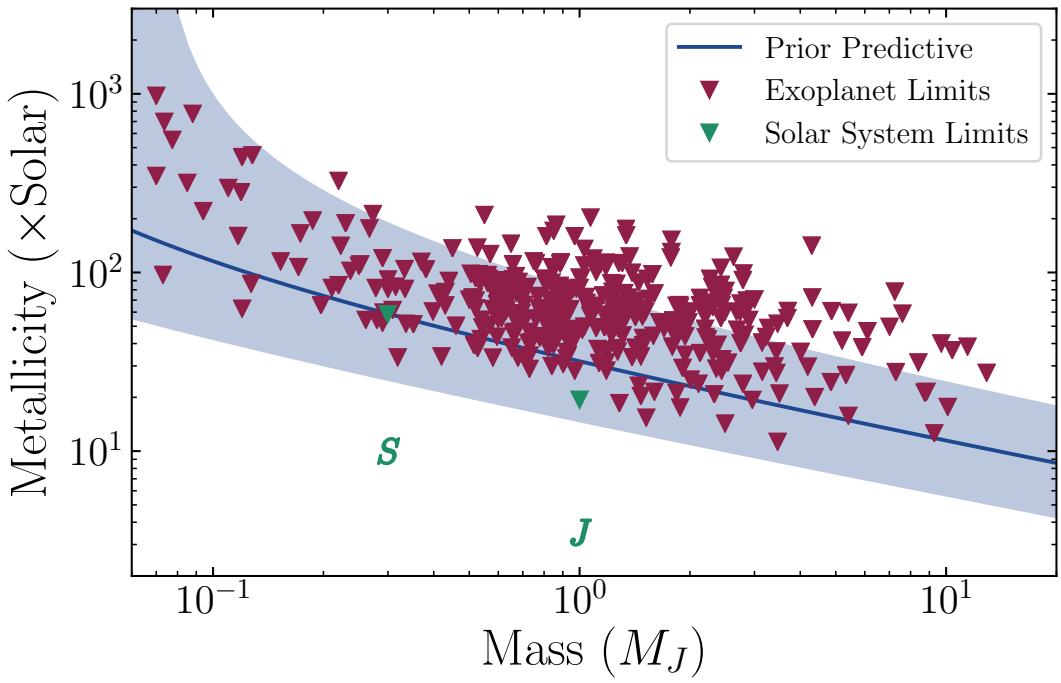

Figure 4.2: The computed upper limits Z:H_{max} for exoplanets, Jupiter, and Saturn, plotted against mass. Also shown is the prior predictive distribution from Eq. 4.8.. The limits are systematically higher than the predictive because they are the 95^{th} percentile of the posterior for each planet. The actual observed atmospheric abundances of Jupiter and Saturn Atreya et al. (2018) are shown as J and S, and are about 20% of the limits we compute.

4.3.2 Fits for Future Discoveries

For new exoplanet discoveries, it would be useful to have a rough estimate of Z:H in advance of running full interior structure models. For this purpose, we have constructed least squares fits of the observed, Z, $\log_{10}(Z{:}H_p)$, $\log_{10}(Z{:}H_{max})$. Due to the complexity of the underlying models, a relatively large number of predictor variables were needed; these were selected by hand with the aim of minimizing the model BIC (Schwarz, 1978) while keeping the number of variables manageable.

The results of these fits were as follows:

$$\begin{aligned}\log_{10}(Z) = &-2.02 - 0.27\log_{10}(M) - 4.75\log_{10}(R) + 0.17\log_{10}(F) + \\ &- 1.27\log_{10}(M)\log_{10}(R) + 0.34\log_{10}(F)\log_{10}(R) \pm 0.1\end{aligned} \tag{4.16}$$

$$\begin{aligned}\log_{10}(Z{:}H) = &-0.16 - 0.35\log_{10}(M) - 9.32\log_{10}(R) + 0.22\log_{10}(F) + \\ &- 1.17\log_{10}(M)\log_{10}(R) + 0.77\log_{10}(F)\log_{10}(R) \pm 0.13\end{aligned} \tag{4.17}$$

$$\begin{aligned}\log_{10}(Z{:}H_{max}) = &1.14 - 0.27\log_{10}(M) - 9.06\log_{10}(R) + 0.19\log_{10}(F) + \\ &- 1.15\log_{10}(M)\log_{10}(R) + 0.72\log_{10}(F)\log_{10}(R) + \\ &1.07\log_{10}(\sigma_R) + 0.3\log_{10}(\sigma_R)^2 \pm 0.11\end{aligned} \tag{4.18}$$

It is important to remember that these are only fits, and so extrapolation is not appropriate; they should only be used for planets with parameters similar to that of our data. Using the 5 to 95$^{\text{th}}$ percentiles, these are $.13 < M < 4.80$ (M_J), $.51 < R < 1.63$ (R_J), $.033 < F < 4.60$ (Gerg s^{-1} cm^{-2}), and $.015 < \sigma_R < .22$ (R_J). The other important caveat is that we have made no attempt to account for observation error, so applying these formulas to planets discovered using methods/telescopes with sensitivities significantly different than the planets we considered may produce a systematic bias. Still, even though they are approximate, these fits provide quick and useful estimates for contextualizing new observations.

4.4 Discussion

We anticipate that these upper limits will provide useful information to atmosphere models. For example, Wakeford et al. (2018) examine WASP-39b and find,

among other results, an atmospheric metallicity of 151^{+48}_{-46} $\times$ solar. Our models find a maximum metallicity of 54.5 $\times$ solar. This tension suggests that the true metallicity is near the bottom of their 2σ range, and that the planet likely has a fairly well mixed interior. It may also point towards favoring their free chemistry model, which found a moderately lower metallicity.

In some cases, the metallicity can exceed our upper limits if the planet interior is hotter than expected by our models. This could occur if the planet is tidally heated, as hypothesized for GJ 436b in Morley et al. (2017), or if the planet is potentially much younger than the models (see discussion in Kreidberg et al., 2018). These potential effects would be minimal in hot Jupiters if the anomalous heating mechanism does not include a delayed cooling component (see Fortney et al., 2010; Spiegel & Burrows, 2013), as these planets must already be supplied with a massive amount of energy and would quickly reach equilibrium.

In the long run as these observations become more numerous and precise, it may be possible to investigate the ratio of the atmosphere metallicity to the bulk metallicity, f. If a certain set of planets consistently exhibit $f \approx 1$ (such as how WASP-39b appears), it suggests that these planets are generally well mixed – they have minimal cores or composition gradients. Cases where f is closer to zero, such as the solar system planets, suggest the converse. These possibilities have been studied theoretically both in the solar system (e.g. Vazan et al., 2016; Moll et al., 2017; Leconte & Chabrier, 2012), and for exoplanets (e.g Vazan et al., 2015; Chabrier & Baraffe, 2007), but observational evidence has been sparse, especially for the latter case. Using interior models in conjunction with atmosphere modeling can provide a new and unique approach to these issues.

5. Main-Sequence Reinflation of Giant Planets

5.1 Introduction

Since the first discovery of a transiting hot Jupiter, HD 209458 b (Charbonneau et al., 2000; Henry et al., 2000), there has been an open question as to why their radii are so large. Without any special physics, giant planets should not have radii much exceeding $\sim 1.2R_J$ (Fortney et al., 2007), even on close orbits. Nevertheless it has become clear that hot Jupiters almost always have inflated radii, extending to as much as twice the radius of Jupiter (e.g. Hartman et al., 2011b). Thus, the race was on to identify the missing physics that could explain this discrepancy.

Many possibilities have since been suggested. (Bodenheimer et al., 2001) note that tidal dissipation, driven by interactions with other planets in the solar system, would deposit significant energy into the planetary interior. (Batygin & Stevenson, 2010) suggest that Ohmic dissipation in the atmosphere could transfer heat downwards, heating the interior and suppressing heat loss. (Arras & Socrates, 2009) propose that tidal forces acting on planets' thermal bulges could deposit heat into the interior. (Chabrier & Baraffe, 2007) and (Burrows et al., 2007) theorize that large composition gradients or additional atmospheric opacity sources

respectively could slow interior cooling to a crawl. Fluid dynamical effects might also allow heat to be pushed from the atmosphere into the interior (e.g. Youdin & Mitchell, 2010; Tremblin et al., 2017). Yet this is still only a sample of the many proposed solutions.

To sort through these theories, we must identify testable differences between them. One valuable piece of evidence is that the radius excess appears to only occur at equilibrium temperatures exceeding 1000 K (Miller & Fortney, 2011; Demory & Seager, 2011). Similarly, these radius anomalies correlate with incident flux much better than semi-major axis (Weiss et al., 2013; Laughlin et al., 2011), disfavoring tidal explanations which would scale against the latter. In Thorngren & Fortney (2018) (Chapter 3), we showed that the extra interior heating as a fraction of flux (fit to match the observed radii) decreases at very high fluxes. This was predicted by the Ohmic dissipation model (see Menou, 2012; Batygin et al., 2011), but may be consistent other models as well. Another test, proposed in Lopez & Fortney (2016), would determine whether hot Jupiters reinflate when their insolation increases by identifying hot Jupiters orbiting red giants, whose insolation greatly increased when their stars went off the main sequence. Whether they would reinflate depends on how deeply the anomalous heat is deposited (Komacek & Youdin, 2017): heating below the radiative-convective boundary allows reinflation, but not above this point. Thus, reinflation would occur under tidal heating mechanisms because these deposit heat relatively deep in the planet, but not for delayed cooling models nor Ohmic dissipation (Ginzburg & Sari, 2016) unless the deposition depth was much deeper than expected. Some such planets have been discovered (Grunblatt et al., 2016, 2017) that seem to point towards reinflation occurring, but the results are not yet conclusive.

Of particular interest to us is a companion path to the Lopez & Fortney (2016)

approach discussed in Hartman et al. (2016), which found a correlation between the radius of hot Jupiters and the fractional age of their parent star (age divided by main sequence lifetime). Their explanation was that as stars age on the main sequence, they brighten; consequently, the flux on the hot Jupiters increases and so their radii grow. They showed that their results were the same for HAT, WASP, and Kepler planets separately as well as for the combined population. However, they did not attempt to control for other observables, such as mass, eccentricity, or stellar mass. This is important to show that it is not simply a byproduct of some other correlation.

For this work, we will further investigate the possibility of main-sequence reinflation of giant planets. First we will study which variables are predictive of the planet radius under a variety of control schemes. Next, we will show that the main-sequence brightening is indeed strong enough to reinflate some planets detectably – and thus that it is a good test of whether reinflation occurs. Finally, we will consider the evidence from hot Jupiters around main-sequence stars that this reinflation actually occurs.

5.2 Mass, Flux, and Radius

To understand how the radius of a hot Jupiter is set, it is worth studying which observables correlate with radius in a comprehensive, model-free manner. To do this, we will compare the Bayesian Information Criterion (BIC) for various linear regressions of the log of the parameters. Specifically we consider simple linear models of the following form:

$$\log(R) \sim \mathcal{N}\left(\beta_0 + \sum_{i=1}^{n} \beta_i \log(x_i), \sigma\right) \tag{5.1}$$

Where $\mathcal{N}$ is the normal distribution, x_i are the observed regressors under consideration, β_i are the regression coefficients, and σ is the residual standard deviation. We use the standard reference priors $p(\beta_0, \sigma) \propto \sigma^{-2}$. This reduces to a power-law relationship for R, but writing it as a linear model lets us use the least-squares regression solution. Because we have such a simple model, the BIC is also available in a closed form. Let n be the number of planets, k the number of regressors (x), and SSD is the sum of squared residuals. Then up to a constant term, the BIC is:

$$\mathrm{BIC} = k \log(n) + n(1 + \log(\mathrm{SSD}/n)) \tag{5.2}$$

We will consider the following regressors: the planet mass M (in M_J), the incident flux on the planet F (in Gerg s^{-1} cm^{-2}), the stellar mass $M_\star$ (in $M_\odot$), the stellar radius $R_\star$ (in $R_\odot$), the system age t (in Gyr), the fractional age t/T (age over main sequence lifetime), the orbital semi-major axis a (in AU), the orbital eccentricity e, stellar luminosity $L_\star$, the stellar zero age main sequence (ZAMS) flux F_{zams} (in Gerg s^{-1} cm^{-2}), and the second order crossterm $\exp(\log(M)\log(F))$. The crossterm was included to allow for the effect seen in structure models where higher mass planets are more difficult to inflate for an equal incident flux (see Thorngren & Fortney, 2018). For t/T, we omit the log in Eq. 5.1 to best reflect the potential relationship, and likewise for e to avoid taking the log of zero.

Using data combined from exoplanet.org (Schneider et al., 2011) and the NASA Exoplanet Archive (Akeson et al., 2013), we considered the 232 hot Jupiters with well determined masses and radii, $F > 2 \times 10^8$ Gerg s^{-1} cm^{-2}, and $M > 0.5 M_J$. We carried out the procedure above for a number of models and regressors; Table 5.1 shows the results. Each row corresponds to a statistical model of the observed radius (on the left) with σ/R as the residual uncertainty as a percent. The remaining columns are the ΔBIC values for adding the regressor indicated by the

Base Model	σ/R	M	F	$M_\star$	$R_\star$	t	t/T	a	e	$L_\star$	F_{zams}	(MF)
1.27	18.40	4.6	-137.9	-79.1	-61.20	5.10	-18.60	2.50	4.40	-90.50	-104.9	3.9
$1.22F^{0.14}$	13.24	-16.8		-6.3	-2.70	5.40	2.30	-8.20	5.30	-8.60	4.8	-19.8
$1.23M^{-0.06}F^{0.15}$	12.61			-7.0	-0.60	4.20	4.30	-7.50	4.40	-7.70	5.3	-11.3
$1.24M^{-0.04}F^{0.17}(MF)^{-0.13}$	12.16			-5.2	2.20	3.80	5.40	-4.30	5.20	-4.60	5.4	
$1.22M^{-0.04}F^{0.14}(MF)^{-0.12}M_\star^{0.19}$	11.90				4.90	5.40	5.00	5.20	5.40	5.00	4.9	
1.23	18.72	4.9	-98.3	-52.20	-56.00	4.90	-10.70	-3.70	2.70	-57.20	-87.90	2.5
$1.21F^{0.14}$	12.55	-6.1		2.00	-0.20	3.80	1.80	0.70	4.80	0.30	2.10	-9.4
$1.23M^{-0.05}F^{0.15}$	12.07			2.20	0.30	4.90	3.20	0.90	4.90	0.70	2.30	-7.4
$1.23M^{-0.04}F^{0.17}(MF)^{-0.12}$	11.56			3.70	3.10	4.80	4.60	2.90	4.70	2.60	2.40	
$1.26F_{zams}^{0.13}$	14.28	-13.1	-28.1	-10.7	-25.20	2.30	-8.80	-10.00	5.40	-30.90		-12.4
$1.28M^{-0.06}F_{zams}^{0.14}$	13.71		-31.3	-10.8	-24.50	4.40	-5.70	-10.10	4.90	-32.40		-5.9

Table 5.1: A table of ΔBICs showing which variables are effective in predicting the radius as we include progressively more variables in a power-law model. Negative numbers indicate that the BIC criterion favors adding the variable to the model. σ/R is the relative predictive uncertainty as a percent. Note that (MF) is the next-order crossterm between M and F, not the product of M and F. The table is divided into three blocks. The top block was calculated for the full set of 232 planets. The middle block was calculated only for planets for whom $F/F_{zams} < 1.25$: the 137 planets which could have reinflated at most only a small amount (about 4% in radius). The bottom block shows all the planets but using F_{zams} instead of the flux.

column head. If a variable is already in the model, its ΔBIC is omitted. More negative numbers are indicate more favored additions to the model – positive numbers indicate it is preferred to leave the variable out.

It is clear from this analysis that flux is the most important variable, followed by the planet mass, and then the crossterm of M and F. After this, several variables are slightly significant at roughly equal levels: $M_\star$, a, and $L_\star$. Including $M_\star$ removes the effect from the other variables. This may indicate that the orbit or stellar parameters matter slightly beyond just setting the flux, but the exact cause is unclear. It is also worth noting that at no point is the system age t a useful predictor; this is inconsistent with delayed cooling models, for which age should predict a reduced radius, even if only modestly.

We see the correlation between fractional age and radius noted by Hartman et al. (2016), and observe that the correlation vanishes when the present-day flux is accounted for. This is consistent with their interpretation that hot Jupiters further reinflate as their parent stars age and brighten. Furthermore, when we only control for the flux predicted for the star at ZAMS, the fractional age remains a useful predictor. This further supports the idea that it is serving as a proxy for the amount of main-sequence brightening (and therefore radius reinflation) that has occurred.

From these results we can also suggest a well-motivated model for the radius given other information. We favor the model $R = 1.23 M^{-.04} F^{.17-.12\log_{10}(M)}$, as this includes all of the significant variables – more detailed models in Table 5.1 are only slightly better and their theoretical grounding is much less clear. If we consider only planets whose brightening $F/F_{zams} < 1.25$ (the center block of Table 5.1), we can see that fitting for this model yields nearly identical results.

5.3 The Effects of Reinflation

Stars brighten as they age on the main sequence. For the more massive planet hosting stars, this can lead a significant change in flux incident on the planet over the course of the star's main sequence lifetime. We are interested in whether planet radii increase in kind with this brightening, or lag behind. Less massive stars increase in luminosity very slowly, and thus represent a natural control group. We can estimate the equilibrium radius R_{eq} of a planet from planets orbiting these stars without having to worry about whether the planet's radius is lagging behind the star's brightening. Then, we construct the simple model for how a planet's radius varies over time, as a function of the reinflation timescale τ_r.

$$R_{eq} = AM^B F^{C+D\log_{10}(M)} \tag{5.3}$$

$$\frac{dR}{dt} = \frac{R - R_{eq}}{\tau} \tag{5.4}$$

$$\tau = \begin{cases} 0.1\text{Gyr} & R > R_{eq} \\ \tau_r & R < R_{eq} \end{cases} \tag{5.5}$$

This model leads to a few cases to consider. First and simplest, if the timescale of reinflation τ_r is fast, then $R \approx R_{eq}$. If the timescale of reinflation is very slow, then once $R < R_{eq}$, the radius becomes essentially constant. For intermediate values of τ_r, the situation is more complex. These will increase slowly in radius as they approach a dynamical equilibrium where $dR/dt = dR_{eq}/dt$, assuming a steadily increasing stellar brightness. However that condition will not always exist long enough for the planet to actually reach dynamical equilibrium. This depends greatly on the rate of stellar brightening, the stellar lifetime, and the reinflation timescale.

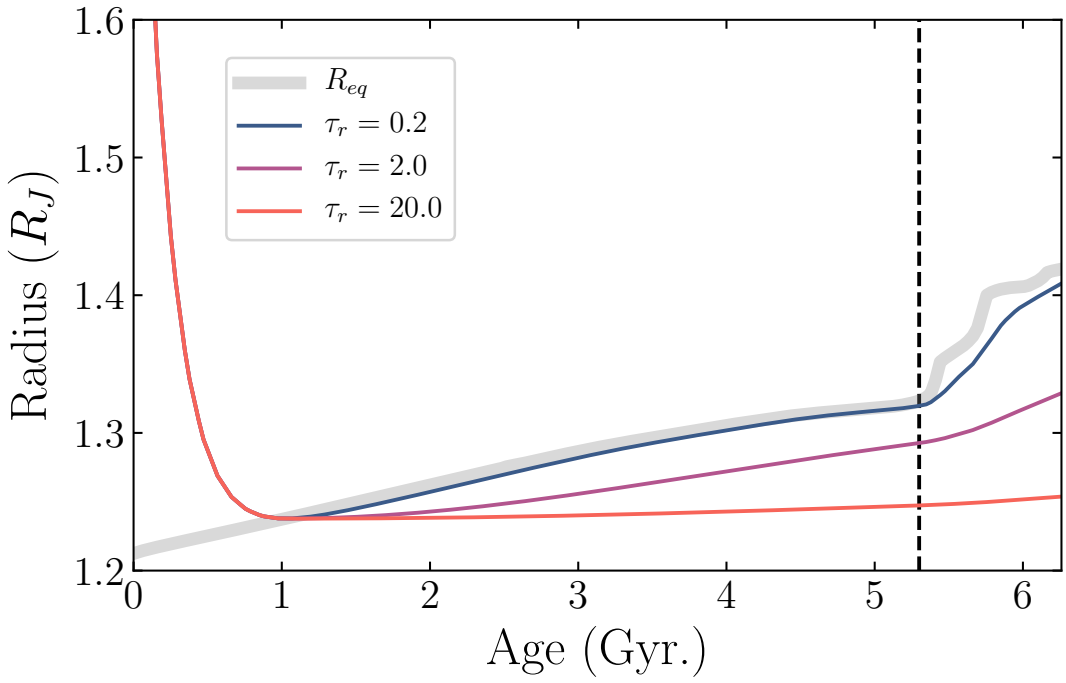

Figure 5.1: Radius evolution for different values of the reinflation timescale τ_r in Gyr. The vertical dotted line is approximately the end of the main sequence; post main-sequence reinflation is apparent as well. The parameters used were based on Kepler-6 b: $M_\star = 1.21 M_\odot$, $M_p = .669 M_J$, $[Fe/H] = .34$, $a = .046$ AU. Stellar evolution tracks are from Dotter (2016); Choi et al. (2016).

Using stellar models (Dotter, 2016; Choi et al., 2016), we can quantify the considerable brightening that stars undergo during their main-sequence lifetime. Their relative luminosity changes are $\sim 2\times$ for $1.5M_\odot$ stars and $\sim 4\times$ for $.5M_\odot$ stars (all at solar metallicity). Of course, the more massive stars experience this brightening much faster, so their relative brightening per unit time is greater. The maximum possible reinflation ($\tau_r = 0$) may be calculated from Eq. 5.3 for $C = .17$ and $M = 1M_J$, and works out to $10 - 30\%$, depending on the stellar mass. This should be readily detectible if τ_r is indeed short.

Figure 5.1 shows example reinflation tracks using several different values of τ_r for the stellar parameters and planet mass of Kepler-6 b. It is clear that significant radius inflation is contingent on the value of τ_r. For reference, Kepler-6 b has $R_p = 1.323 \pm .03\ R_J$ and $t = 3 \pm 1$ Gyr (Dunham et al., 2010), slightly favoring slower timescales. However, our predictions come with a 12% uncertainty, due to e.g. variations in planet composition and observational uncertainties. Thus one planet is not enough to make a determination of the reinflation timescale; instead, we must examine the whole population.

For this, we turn return to the relationship between age and radius noted by (Hartman et al., 2016). Fig. 5.2 shows the radius and residual radius (R/R_{eq} from Eq. 5.3) plotted against the age and fractional age, with correlation measured by the Kendall's Tau statistic and its associated p-value. With high confidence ($p = 1.2 \times 10^{-6}$) we are able to reproduce the correlation that Hartman et al. observed. However, when we correct for the mass and incident flux using the equilibrium radius, the correlation vanishes, as we saw in Table 5.1. Furthermore, we see that neither the radius nor the radius relative to R_{eq} are significantly correlated with the age.

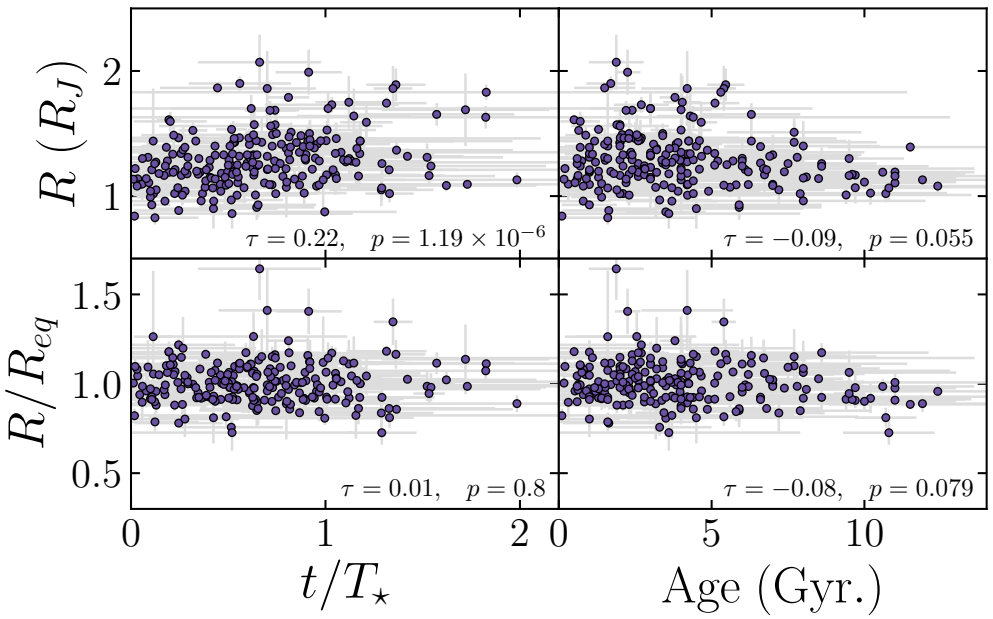

Figure 5.2: Planet radius (top) and the radius relative to the equilibrium radius (bottom, from Eq. 5.3) against age (left) and fractional age (right). To test for correlations, Kendall's tau is shown along with the p-value for non-correlation null hypothesis. A correlation exists between fractional age and radius, but not when flux and mass are corrected for (bottom left), consistent with fast reinflation. No significant correlation with age exists for radius or radius relative to equilibrium, a correlation one would expect under delayed cooling models.

5.4 Conclusions

Our results give strong support to the hypothesis that hot Jupiters can reinflate with their parent stars' main sequence evolution. We have seen that the brightening of these stars, and the reaction of hot Jupiters to changes in flux, is significant enough that the resulting reinflation ($10 - 30\%$) would likely be detectable. We also saw that the difference between plausible reinflation timescales τ_r is enough to significantly alter the radius evolution of the planet (see Fig. 5.1). Thus we conclude that an analysis of main-sequence hot Jupiter evolution can plausibly measure the reinflation timescale.

Furthermore, we have found several points of evidence indicating that this timescale is short. We were able to reproduce the Hartman et al. (2016) result showing a correlation between fractional age and radius. Furthermore, we were able to show that this correlation disappears once the present-day flux is accounted for. If τ_r were long, the original correlation should not exist and our R_{eq} correction should produce an anti-correlation as the star luminosity growth outruns planetary radius inflation. As another check, we showed that correcting with $F_{\rm zams}$ does *not* remove the correlation, showing that subsequent brightening is important. Finally, we found that fitting mass-radius-flux relations produces an essentially identical power-law relationship regardless of whether we include planets with significantly brightened stars. Again, this is only possible if the planetary radii are keeping up with the stellar brightening.

These results therefore firmly rule out delayed cooling models, whether by internal composition gradients (e.g. Chabrier & Baraffe, 2007) or additional atmospheric opacity (Burrows et al., 2007), as these predict no reinflation and radii negatively correlated with age. It also causes problems for the Ohmic dissipation

proposal (Batygin & Stevenson, 2010; Batygin et al., 2011; Menou, 2012), which predict reinflation on a slow, 20 Gyr timescale (Ginzburg & Sari, 2016). This is because its heating is deposited above the RCB, and so it would act to delay cooling much more than directly pumping energy into the interior. Indeed, any similar model which deposits its anomalous heating above the radiative-convective boundary will not produce much reinflation (see Komacek & Youdin, 2017), and is thus disfavored by our results. It is not clear what fluid dynamical solutions like (Tremblin et al., 2017; Youdin & Mitchell, 2010) predict for reinflation; determining this will be a valuable test for these and future proposed explanations.

There remains work to be done in this area. Directly following this work, it should be possible to integrate our reinflation model in the context of a hierarchical model to estimate the actual value of τ_r. To do this accurately, it will be necessary to carefully tie uncertainties in the stellar properties to the luminosity evolution. Additionally, the planets discovered by TESS are expected to include a large number of hot Jupiters (Barclay et al., 2018); these will provide a uniformly-derived sample on which to verify our results. Finally, the study of hot Jupiter hosting red giants proposed in Lopez & Fortney (2016) remains very much worthwhile as it could not only independently confirm our results but could also provide uniquely precise measurements of τ_r. All that would be required is the discovery of more hot Jupiters around red giants (as in Grunblatt et al., 2017), which would be interesting discoveries in their own right.

6. Conclusions

Most of the results of the previous chapters have already been published. In this section, I will review the most important of these results and highlight where they have been applied thus far in the literature.

First, in chapter 2, we inferred the metallicities of a set of observed cool giant planets. We found that the bulk metal content of the planet was positively correlated with the mass of the planet with a power law $M_z = 58M^{.61}$ (fig. 6.1), but not strongly related to the parent star's metallicity. We published these results in Thorngren et al. (2016). Following this work, in Espinoza et al. (2017), we showed that in light of disk C/O ratios (Öberg et al., 2011) these inferred metallicities suggest that the planets considered likely have a lower C/O ratio than their parent stars. In Morley et al. (2017) and Kreidberg et al. (2018), we applied interior models to constrain the atmosphere metallicity of GJ 436 b and WASP-107 b respectively. Our work has also helped to contextualize new planet discoveries (for example, in Petigura et al., 2017; Shporer et al., 2017; Sarkis et al., 2018) and inform models of planet formation (including Mordasini et al., 2016; Humphries & Nayakshin, 2018; Bitsch et al., 2019).

For hot Jupiters, we discussed in chapter 3 our analysis of hot Jupiter inflation power, which was published in Thorngren & Fortney (2018). We found that the inflation power as a fraction of incident stellar flux increases from negligible quantities at $T_{\rm eq} \sim 1000$ K to reach a peak of about 2-3% at around $T_{\rm eq} \sim 1600$

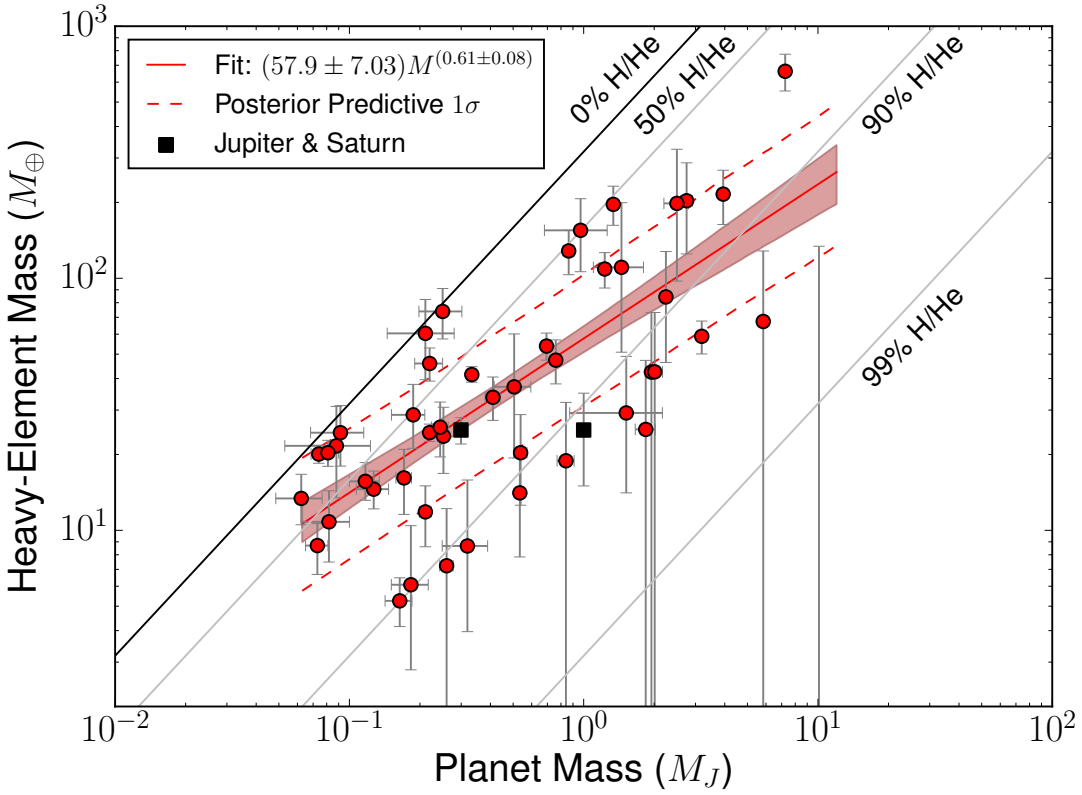

Figure 6.1: The primary results of Chapter 2, showing, the heavy element masses of planets and their masses. The lines of constant $Z_{\rm planet}$ are shown at values of 1 (black), 0.5, 0.1, and .01 (Gray). Distributions for points near $Z_{\rm planet} = 1$ tend to be strongly correlated (have well-defined $Z_{\rm planet}$ values) but may have high mass uncertainties. No models have a $Z_{\rm planet}$ larger than one. The distribution of fits (see §2.4 for discussion) is shown by a red median line with 1 σ shaded region. The dotted line is the 1 σ predictive region. Note Kepler-75b at 10.1 $M_{\rm J}$ which only has an upper limit. This figure is a duplicate of Fig. 2.7.

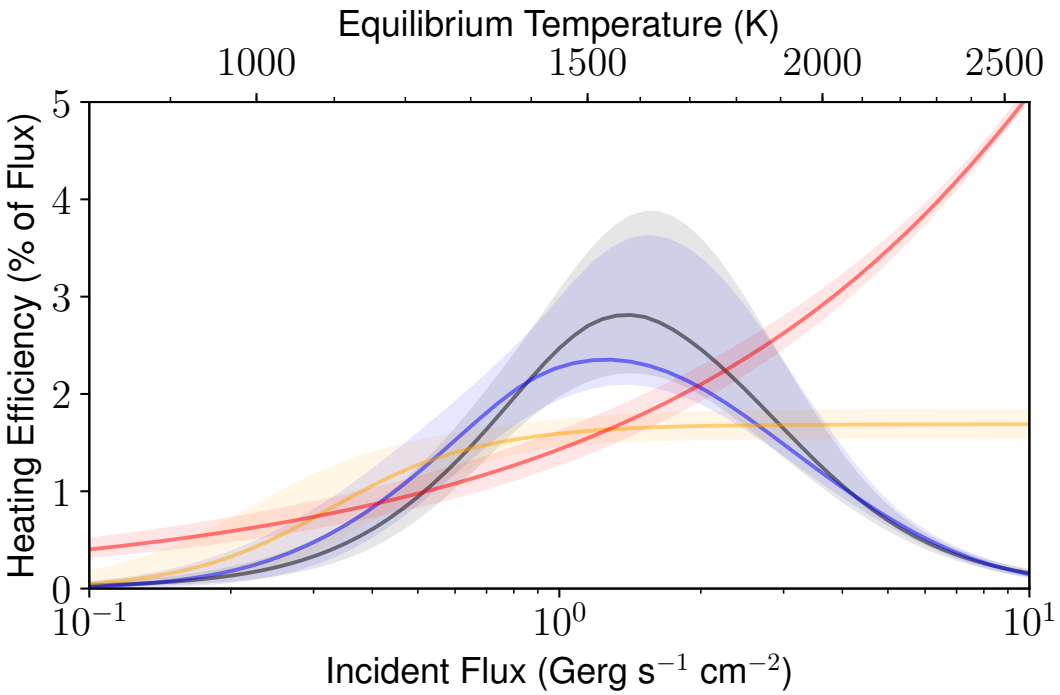

Figure 6.2: The primary results of chapter 3, showing the posteriors of our statistical models of inflation power (as a percent of flux) against incident flux, with 1σ uncertainty bounds. The red line is a power-law model, yellow is logistic, blue is Gaussian, and black is the GP. The Gaussian model is strongly favored over the other parametric models by the DIC model selection criterion, and the GP strongly indicates a negative relationship at high flux. This decrease in inflation efficiency at higher fluxes is important, because it matches predictions from the Ohmic dissipation mechanism of hot Jupiter inflation. This figure is a duplicate of Fig. 3.11.

K, and then declines at higher temperatures (see fig. 6.2). This is an important constraint on the hot Jupiter heating mechanism. These results were naturally quite effective in reproducing the radii of observed giant planets, which led directly into the work in chapter 4. Additionally, in Yadav & Thorngren (2017), we were able to show that by comparing the inferred inflation power with the magnetic scaling laws of Christensen & Aubert (2006), we could estimate the magnetic field strengths of hot Jupiters. These were in the hundreds of Gauss, stronger than previously thought. Additionally, our results were again useful for contextualizing new discoveries (Espinoza et al., 2018; Temple et al., 2019), helping to understand their atmospheres (Carone et al., 2019; Arcangeli et al., 2019) and supporting theoretical models (Adams et al., 2019; Lothringer et al., 2018).

Due to the tremendous importance of spectroscopic studies of planetary atmospheres in exoplanet science, the next reasonable step was to consider how the aforementioned results could be applied to atmospheric studies. In chapter 4, we discussed how bulk metallicities are upper limits in the atmosphere metallicity and used the population trends from chapters 2 and 3 to derive upper limits for a 403 observed giant planets (fig. 6.3). This work will be useful to planet atmosphere studies as in Morley et al. (2017) Kreidberg et al. (2018), but studies directly applying this work have not yet reached publication.

Finally, we examined the possibility of reinflating hot Jupiters as their parent stars brightened. We demonstrated that reinflation is plausible, derived a robust mass-radius-flux relation, and by comparison with the fractional age relationship of (Hartman et al., 2016) argue that it is likely occurring. Unfortunately, we were not able to directly estimate the reinflation timescale, as this will require more precise stellar ages and an improved treatment of stellar luminosity evolution. Nevertheless, this work has important implications for the nature of the hot

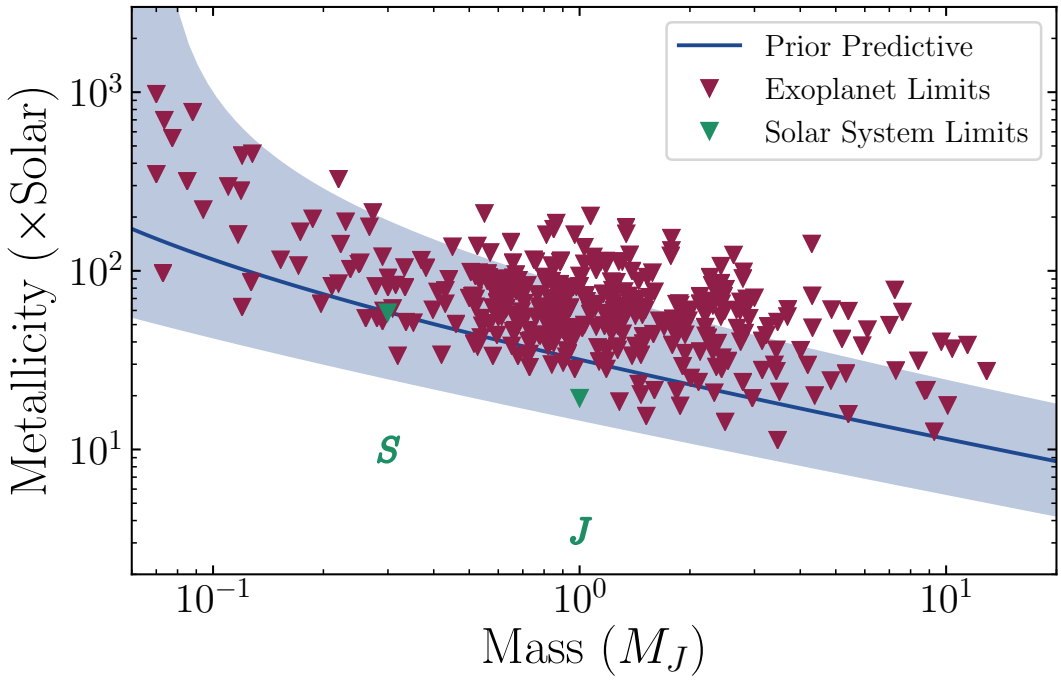

Figure 6.3: The computed upper limits Z:H_{max} for exoplanets, Jupiter, and Saturn, plotted against mass. Also shown is the prior predictive distribution from Eq. 4.8. The limits are systematically higher than the predictive because they are the 95$^{\text{th}}$ percentile of the posterior for each planet. The actual observed atmospheric abundances of Jupiter and Saturn Atreya et al. (2018) are shown as J and S, and are about 20% of the limits we compute. This figure is a duplicate of Fig. 4.2

Jupiter inflation mechanism (see Lopez & Fortney, 2016); for example, disfavoring the Ohmic dissipation model (Batygin et al., 2011; Ginzburg & Sari, 2016) as it is currently understood. This is interesting in light of our results in Chapter 3, which favored Ohmic dissipation for having predicted the flux-heating relationship (Fig. 6.2). There are a few ways to understand this disagreement. For example, Ohmic dissipation may be one part of a larger effect. Alternatively, the flux-heating relation may only indicate that the true heating mechanism strongly relies on upper atmosphere wind speeds (as Ohmic dissipation does, see (Batygin et al., 2011)). Finally, we may simply not understand Ohmic dissipation correctly. Regardless, these results provide valuable tests of hot Jupiter heating models.

6.1 Future Work

There are a number of avenues for future research following this work. A follow-up of the main-sequence reinflation analysis (chapter 5) is perhaps the most obvious. Using a full Bayesian model it should be possible to estimate the reinflation timescale. This will necessitate careful fits to stellar evolution tracks and a well-vetted selection of observed stellar properties; the recent release of GAIA data will help with this. Another way to follow up this work is to identify more post-main-sequence stars hosting giant planets and see whether they are reinflated (as suggested in Lopez & Fortney, 2016). This is a part of ongoing work by others to find such stars (Grunblatt et al., 2016, 2017), and could provide a valuable independent measurement of the reinflation rate. So far, the results have been ambiguous, but new planets in TESS data (Barclay et al., 2018) could improve this.

Another area of interest is the inflation of hot Saturns, whose population exhibits a number of strange properties. I discussed some of these in chapter 3.

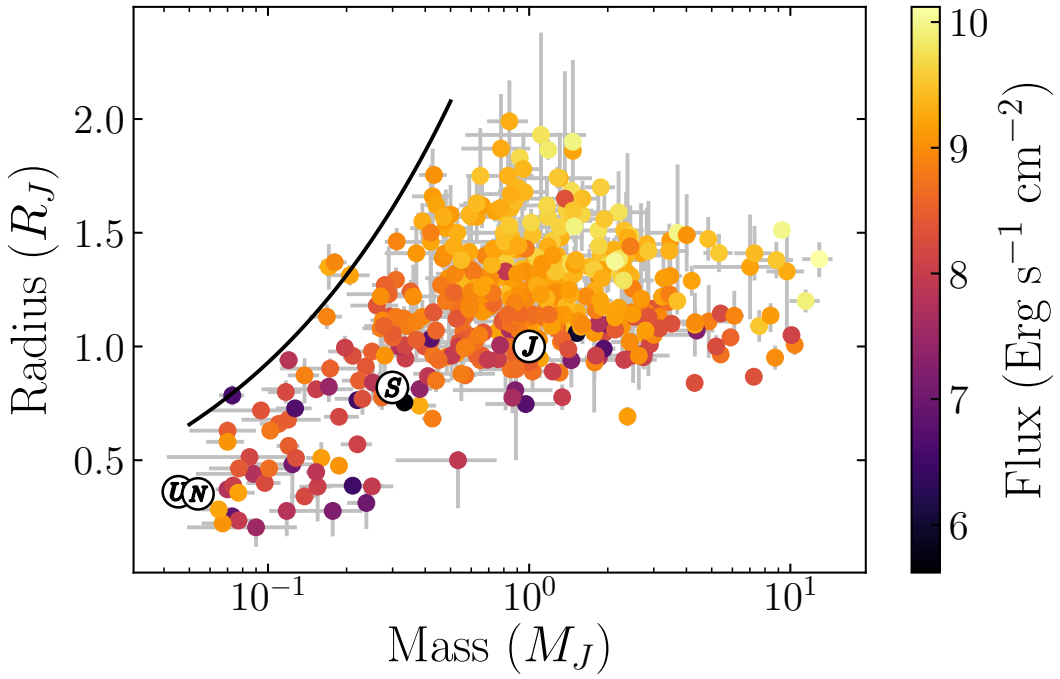

Figure 6.4: Radius plotted against mass, colored by flux of observed giant exoplanets. Jupiter, Saturn, Uranus, and Neptune are also shown. The 3 m/s^2 surface gravity line is shown in black. It seems that giant planets are not found much beyond this limit, even though structure models of such objects are easy to inflate.

These objects do not seem to occur with surface gravities much beyond 3 m/s^2 (Fig. 6.4), even though the required radii are perfectly feasible from an interior structure point of view. This effect appears to become important at about $0.5M_J$, and in fact, giant planets appear much more common just above this mass than just below. Finally, the clear correlation between radius and incident flux seen with hot Jupiters is far messier for hot Saturns. For example, KELT-11 b (Pepper et al., 2017) and HAT-P-47 b (Bakos et al., 2016) are clearly inflated, yet K2-108 b (Petigura et al., 2017) and Kepler-101 b (Bonomo et al., 2014) aren't, even though their masses and fluxes are similar. HD 149026 b is a particularly extreme case (Fortney et al., 2006), having a radius of $.72R_J$ in spite of being highly insolated (Sato et al., 2005). This problem is somewhat overlapping with the sub-Jupiter desert issue described in Szabó & Kiss (2011), for which Owen & Murray-Clay (2018) propose that mass-loss during high-eccentricity migration is the cause. This process may well occur, but it seems unlikely that *all* hot Saturns undergo high-eccentricity migration (see Dawson & Murray-Clay, 2013), and this does not alone explain strange cases like HD 149026 b. As such, further work is needed.

One final area of interest to mention here concerns the effects of semi-convective regions. The work outlined here has so far considered only structures that contain either one fully-convective layer or a conductive core underneath a convective envelope. In reality, there may be a gradual transition from core to envelope (see section 1.4.4). This has already been the subject of a number of studies (Leconte & Chabrier, 2012; Vazan et al., 2015, 2016, e.g.). In particular, Moll et al. (2017) showed that the rate at which the core can dissolve in Jupiter is related to the heat flux out of the core. This needs to be studied for other planet masses, but perhaps more interesting is the effect that core heating from radioactive decays or tidal dissipation might have. These additional power sources could disrupt semi-

convective regions and lead to more efficient core erosion. The resulting planets would be better mixed, which could potentially be observable in comparing bulk and atmosphere metallicities among many planets – see chapter 4.

The potential research outlined here represents only the most immediate logical next steps. The overall strategy of combining detailed physical modelling with population-level statistics is widely applicable in exoplanet science, and will only become more important as more planets are discovered and further characterized.

Bibliography

Adams, D., Gao, P., de Pater, I., & Morley, C. V. 2019, The Astrophysical Journal, 874, 61

Akaike, H. 1974, IEEE Transactions on Automatic Control, 19, 716

Akeson, R. L., Chen, X., Ciardi, D., et al. 2013, Publications of the Astronomical Society of the Pacific, 125, 989

Alibert, Y., Mousis, O., Mordasini, C., & Benz, W. 2005, The Astrophysical Journal Letters, 626, L57

Anderson, D. R., Hellier, C., Gillon, M., et al. 2010, ApJ, 709, 159

Anderson, D. R., Collier Cameron, A., Delrez, L., et al. 2014, Monthly Notices of the Royal Astronomical Society, 445, 1114

Anderson, D. R., Cameron, A. C., Delrez, L., et al. 2017, A&A, 604, A110

Arcangeli, J., Desert, J.-M., Parmentier, V., et al. 2019, arXiv:1904.02069 [astro-ph], arXiv:1904.02069

Armitage, P. J. 2011, Annual Review of Astronomy and Astrophysics, 49, 195

Arras, P., & Socrates, A. 2009, ArXiv e-prints, 0901, arXiv:0901.0735

Asplund, M., Grevesse, N., Sauval, A. J., & Scott, P. 2009, Annual Review of Astronomy and Astrophysics, 47, 481

Atreya, S. K., Crida, A., Guillot, T., et al. 2018, in Saturn in the 21st Century, ed. K. H. Baines, F. M. Flasar, N. Krupp, & T. Stallard, Cambridge Planetary Science (Cambridge University Press), 5–43

Auvergne, M., Bodin, P., Boisnard, L., et al. 2009, Astronomy and Astrophysics, 506, 411

Bai, X.-N. 2016, The Astrophysical Journal, 821, 80

Baker, R. D., & Schubert, G. 1998, Icarus, 136, 340

Bakos, G. Á., Torres, G., Pál, A., et al. 2010, ApJ, 710, 1724

Bakos, G. Á., Hartman, J., Torres, G., et al. 2011, ApJ, 742, 116

Bakos, G. Á., Hartman, J. D., Bhatti, W., et al. 2015, AJ, 149, 149

Bakos, G. Á., Hartman, J. D., Torres, G., et al. 2016, arXiv:1606.04556 [astro-ph], arXiv:1606.04556

Baraffe, I., Chabrier, G., & Barman, T. 2008, Astronomy and Astrophysics, 482, 315

Baraffe, I., Chabrier, G., Barman, T. S., Allard, F., & Hauschildt, P. H. 2003, Astronomy and Astrophysics, 402, 701

Baraffe, I., Chabrier, G., Fortney, J., & Sotin, C. 2014, Protostars and Planets VI, 763

Baraffe, I., Selsis, F., Chabrier, G., et al. 2004, A&A, 419, L13

Barclay, T., Pepper, J., & Quintana, E. V. 2018, The Astrophysical Journal Supplement Series, 239, 2

Barman, T. S., Konopacky, Q. M., Macintosh, B., & Marois, C. 2015, The Astrophysical Journal, 804, 61

Batista, V. 2018, in Handbook of Exoplanets, ed. H. J. Deeg & J. A. Belmonte (Cham: Springer International Publishing), 659–687

Batygin, K., & Stevenson, D. J. 2010, ApJL, 714, L238

Batygin, K., Stevenson, D. J., & Bodenheimer, P. H. 2011, The Astrophysical Journal, 738, 1

Bean, J. L., Benedict, G. F., & Endl, M. 2006, ApJ, 653, L65

Bean, J. L., Stevenson, K. B., Batalha, N. M., et al. 2018, Publications of the Astronomical Society of the Pacific, 130, 114402

Beaulieu, J.-P., Bennett, D. P., Fouqué, P., et al. 2006, Nature, 439, 437

Becker, J. C., Vanderburg, A., Adams, F. C., Rappaport, S. A., & Schwengeler, H. M. 2015, The Astrophysical Journal Letters, 812, L18

Beichman, C., Benneke, B., Knutson, H., et al. 2014, Publications of the Astronomical Society of the Pacific, 126, 1134

Belton, M. J. S., Head, III, J. W., Ingersoll, A. P., et al. 1996, Science, 274, 377

Benneke, B., & Seager, S. 2012, The Astrophysical Journal, 753, 100

Bitsch, B., Izidoro, A., Johansen, A., et al. 2019, A&A, 623, A88

Bodenheimer, P., Lin, D. N. C., & Mardling, R. A. 2001, The Astrophysical Journal, 548, 466

Boehler, R. 1993, Nature, 363, 534

Bolton, S. J., Adriani, A., Adumitroaie, V., et al. 2017, Science, 356, 821

Bonomo, A. S., Santerne, A., Alonso, R., et al. 2010, A&A, 520, A65

Bonomo, A. S., Sozzetti, A., Lovis, C., et al. 2014, A&A, 572, A2

Bonomo, A. S., Sozzetti, A., Santerne, A., et al. 2015, A&A, 575, A85

Bordé, P., Bouchy, F., Deleuil, M., et al. 2010, A&A, 520, A66

Borucki, W. J., Koch, D., Basri, G., et al. 2010, Science, 327, 977

Brahm, R., Jordán, A., Bakos, G. Á., et al. 2016, The Astronomical Journal, 151, 89

Bruno, G., Almenara, J.-M., Barros, S. C. C., et al. 2015, A&A, 573, A124

Burrows, A., Budaj, J., & Hubeny, I. 2008, The Astrophysical Journal, 678, 1436

Burrows, A., Hubeny, I., Budaj, J., & Hubbard, W. B. 2007, The Astrophysical Journal, 661, 502

Cabrera, J., Bruntt, H., Ollivier, M., et al. 2010, Astronomy and Astrophysics, 522, A110

Campbell, J. K., & Synnott, S. P. 1985, The Astronomical Journal, 90, 364

Carone, L., Baeyens, R., Mollière, P., et al. 2019, arXiv e-prints, arXiv:1904.13334

Chabrier, G., & Baraffe, I. 2007, The Astrophysical Journal Letters, 661, L81

Chabrier, G., Johansen, A., Janson, M., & Rafikov, R. 2014, Protostars and Planets VI, 619

Chabrier, G., Mazevet, S., & Soubiran, F. 2019, The Astrophysical Journal, 872, 51

Chabrier, G., Saumon, D., Hubbard, W. B., & Lunine, J. I. 1992, The Astrophysical Journal, 391, 817

Chandrasekhar, S. 1939, An Introduction to the Study of Stellar Structure (Chicago, Ill.: University of Chicago Press)

Charbonneau, D., Brown, T. M., Latham, D. W., & Mayor, M. 2000, The Astrophysical Journal Letters, 529, L45

Charbonneau, D., Berta, Z. K., Irwin, J., et al. 2009, Nature, 462, 891

Choi, J., Dotter, A., Conroy, C., et al. 2016, The Astrophysical Journal, 823, 102

Christensen, U. R., & Aubert, J. 2006, Geophysical Journal International, 166, 97

Collins, K. A., Kielkopf, J. F., & Stassun, K. G. 2017, The Astronomical Journal, 153, 78

Conrath, B. J., & Gautier, D. 2000, Icarus, 144, 124

Crida, A., Morbidelli, A., & Masset, F. 2006, Icarus, 181, 587

Cumming, A. 2010, in Exoplanets (University of Arizona Press), 191–214

Cumming, A., Helled, R., & Venturini, J. 2018, Monthly Notices of the Royal Astronomical Society, 477, 4817

Dawson, R. I., & Murray-Clay, R. A. 2013, The Astrophysical Journal Letters, 767, L24

Dawson, R. I., Johnson, J. A., Fabrycky, D. C., et al. 2014, ApJ, 791, 89

Debras, F., & Chabrier, G. 2019, arXiv:1901.05697 [astro-ph], arXiv:1901.05697

Deeg, H. J., & Alonso, R. 2018, in Handbook of Exoplanets, ed. H. J. Deeg & J. A. Belmonte (Cham: Springer International Publishing), 633–657

Deeg, H. J., Moutou, C., Erikson, A., et al. 2010, Nature, 464, 384

Demarcus, W. C. 1958, The Astronomical Journal, 63, 2

Deming, D., Harrington, J., Laughlin, G., et al. 2007, The Astrophysical Journal Letters, 667, L199

Demory, B.-O., & Seager, S. 2011, ApJS, 197, 12

Dotter, A. 2016, The Astrophysical Journal Supplement Series, 222, 8

Doyle, L. R., Carter, J. A., Fabrycky, D. C., et al. 2011, Science, 333, 1602

Dressing, C. D., & Charbonneau, D. 2013, The Astrophysical Journal, 767, 95

Duffell, P. C., & Dong, R. 2015, The Astrophysical Journal, 802, 42

Dunham, E. W., Borucki, W. J., Koch, D. G., et al. 2010, The Astrophysical Journal Letters, 713, L136

Eremets, M. I., & Troyan, I. A. 2011, Nature Materials, 10, 927

Espinoza, N., Fortney, J. J., Miguel, Y., Thorngren, D., & Murray-Clay, R. 2017, The Astrophysical Journal Letters, 838, L9

Espinoza, N., Hartman, J. D., Bakos, G. Á., et al. 2018, arXiv e-prints, arXiv:1812.07668

Evans, T. M., Sing, D. K., Wakeford, H. R., et al. 2016, The Astrophysical Journal Letters, 822, L4

Eylen, V. V., Nowak, G., Albrecht, S., et al. 2016, ApJ, 820, 56

Faedi, F., Barros, S. C. C., Anderson, D. R., et al. 2011, A&A, 531, A40

Fei, Y., Mao, H.-K., & Mysen, B. O. 1991, Journal of Geophysical Research, 96, 2157

Fischer, D. A., & Valenti, J. 2005, The Astrophysical Journal, 622, 1102

Fisher, C., & Heng, K. 2018, Monthly Notices of the Royal Astronomical Society, 481, 4698

Fletcher, L. N., Orton, G. S., Teanby, N. A., Irwin, P. G. J., & Bjoraker, G. L. 2009, Icarus, 199, 351

Ford, E. B., Fabrycky, D. C., Steffen, J. H., et al. 2012, ApJ, 750, 113

Foreman-Mackey, D. 2016, The Journal of Open Source Software, 24, doi:10.21105/joss.00024

Foreman-Mackey, D., Hogg, D. W., Lang, D., & Goodman, J. 2013, Publications of the Astronomical Society of the Pacific, 125, 306

Fortney, J. J. 2005, Monthly Notices of the Royal Astronomical Society, 364, 649

Fortney, J. J., Baraffe, I., & Militzer, B. 2010, in Exoplanets (Tuscon, Arizona: University of Arizona Press), 397–418

Fortney, J. J., Lodders, K., Marley, M. S., & Freedman, R. S. 2008, The Astrophysical Journal, 678, 1419

Fortney, J. J., Marley, M. S., & Barnes, J. W. 2007, The Astrophysical Journal, 659, 1661

Fortney, J. J., Mordasini, C., Nettelmann, N., et al. 2013, ApJ, 775, 80

Fortney, J. J., Saumon, D., Marley, M. S., Lodders, K., & Freedman, R. S. 2006, ApJ, 642, 495

French, M., Becker, A., Lorenzen, W., et al. 2012, The Astrophysical Journal Supplement Series, 202, 5

French, M., Mattsson, T. R., Nettelmann, N., & Redmer, R. 2009, Phys. Rev. B, 79, 054107

Fressin, F., Torres, G., Charbonneau, D., et al. 2013, The Astrophysical Journal, 766, 81

Fulton, B. J., Petigura, E. A., Howard, A. W., et al. 2017, The Astronomical Journal, 154, 109

Fung, J., Shi, J.-M., & Chiang, E. 2014, The Astrophysical Journal, 782, 88

Galle, J. G. 1846, Monthly Notices of the Royal Astronomical Society, 7, 153

Gardner, J. P., Mather, J. C., Clampin, M., et al. 2006, Space Science Reviews, 123, 485

Gaudi, B. S., Stassun, K. G., Collins, K. A., et al. 2017, Nature, 546, 514

Gelman, A., Carlin, J. B., Stern, H. S., et al. 2014a, Bayesian Data Analysis, third edition edn., Texts in Statistical Science Series (Boca Raton London New York: CRC Press, Taylor and Francis Group), oCLC: 864304245

Gelman, A., Hwang, J., & Vehtari, A. 2014b, Stat Comput, 24, 997

Gelman, A., & Rubin, D. B. 1992, Statist. Sci., 7, 457

Gibson, N. P., Aigrain, S., Pont, F., et al. 2012, Monthly Notices of the Royal Astronomical Society, 422, 753

Gillon, M., Triaud, A. H. M. J., Fortney, J. J., et al. 2012, Astronomy & Astrophysics, 542, A4

Ginzburg, S., & Sari, R. 2016, The Astrophysical Journal, 819, 116

González-Cataldo, F., Wilson, H. F., & Militzer, B. 2014, The Astrophysical Journal, 787, 79

Griffith, C. A. 2014, Phil. Trans. R. Soc. A, 372, 20130086

Griffiths, D. J. 2017, Introduction to Quantum Mechanics, second edition edn. (Cambridge: Cambridge University Press)

Grunblatt, S. K., Huber, D., Gaidos, E. J., et al. 2016, The Astronomical Journal, 152, 185

Grunblatt, S. K., Huber, D., Gaidos, E., et al. 2017, The Astronomical Journal, 154, 254

Guillot, T. 1999, Planetary and Space Science, 47, 1183

—. 2010, Astronomy and Astrophysics, 520, A27

Guillot, T., & Gautier, D. 2014, arXiv e-prints, 1405, arXiv:1405.3752

Guillot, T., & Havel, M. 2009, in AAS/Division for Planetary Sciences Meeting Abstracts #41, Vol. 41, 8.04

Guillot, T., Santos, N. C., Pont, F., et al. 2006, Astronomy and Astrophysics, 453, L21

Guillot, T., & Showman, A. P. 2002, Astronomy and Astrophysics, 385, 156

Guillot, T., Stevenson, D. J., Hubbard, W. B., & Saumon, D. 2004, in Jupiter. The Planet, Satellites and Magnetosphere (Cambridge University Press), 35–57

Hadden, S., & Lithwick, Y. 2017, The Astronomical Journal, 154, 5

Hartman, J. D., Bakos, G. Á., Kipping, D. M., et al. 2011a, The Astrophysical Journal, 728, 138

Hartman, J. D., Bakos, G. Á., Torres, G., et al. 2011b, The Astrophysical Journal, 742, 59

Hartman, J. D., Bayliss, D., Brahm, R., et al. 2015, AJ, 149, 166

Hartman, J. D., Bakos, G. Á., Bhatti, W., et al. 2016, The Astronomical Journal, 152, 182

Hastings, W. K. 1970, Biometrika, 57, 97

Hayashi, C. 1981, Progress of Theoretical Physics Supplement, 70, 35

Hebb, L., Collier-Cameron, A., Loeillet, B., et al. 2009, ApJ, 693, 1920

Hébrard, G., Cameron, A. C., Brown, D. J. A., et al. 2013, A&A, 549, A134

Helled, R. 2018, arXiv:1812.07436 [astro-ph], 1, arXiv:1812.07436

Helled, R., & Bodenheimer, P. 2014, ArXiv:1404.5018, arXiv:1404.5018

Hellier, C., Anderson, D. R., Collier Cameron, A., et al. 2010, ApJ, 723, L60

—. 2011, Astronomy and Astrophysics, 535, L7

Hellier, C., Anderson, D. R., Cameron, A. C., et al. 2017, Monthly Notices of the Royal Astronomical Society, 465, 3693

Heng, K. 2018, Research Notes of the American Astronomical Society, 2, 128

Heng, K., & Kitzmann, D. 2017, Monthly Notices of the Royal Astronomical Society, 470, 2972

Henry, G. W., Marcy, G. W., Butler, R. P., & Vogt, S. S. 2000, The Astrophysical Journal Letters, 529, L41

Herschel, F. 1781, Philosophical Transactions of the Royal Society of London, 71, 492

Hicks, D. G., Boehly, T. R., Celliers, P. M., et al. 2009, Physical Review B, 79, 014112

Hirano, T., Narita, N., Sato, B., et al. 2012, ApJ, 759, L36

Holman, M. J., Fabrycky, D. C., Ragozzine, D., et al. 2010, Science, 330, 51

Howard, A. W., Marcy, G. W., Johnson, J. A., et al. 2010, Science, 330, 653

Howard, A. W., Bakos, G. Á., Hartman, J., et al. 2012, ApJ, 749, 134

Howell, S. B., Sobeck, C., Haas, M., et al. 2014, Publications of the Astronomical Society of the Pacific, 126, 398

Huang, C. X., Burt, J., Vanderburg, A., et al. 2018, The Astrophysical Journal Letters, 868, L39

Hubbard, W. B. 1968, The Astrophysical Journal, 152, 745

—. 2012, The Astrophysical Journal Letters, 756, L15

Hubbard, W. B., Burrows, A., & Lunine, J. I. 2002, Annu. Rev. Astron. Astrophys., 40, 103

Hubbard, W. B., Hattori, M. F., Burrows, A., Hubeny, I., & Sudarsky, D. 2007, Icarus, 187, 358

Hubbard, W. B., & Marley, M. S. 1989, Icarus, 78, 102

Hubbard, W. B., & Militzer, B. 2016, The Astrophysical Journal, 820, 80

Humphries, R. J., & Nayakshin, S. 2018, Monthly Notices of the Royal Astronomical Society, 477, 593

Ida, S., & Lin, D. N. C. 2004, The Astrophysical Journal, 604, 388

Iess, L., Folkner, W. M., Durante, D., et al. 2018, Nature, 555, 220

Jeffreys, H. 1935, Mathematical Proceedings of the Cambridge Philosophical Society, 31, 203

—. 1946, Proceedings of the Royal Society of London Series A, 186, 453

Johnson, J. A., Aller, K. M., Howard, A. W., & Crepp, J. R. 2010, Publications of the Astronomical Society of the Pacific, 122, 905

Johnson, J. A., Gazak, J. Z., Apps, K., et al. 2012, The Astronomical Journal, 143, 111

Jontof-Hutter, D., Ford, E. B., Rowe, J. F., et al. 2016, The Astrophysical Journal, 820, 39

Kass, R. E., & Raftery, A. E. 1995, Journal of the American Statistical Association, 90, 773

Kippenhahn, R., Weigert, A., & Weiss, A. 2012, Stellar Structure and Evolution, Astronomy and Astrophysics Library (Berlin, Heidelberg: Springer Berlin Heidelberg), doi:10.1007/978-3-642-30304-3

Klahr, H., & Bodenheimer, P. 2006, The Astrophysical Journal, 639, 432

Knutson, H. A., Charbonneau, D., Allen, L. E., Burrows, A., & Megeath, S. T. 2008, The Astrophysical Journal, 673, 526

Komacek, T. D., & Youdin, A. N. 2017, The Astrophysical Journal, 844, 94

Konacki, M., Torres, G., Jha, S., & Sasselov, D. D. 2003, Nature, 421, 507

Konopacky, Q. M., Barman, T. S., Macintosh, B. A., & Marois, C. 2013, Science, 339, 1398

Kostov, V. B., McCullough, P. R., Carter, J. A., et al. 2014, ApJ, 784, 14

Kostov, V. B., Orosz, J. A., Welsh, W. F., et al. 2016, The Astrophysical Journal, 827, 86

Kovács, G., Bakos, G. Á., Hartman, J. D., et al. 2010, ApJ, 724, 866

Kratter, K. M., Matzner, C. D., Krumholz, M. R., & Klein, R. I. 2010, The Astrophysical Journal, 708, 1585

Kreidberg, L., Line, M. R., Thorngren, D., Morley, C. V., & Stevenson, K. B. 2018, The Astrophysical Journal Letters, 858, L6

Kreidberg, L., Bean, J. L., Désert, J.-M., et al. 2014a, Nature, 505, 69

—. 2014b, ApJL, 793, L27

Kurokawa, H., & Inutsuka, S.-i. 2015, The Astrophysical Journal, 815, 78

Lagrange, A.-M., Gratadour, D., Chauvin, G., et al. 2009, Astronomy and Astrophysics, 493, L21

Laughlin, G., Crismani, M., & Adams, F. C. 2011, The Astrophysical Journal Letters, 729, L7

Leconte, J., Baraffe, I., Chabrier, G., Barman, T., & Levrard, B. 2009, Astronomy and Astrophysics, 506, 385

Leconte, J., & Chabrier, G. 2012, A&A, 540, A20

Leconte, J., Chabrier, G., Baraffe, I., & Levrard, B. 2010, A&A, 516, A64

Leconte, J., Chabrier, G., Baraffe, I., & Levrard, B. 2011, in European Physical Journal Web of Conferences, Vol. 11, eprint: arXiv:1011.0336, 03004

Ledoux, P. 1947, The Astrophysical Journal, 105, 305

Li, C., Ingersoll, A., Janssen, M., et al. 2017, Geophysical Research Letters, 44, 5317

Lin, D. N. C., & Papaloizou, J. C. B. 1993, in Protostars and Planets III, 749–835

Line, M. R., Knutson, H., Wolf, A. S., & Yung, Y. L. 2014, The Astrophysical Journal, 783, 70

Line, M. R., & Parmentier, V. 2016, The Astrophysical Journal, 820, 78

Lissauer, J. J. 1993, Annual Review of Astronomy and Astrophysics, 31, 129

Lissauer, J. J., Hubickyj, O., D'Angelo, G., & Bodenheimer, P. 2009, Icarus, 199, 338

Lodders, K. 2009, ArXiv:0910.0811, arXiv:0910.0811

Lopez, E. D., & Fortney, J. J. 2014, The Astrophysical Journal, 792, 1

—. 2016, The Astrophysical Journal, 818, 4

Lopez, E. D., Fortney, J. J., & Miller, N. 2012, The Astrophysical Journal, 761, 59

Lothringer, J. D., Barman, T., & Koskinen, T. 2018, The Astrophysical Journal, 866, 27

Loubeyre, P., Brygoo, S., Eggert, J., et al. 2012, Phys. Rev. B, 86, 144115

Lovis, C., & Fischer, D. 2010, in Exoplanets (University of Arizona Press), 27–53

Low, F. J. 1966, The Astronomical Journal, 71, 391

Lozovsky, M., Helled, R., Rosenberg, E. D., & Bodenheimer, P. 2017, ApJ, 836, 227

Lyon, S. P., & Johnson, J. D. 1992, SESAME: The Los Alamos National Laboratory Equation of State Database., Tech. Rep. LA-UR-92-3407, Los Alamos National Laboratory

Madhusudhan, N., Knutson, H., Fortney, J. J., & Barman, T. 2014, Protostars and Planets VI, 739

Madhusudhan, N., Mousis, O., Johnson, T. V., & Lunine, J. I. 2011, The Astrophysical Journal, 743, 191

Mancini, L., Lillo-Box, J., Southworth, J., et al. 2016, A&A, 590, A112

Mandell, A. M., Haynes, K., Sinukoff, E., et al. 2013, The Astrophysical Journal, 779, 128

Mankovich, C., Fortney, J. J., & Moore, K. L. 2016, The Astrophysical Journal, 832, 113

Marley, M. S., Fortney, J. J., Hubickyj, O., Bodenheimer, P., & Lissauer, J. J. 2007, ApJ, 655, 541

Marois, C., Macintosh, B., Barman, T., et al. 2008, Science, 322, 1348

Masuda, K., Hirano, T., Taruya, A., Nagasawa, M., & Suto, Y. 2013, ApJ, 778, 185

Mayor, M., & Queloz, D. 1995, Nature, 378, 355

Mazzola, G., Helled, R., & Sorella, S. 2018, Physical Review Letters, 120, 025701

Menou, K. 2012, The Astrophysical Journal, 745, 138

Miguel, Y., Guillot, T., & Fayon, L. 2016, Astronomy and Astrophysics, 596, A114

Militzer, B., & Hubbard, W. B. 2013, The Astrophysical Journal, 774, 148

Miller, N., & Fortney, J. J. 2011, The Astrophysical Journal Letters, 736, L29

Miller, N., Fortney, J. J., & Jackson, B. 2009, ApJ, 702, 1413

Moll, R., Garaud, P., Mankovich, C., & Fortney, J. J. 2017, The Astrophysical Journal, 849, 24

Mordasini, C., Alibert, Y., Benz, W., Klahr, H., & Henning, T. 2012, Astronomy and Astrophysics, 541, A97

Mordasini, C., Klahr, H., Alibert, Y., Miller, N., & Henning, T. 2014, A&A, 566, A141

Mordasini, C., van Boekel, R., Mollière, P., Henning, T., & Benneke, B. 2016, The Astrophysical Journal, 832, 41

Morley, C. V., Fortney, J. J., Kempton, E. M.-R., et al. 2013, The Astrophysical Journal, 775, 33

Morley, C. V., Knutson, H., Line, M., et al. 2017, The Astronomical Journal, 153, 86

Mousis, O., Marboeuf, U., Lunine, J. I., et al. 2009, The Astrophysical Journal, 696, 1348

Naef, D., Latham, D. W., Mayor, M., et al. 2001, A&A, 375, L27

Nespral, D., Gandolfi, D., Deeg, H. J., et al. 2017, Astronomy and Astrophysics, 601, A128

Nettelmann, N., Fortney, J. J., & Garaud, P. 2013, AGU Fall Meeting Abstracts, 23, MR23B

Nettelmann, N., Fortney, J. J., Moore, K., & Mankovich, C. 2015, Monthly Notices of the Royal Astronomical Society, 447, 3422

Nettelmann, N., Holst, B., Kietzmann, A., et al. 2008, The Astrophysical Journal, 683, 1217

Nettelmann, N., Kramm, U., Redmer, R., & Neuhäuser, R. 2010, Astronomy and Astrophysics, 523, A26

Nettelmann, N., Wang, K., Fortney, J. J., et al. 2016, Icarus, 275, 107

Niemann, H. B., Atreya, S. K., Carignan, G. R., et al. 1998, Journal of Geophysical Research, 103, 22831

Null, G. W. 1976, The Astronomical Journal, 81, 1153

Nutzman, P., Gilliland, R. L., McCullough, P. R., et al. 2011, ApJ, 726, 3

Öberg, K. I., Murray-Clay, R., & Bergin, E. A. 2011, The Astrophysical Journal Letters, 743, L16

Oreshenko, M., Lavie, B., Grimm, S. L., et al. 2017, The Astrophysical Journal Letters, 847, L3

Ortiz, M., Gandolfi, D., Reffert, S., et al. 2015, A&A, 573, L6

Owen, J. E., & Murray-Clay, R. 2018, arXiv:1807.06033 [astro-ph], arXiv:1807.06033

Owen, J. E., & Wu, Y. 2016, The Astrophysical Journal, 817, 107

Pepper, J., Rodriguez, J. E., Collins, K. A., et al. 2017, AJ, 153, 215

Perna, R., Menou, K., & Rauscher, E. 2010, The Astrophysical Journal, 719, 1421

Petigura, E. A., Howard, A. W., Lopez, E. D., et al. 2016, The Astrophysical Journal, 818, 36

Petigura, E. A., Sinukoff, E., Lopez, E. D., et al. 2017, AJ, 153, 142

Piskorz, D., Buzard, C., Line, M. R., et al. 2018, The Astronomical Journal, 156, 133

Pollacco, D. L., Skillen, I., Collier Cameron, A., et al. 2006, Publications of the Astronomical Society of the Pacific, 118, 1407

Pollack, J. B., Hubickyj, O., Bodenheimer, P., et al. 1996, Icarus, 124, 62

Pont, F., Hébrard, G., Irwin, J. M., et al. 2009, A&A, 502, 695

Porco, C. C., Baker, E., Barbara, J., et al. 2005, Science, 307, 1243

Pu, B., & Valencia, D. 2017, The Astrophysical Journal, 846, 47

Queloz, D., Anderson, D., Collier Cameron, A., et al. 2010, A&A, 517, L1

Ricker, G. R., Winn, J. N., Vanderspek, R., et al. 2015, Journal of Astronomical Telescopes, Instruments, and Systems, 1, 014003

Roberts, G. O., & Rosenthal, J. S. 2004, Probab. Surveys, 1, 20

Rogers, L. A., & Seager, S. 2010, The Astrophysical Journal, 716, 1208

Rogers, T. M., & Komacek, T. D. 2014, The Astrophysical Journal, 794, 132

Saffe, C., Gómez, M., & Chavero, C. 2005, A&A, 443, 609

Safronov, V. S. 1960, Annales d'Astrophysique, 23, 979

Sanchis-Ojeda, R., Fabrycky, D. C., Winn, J. N., et al. 2012, Nature, 487, 449

Santerne, A., Hébrard, G., Deleuil, M., et al. 2014, A&A, 571, A37

Sarkis, P., Henning, T., Hartman, J. D., et al. 2018, The Astronomical Journal, 156, 216

Sato, B., Fischer, D. A., Henry, G. W., et al. 2005, ApJ, 633, 465

Saumon, D., Chabrier, G., & van Horn, H. M. 1995, The Astrophysical Journal Supplement Series, 99, 713

Schneider, J., Dedieu, C., Le Sidaner, P., Savalle, R., & Zolotukhin, I. 2011, Astronomy and Astrophysics, 532, A79

Schwarz, G. 1978, Ann. Statist., 6, 461

Shakura, N. I., & Sunyaev, R. A. 1973, Astronomy and Astrophysics, 24, 337

Showman, A. P., & Ingersoll, A. P. 1998, Icarus, 132, 205

Shporer, A., Zhou, G., Fulton, B. J., et al. 2017, The Astronomical Journal, 154, 188

Silverman, B. W. 1986, Density Estimation for Statistics and Data Analysis (Boston, MA: Springer US), doi:10.1007/978-1-4899-3324-9

Sing, D. K., Pont, F., Aigrain, S., et al. 2011, Monthly Notices of the Royal Astronomical Society, 416, 1443

Socrates, A. 2013, arXiv:1304.4121 [astro-ph], arXiv:1304.4121

Southworth, J. 2010, Monthly Notices of the Royal Astronomical Society, 408, 1689

Southworth, J., Wheatley, P. J., & Sams, G. 2007, Monthly Notices of the Royal Astronomical Society, 379, L11

Southworth, J., Hinse, T. C., Dominik, M., et al. 2012, Monthly Notices of the Royal Astronomical Society, 426, 1338

Spiegel, D. S., & Burrows, A. 2013, The Astrophysical Journal, 772, 76

Spiegelhalter, D. J., Best, N. G., Carlin, B. P., & van der Linde, A. 2002, Journal of the Royal Statistical Society: Series B (Statistical Methodology), 64, 583

Stahler, S. W., Shu, F. H., & Taam, R. E. 1980, The Astrophysical Journal, 241, 637

Stevenson, D. J. 1975, Physical Review B, 12, 3999

Stevenson, D. J., & Salpeter, E. E. 1977a, The Astrophysical Journal Supplement Series, 35, 239

—. 1977b, The Astrophysical Journal Supplement Series, 35, 221

Sullivan, P. W., Winn, J. N., Berta-Thompson, Z. K., et al. 2015, The Astrophysical Journal, 809, 77

Swain, M. R., Deroo, P., Griffith, C. A., et al. 2010, Nature, 463, 637

Szabó, G. M., & Kiss, L. L. 2011, The Astrophysical Journal Letters, 727, L44

Temple, L. Y., Hellier, C., Almleaky, Y., et al. 2019, The Astronomical Journal, 157, 141

Thompson, S. L. 1990, ANEOS Analytic Equations of State for Shock Physics Codes Input Manual, Tech. Rep. SAND-89-2951, 6939284, Sandia National Laboratory, doi:10.2172/6939284

Thorngren, D., & Fortney, J. J. 2019, The Astrophysical Journal, 874, L31

Thorngren, D. P., & Fortney, J. J. 2018, The Astronomical Journal, 155, 214

Thorngren, D. P., Fortney, J. J., Murray-Clay, R. A., & Lopez, E. D. 2016, The Astrophysical Journal, 831, 64

Toomre, A. 1964, The Astrophysical Journal, 139, 1217

Tremblin, P., Chabrier, G., Mayne, N. J., et al. 2017, The Astrophysical Journal, 841, 30

Triaud, A. H. M. J., Gillon, M., Ehrenreich, D., et al. 2015, Monthly Notices of the Royal Astronomical Society, 450, 2279

Turner, N. J., Fromang, S., Gammie, C., et al. 2014, Protostars and Planets VI, 411

van der Walt, S., Colbert, S. C., & Varoquaux, G. 2011, Computing in Science and Engineering, 13, 22

Vazan, A., Helled, R., Kovetz, A., & Podolak, M. 2015, The Astrophysical Journal, 803, 32

Vazan, A., Helled, R., Podolak, M., & Kovetz, A. 2016, The Astrophysical Journal, 829, 118

Vazan, A., Ormel, C. W., Noack, L., & Dominik, C. 2018, arXiv:1811.02588 [astro-ph], arXiv:1811.02588

von Zahn, U., Hunten, D. M., & Lehmacher, G. 1998, Journal of Geophysical Research, 103, 22815

Wahl, S. M., Wilson, H. F., & Militzer, B. 2013, The Astrophysical Journal, 773, 95

Wahl, S. M., Hubbard, W. B., Militzer, B., et al. 2017, Geophysical Research Letters, 44, 4649

Wakeford, H. R., Sing, D. K., Deming, D., et al. 2018, The Astronomical Journal, 155, 29

Weir, S. T., Mitchell, A. C., & Nellis, W. J. 1996, Physical Review Letters, 76, 1860

Weiss, L. M., Marcy, G. W., Rowe, J. F., et al. 2013, The Astrophysical Journal, 768, 14

Welsh, W. F., Orosz, J. A., Carter, J. A., et al. 2012, Nature, 481, 475

Wigner, E., & Huntington, H. B. 1935, Journal of Chemical Physics, 3, 764

Wilson, H. F., & Militzer, B. 2012a, Physical Review Letters, 108, 111101

—. 2012b, The Astrophysical Journal, 745, 54

Wolszczan, A., & Frail, D. A. 1992, Nature, 355, 145

Wong, M. H., Mahaffy, P. R., Atreya, S. K., Niemann, H. B., & Owen, T. C. 2004, Icarus, 171, 153

Wood, T. S., Garaud, P., & Stellmach, S. 2013, The Astrophysical Journal, 768, 157

Wu, Y., & Lithwick, Y. 2013, The Astrophysical Journal, 763, 13

Xie, J.-W. 2014, ApJS, 210, 25

Yadav, R. K., & Thorngren, D. P. 2017, The Astrophysical Journal Letters, 849, L12

Yang, R., & Berger, J. O. 1996, A Catalog of Noninformative Priors (Institute of Statistics and Decision Sciences, Duke University)

Yelle, R. V. 2004, Icarus, 170, 167

Youdin, A. N., & Mitchell, J. L. 2010, The Astrophysical Journal, 721, 1113

Zapolsky, H. S., & Salpeter, E. E. 1969, The Astrophysical Journal, 158, 809

Zharkov, V. N., & Trubitsyn, V. P. 1974, Icarus, 21, 152